Titre: Title:	Influence of electrode surface charge accumulation upon partial discharge behavior
Auteur: Author:	Vladimir Nikonov
Date:	1999
Type:	Mémoire ou thèse / Dissertation or Thesis
Référence: Citation:	Nikonov, V. (1999). Influence of electrode surface charge accumulation upon partial discharge behavior [Mémoire de maîtrise, École Polytechnique de Montréal]. PolyPublie. https://publications.polymtl.ca/8890/

UNIVERSITÉ DE MONTRÉAL

INFLUENCE OF ELECTRODE SURFACE CHARGE ACCUMULATION UPON PARTIAL DISCHARGE BEHAVIOR

VLADIMIR NIKONOV
DÉPARTEMENT DE GÉNIE PHYSIQUE ET DE GÉNIE DES MATÉRIAUX
ÉCOLE POLYTECHNIQUE DE MONTRÉAL

MÉMOIRE PRÉSENTÉ EN VUE DE L'OBTENTION
DU DIPLÔME DE MAÎTRISE ÈS SCIENCES APPLIQUÉES
(GÉNIE PHYSIQUE)
JUIN 1999

UNIVERSITÉ DE MONTRÉAL

ÉCOLE POLYTECHNIQUE DE MONTRÉAL

Ce mémoire intitulé:

INFLUENCE OF ELECTRODE SURFACE CHARGE ACCUMULATION UPON PARTIAL DISCHARGE BEHAVIOR

présenté par: NIKONOV Vladimir

en vue de l'obtention du diplôme de: Maîtrise ès sciences appliquées

a été dûment accepté par le jury d'examen constitué de:

M. MARTINU Ludvik, Ph.D., président

M. WERTHEIMER Michael, D.Sc.A., directeur

M. BARTNIKAS Raymond, Ph.D., co-directeur

M. CAMARERO Ricardo, Ph.D., membre

REMERCIEMENTS

Je remercie de tout coeur mes directeurs de recherches, le Dr. Ray Bartnikas et le Dr. Michael Wertheimer, avec qui j'ai abondamment discuté des problèmes physiques rencontrés dans le cadre de ce travail. Leur aide me fut indispensable.

Je remercie également les autres membres du jury, le Dr. Ludvik Martinu pour avoir bien voulu accepter la présidence et le Dr. Ricardo Camarero pour l'intérêt qu'il a manifesté pour cette recherche.

Je tiens à remercier les personnels scientifiques et techniques de l'École Polytechnique, ainsi que de l'IREQ pour leur aide concernant la préparation d'un montage expérimental à l' IREQ.

Je remercie Grzegorz Czeremuszkin, Daniel Poitras, Oleg Zabeida, Alexandru Fozza, ainsi que les autres membres de la Chaire de recherche sur les plasmas pour leur aide précieuse.

Enfin, je remercie le Dr. Gervais Leclerc qui m'a grandement aidé par sa lecture critique du mémoire.

RÉSUMÉ

Ce mémoire étudie l'influence de l'accumulation de charge superficielle sur la dynamique des décharges partielles. Nous avons modélisé et simulé le comportement d'une décharge partielle dans l'air à pression atmosphérique entre deux électrodes planes parallèles. Les deux électrodes sont métalliques, bien qu'une d'elles soit recouverte d'une barrière diélectrique. Le modèle employé s'appuie sur l'équation de Poisson ainsi que sur les équations de continuité des électrons et des ions.

Nos simulations ont révélé que l'accumulation de charges à la barrière diélectrique modifie plusieurs propriétés du système, notamment: la charge résiduelle dans le gap, la distribution radiale de la charge d'espace ainsi que le temps de transit de la décharge au travers du gap. Ces résultats sont comparés aux travaux théoriques de J.P. Novak et R. Bartnikas.

De plus, un modèle exponentiel simple nous a permis d'étudier l'effet de la conductivité superficielle sur l'évolution de la décharge. Nous avons ainsi pu montrer que la relaxation de la charge superficielle du diélectrique provoque une augmentation du champ électrique moyen dans le gap, bien que cette quantité diminue près de l'isolant. L'accumulation de charges dans les défauts du diélectrique provoque l'apparition d'aspérités dans le champ électrique favorisant l'injection de courant dans le diélectrique, ce qui crée une situation propice à l'initiation d'arborescences. Les résultats de ces simulations sont comparés aux travaux expérimentaux de C. Hudon, R. Bartnikas

et M.R. Wertheimer. Le mécanisme de transition d'une décharge impulsionnelle aux types de décharges "pseudoluminescent" et "luminescent" est également discuté.

ABSTRACT

A study of the influence of surface charge accumulation on the dynamics of partial discharges is presented here. We have modeled and simulated the behavior of a partial discharge at atmospheric pressure in an air gap between two plane parallel electrodes. Both electrodes are metallic, although one of them is covered with a dielectric barrier. A two-dimensional breakdown model based on Poisson's equation and the continuity equations for electrons and ions has been used for these simulations.

Our simulations have shown that the accumulation of charges at the dielectric barrier modifies several properties of the system, such as the residual charge in the gap, the radial space charge distribution, and the transit time of the discharge across the gap. These results are compared with the theoretical investigations published by J.P. Novak and R. Bartnikas.

In addition, the effect of surface conductivity on the evolution of the discharge has been studied with the help of a simple exponential model. It is shown that charge decay at the dielectric surface increases the value of the average electric field in the gap. The accumulations of charges in defects of the dielectric create field asperities that favor charge injection into the dielectric, a phenomenon which, in turn, may initiate electrical treeing. The results of these simulations are compared to the experimental results of C. Hudon, R. Bartnikas and M.R. Wertheimer. The transition mechanism from spark to pseudoglow and glow discharges is also discussed.

CONDENSÉ EN FRANÇAIS

Les décharges électriques sont connues pour se produire dans les systèmes isolants à haute tension des appareillages et des câbles de courant électrique, particulièrement quand des petites lacunes ou des petites cavités sont présentes. Ces décharges peuvent être caractérisées par différentes formes d'impulsions de courant ou de tension. Selon la pression du gaz, la séparation de l'intervalle, l'intensité du champ électrique et la conductivité extérieure des électrodes, la décharge peut prendre la forme d'une impulsion d'étincelle, d'une lueur, ou d'un 'pseudoglow'. Les décharges d'étincelle se caractérisent par un temps de montée rapide, une luminosité élevée et un canal de panne étroit, tandis que les décharges de lueur émettent une lumière diffuse. La décharge de 'pseudoglow' montre des caractéristiques communes aux décharges d'étincelle et de lueur [1-3].

D'un point de vue technologique, un des aspects les plus intéressants d'une décharge de barrière diélectrique est sa stabilité à la pression atmosphérique. C'est l'état de la surface du diélectrique présent qui joue un rôle principal quant à la détermination du type de décharge qui se produira. Les résultats des modèles de barrière diélectrique nous laissent envisages son utilisation pour des applications diverses telles que la production de l'ozone [4,5], le traitement de gaz polluants [6-11], et le déplacement de composé volatil organique [12,13].

Une grande partie des travaux expérimentaux, visant à comprendre des phénomènes de décharge en cavités, ont été effectués dans les années '60 et au début des

années '70 [14]. Ces travaux ont été complété par la simulation numérique des décharges partielles vers la fin des années '70. Des méthodes numériques ont été employées afin d'essayer de comprendre le mécanisme de panne dans la transition de l'étincelle à la décharge de lueur se produisant à la pression atmosphérique dans un intervalle court, parallèle et plat et ce dans différents gaz tels que l'hélium [15-17], l'hydrogène [18], et un mélange d'hélium avec d'air sec [19-21]. Plus tard, les auteurs ont étudié le comportement de panne se produisant dans un intervalle court dans l'air [22-24]. Les nombreuses simulations sur ordinateur ont étudié la formation et la propagation des décharges d'impulsion dans des gaz tels que l'azote et des mélanges l'oxygène et N_2-SF_6, dans des systèmes d'électrode métallique. Quelques modèles physiques pour les décharges ont été proposées [25-32].

Le travail de Novak et de Bartnikas [1] a aidé à la compréhension du rôle de l'accumulation de charge sur une surface isolante qui a lieu lors de la transition de la décharge d'étincelle à une décharge de forme 'pseudoglow' et de lueur dans l'air à la pression atmosphérique. Leurs calculs [1] prouvent qu'en l'absence d'aspérités dans le champ électrique près de surface diélectrique, la décharge naissante se produisant à la surface montre une expansion prononcée du canal de panne, qui est caractéristique d'une décharge de lueur. Le processus de transition de la décharge d'étincelle à la décharge de lueur se compose d'une grande diffusion radiale de la charge d'espace et d'une augmentation de la conductivité de la surface du diélectrique due à la dégradation électrochimique de cette surface [2,3].

La transition de l'impulsion d'étincelle à la décharge de lueur sur les électrodes revêtues d'époxyde a été découverte par hasard et étudiée expérimentalement par Hudon, Bartnikas et Wertheimer [2,3]; cette transition a été accompagnée d'une forte hausse de la conductivité de la surface diélectrique (environ à 10^{10} Ω par place). En utilisant cette information lors des travaux effectués dans le cadre de son M. Sc. A., Monette a en effet observé une augmentation de la lueur dans l'hélium, en utilisant une barrière diélectrique d'AlO_3/TiO_x avec la conductivité de la surface mentionnée ci-dessus. L'objectif du travail actuel a donc été de modeler l'effet de la charge d'une barrière diélectrique sur des décharges entre deux électrodes. Avant d'exécuter des simulations réelles, nous fournissons une description du modèle théorique en Chapitre I, les équations ont utilisé les coefficients d'ionisation, les mobilités, les diffusivités, les conditions initiales de la décharge, etc. Des considérations numériques pour la solution des équations de continuité et de Poisson sont présentées en Chapitre II. Nous commençons nos simulations avec un essai, où les résultats seront comparés à ceux du modèle développé avant par Dhali etal [35]. Les avantages du modèle actuel seront discutés en Chapitre III. L'évaluation de la densité de photoélectron en raison de la photoionisation dans l'air est donnée dans l'annexe I, puisque cet effet est insuffisamment important pour être inclus dans le texte. Les effets de l'accumulation de charge sur la surface diélectrique seront montrés en Chapitres IV et V, respectivement. Finalement, les résultats de nos simulations seront montrés dans la conclusion qui inclut également les objectifs des modélisations futures dont la formation des produits chimiques dans l'air (voir l'annexe II pour des résultats préliminaires) et le flux de photons sur la cathode (un essai du

calcul du flux est montré dans l'annexe III). L'annexe IV indique les améliorations effectuées au montage expérimentale à l'IREQ, et les préparations nécessaires à la poursuite de l'étude des décharges partielles.

TABLE OF CONTENTS

LIST OF APPENDIXES

LIST OF TABLES

LIST OF FIGURES

LIST OF SYMBOLS

PD: partial discharge

VOC: volatile organic compound

R: radial direction for axially symmetric configuration of electrodes

Z: axial direction for axially symmetric configuration of electrodes

n_e: density of electrons

n_{N^+}: density of positive nitrogen ions

n_{O^+}: density of positive oxygen ions

n_{O^-}: density of negative oxygen ions

D_e: diffusivity of electrons

D_{N^+}: diffusivity of positive nitrogen ions

D_{O^+}: diffusivity of positive oxygen ions

D_{O^-}: diffusivity of negative oxygen ions

v_e: drift velocity of electrons

v_{N^+}: drift velocity of positive nitrogen ions

v_{O^+}: drift velocity of positive oxygen ions

v_{O^-}: drift velocity of negative oxygen ions

s_e: source or sink mechanisms for electrons

s_{N^+}: source or sink mechanisms for positive nitrogen ions

s_{O^+} : source or sink mechanisms for positive oxygen ions

s_{O^-} : source or sink mechanisms for negative oxygen ions

α_{N^+} : ionization coefficient for nitrogen

α_{O^-} : ionization coefficient for oxygen

η_{O^-} : total attachment coefficient for oxygen

t : time

ρ : charge density

q_e : elementary charge

ε_0 : permittivity of vacuum

φ : electric potential

P : pressure in the gap

E : electric field

β : recombination coefficient

N : total number of particles per unit volume

η_2 : two-body attachment coefficient for oxygen

η_3 : three-body attachment coefficient for oxygen

W_e : drift velocity for the electrons in oxygen

μ_e : mobility of electrons

μ_{N^+} : mobility of nitrogen ions

μ_O : mobility of positive and negative oxygen ions

D_T : transverse diffusivity

D_L : longitudinal diffusivity

AC: alternative current

V: applied quasistatic voltage

Z_e : external series resistance

I_g : current in the gap

d : anode-cathode distance

d_g : gap distance

d_e : thickness of the dielectric barrier

ε : dielectric permitivity

$\sigma(r,t)$: surface charge density

E_r : radial electric field

E_z : axial electric field

i : grid point in radial direction

j : grid point in axial direction

FCT: flux-corrected transport

$\Delta V_{i,j}$: two-dimensional area element centered on the grid point (i, j)

F^L : the first order transportive flux in radial direction

F^H : the higher order transportive flux in radial direction

G^L : the first order transportive flux in axial direction

G^H : the higher order transportive flux in axial direction

A : antidiffusive flux

v_r : drift velocity in radial direction

v_z : drift velocity in axial direction

$V_{i,j}$: volume of the (i, j) cell

$r_{i,j}$: radius of the (i, j) cell

ΔT : time interval for calculations

FFT: Fast Fourier Transform

$\phi(r,z)$: electric potential in cylindrical coordinates

$\phi_n(r)$: electric potential expanded by FFT

$\rho_n(r)$: charge density expanded by FFT

h_i : distance between points r_i and r_{i-1}

$S_i(r)$: cubic spline function for eletric potential

V_{br} : breakdown voltage

V_{max} : the amplitude of applied voltage

$K(a/b)$: geometric factor for defect in dielectric

a and b : half-axes of ellipsoidal void in the dielectric

$\bar{E}_q$: average electric field due to contribution of surface and space electric charge

q_s : the residual charge from the previous PD

$g(\frac{a}{b}, \varepsilon_r)$: dimensionless proportionality factor

n_0: peak of electron density

δ: decay parameter

J: current density

τ: time constant

R: ohmic resistance

ε_{eff}: effective relative permittivity

υ: effective normal velocity

σ_0: surface conductivity of virgin epoxy matrix

Ψ_{ph}: the rate of photoionization

M_F: concentrations of chemical products

s: stoichiometric coefficient

$\Psi_{cathode}$: the photon flux at cathode

INTRODUCTION

Electrical discharges are known to occur in the high voltage insulating systems of electrical power apparatus and cables, especially when small gaps or small diameter cavities are present. These discharges can be characterized by different forms of current or voltage pulses. Depending upon the gas pressure, gap separation, electrical field intensity and the surface conductivity of the electrodes, the discharge can take the form of a spark pulse, a pulseless glow, or a pseudoglow. Spark discharges are characterized by a rapid rise time, a high luminosity and a narrow breakdown channel, whereas pulseless discharges emit a diffuse glow. Pseudoglow discharge exhibits features that are common to both spark and pulseless glow discharges [1-3].

From a technological point of view, one of the most interesting aspects of a dielectric barrier discharge is its stability at atmospheric pressure, where the presence of the dielectric plays a key role for determining the type of discharge that will occur. The results of dielectric-barrier modeling let us envision its use for such diverse applications as ozone production [4,5], treatment of flue gas [6-11], and volatile organic compound (VOC) removal [12,13].

Much experimental work, aimed at understanding discharge phenomena in cavities, was carried out in the sixties and early seventies [14]. It began to be supplemented by numerical simulation of partial discharges in the late seventies. Numerical methods were used in an attempt to understand the breakdown mechanism in the transition from spark to glow discharge at atmospheric pressure for a short parallel

plane gap in different gases such as helium [15-17] and hydrogen [18], as well as an admixture of helium with dry air [19-21]. Later, the authors studied the breakdown behavior of a short gap in air [22-24]. Numerous computer simulations investigated the formation and propagation of pulse-type discharges in non-attaching gases, such as nitrogen, and in attaching ones, such as oxygen and N_2-SF_6 mixtures in metallic-electrode systems, and some physical models for the discharges were proposed [25-32].

The work of Novak and Bartnikas [1] helped to achieve a proper understanding of the role of charge accumulation at an insulator surface in the transition mechanism from spark discharge to pseudoglow and glow forms of discharges in air at atmospheric pressure. Their calculations [1] show that in the absence of field-enhancing surface asperities, the incipient discharge occurring on a dielectric surface exhibits a pronounced breakdown channel expansion that is characteristic of a pulseless glow discharge. The process of discharge transition from spark to glow form consists of wide radial diffusion of space charge due to enhanced insulator voltage caused by charge accumulation, along with an increase of dielectric surface conductivity due to electrochemical degradation [2,3].

The transition from pulse to glow discharge on epoxy-coated electrodes was discovered by chance and studied experimentally by Hudon, Bartnikas and Wertheimer [2,3]; this transition was accompanied by a sharp increase in the surface conductivity (to about 10^{10} Ω per square) of the dielectric surface. Using this information, Monette indeed observed an enhancement of glow in He in his M. Sc. A. thesis work, when using a Al_2O_3/TiO_x dielectric barrier with the above-named conductivity. The objective of the

present work has therefore been to model the effect of charge (spreading and accumulation) on a dielectric barrier, on discharges in the inter-electrode gap. Before performing actual simulations, we provide in Chapter I a description of the theoretical model; namely, the equations used ionization and attachment coefficients, mobilities and diffusivities, initial and boundary conditions, etc. Numerical considerations for solving of the Continuity and Poisson's equations are presented in Chapter II. We start our simulations with a test, where the results are compared with that from an earlier model, namely that published by Dhali etal [35]. The advantages of the present model over earlier ones are discussed in Chapter III. The estimation of photoelectron density due to photo-ionization in the air is given in Appendix I, since this effect is indeed to be insufficiently important for inclusion in the main body of text. The effects of surface charge accumulation and spreading are shown in Chapters IV and V, respectively. Finally, the results of our simulations are summarized in the Conclusion, which also includes the objects of ongoing modeling studies, namely, the formation of chemical products in an atmospheric pressure air discharge (for preliminary results, see Appendix II), and photon flux at the cathode (a test of the flux calculation is shown in Appendix III). Appendix IV lists certain improvements to the experimental setup at IREQ, and preparations for experiments to continue investigations of partial discharges in the future.

CHAPTER I

THEORETICAL MODELLING OF PARTIAL DISCHARGE

1.1 The problem

We wish to simulate the formation and propagation of plasma discharges in a system possessing the axially symmetric configuration schematically shown in Fig. 1.1. The cathode is chosen to be metallic, while the anode consists of a metal electrode covered by a dielectric barrier, for example, made of epoxy resin.

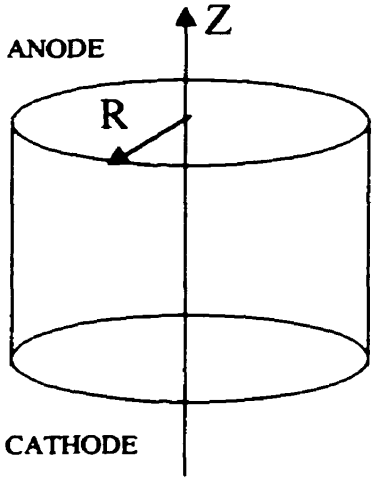

Figure 1.1 Cylindrical symmetric geometry for discharge propagation. R is the radial direction, and Z is the axial one.

All of our simulations are first aimed at computing the concentration of charged species (electrons and ions) as a function of time, space and other relevant parameters. This is achieved by numerically integrating an appropriate physical model that will be described below. Knowledge of the concentration of charged species allows us to compute other relevant quantities such as current, electric field, and velocity distributions.

1.2 Basic physical model

The physical model consists of the simplest set of equations containing the basic physics required to describe the formation and the propagation of the discharge. For this case of a discharge in air, first, we have the continuity equations for electrons, positive nitrogen ions, and negative and positive oxygen ions; the latter two species exist on account of the electronegative (electron-attaching) character of oxygen.

$$\frac{\partial n_e}{\partial t} + \bar{\nabla}\bullet(\bar{v}_e n_e) - D_e\nabla^2 n_e = \alpha_{N^+} n_e|v_e| + \alpha_{O^+} n_e|v_e| - \eta_{O^-} n_e|v_e| + s_e ,$$

$$\frac{\partial n_{N^+}}{\partial t} + \bar{\nabla}\bullet(\bar{v}_{N^+} n_{N^+}) - D_{N^+}\nabla^2 n_{N^+} = \alpha_{N^+} n_e|v_e| + s_{N^+} ,$$

$$\frac{\partial n_{O^+}}{\partial t} + \bar{\nabla}\bullet(\bar{v}_{O^+} n_{O^+}) - D_{O^+}\nabla^2 n_{O^+} = \alpha_{O^+} n_e|v_e| + s_{O^+} , \qquad (1.1)$$

$$\frac{\partial n_{O^-}}{\partial t} + \bar{\nabla}\bullet(\bar{v}_{O^-} n_{O^-}) - D_{O^-}\nabla^2 n_{O^-} = \eta_{O^-} n_e|v_e| + s_{O^-} ,$$

coupled with Poisson's equation:

$$\nabla^2\varphi = -\rho/\varepsilon_0 = -q_e(n_{O^+} + n_{N^+} - n_e - n_{O^-})/\varepsilon_0, \tag{1.2}$$

where subscripts e, N, O identify the nature of the species, n, D, v respectively stand for number density, diffusivity and drift velocity, φ is a potential, ε_0 is the permittivity of vacuum, q_e is the elementary charge, ρ is the charge density, α_i are ionization coefficients, and η is the attachment coefficient. The terms s_i are used to account for any of several particle source or sink mechanisms such as photoionization or recombination in the gas phase.

In addition to these basic equations, various constitutive relations also account for the ionization of both gases and attachment coefficient for oxygen, drift velocities, and so on. These shall be presented in detail in the next subsection.

1.3 Constitutive equations and parameter values

In order to compute n(t) from the previous model, we must first assign meaningful values to all of the other parameters. We shall hereby describe and justify the choices that were made in the present work. All values are expressed in the CGS system of units as was published already by several authors [34,35], except the pressure which is expressed in Torr, and the electric field which is given in V/cm (the coefficient to transform a voltage from SI to CGS is 300 [33]).

1.3.1 Ionization coefficients

The value of the recombination coefficients for electron-positive ion recombination rate constant was taken to be independent of the sort of the positive ions and equal to $\beta = 2.0 \cdot 10^{-7}$ cm^3/s [34]. As has been suggested by several authors [35,36,37], a sparse background value of 10^7 cm^{-3} is placed uniformly throughout the gap volume to simulate photoionization. The Townsend ionization coefficient α is given for nitrogen by the following relation [35,38]:

$$\alpha_{N_2} = 5.7 \cdot P \cdot \exp(-260 \cdot P/E) \qquad (cm^{-1}) \qquad (1.3)$$

where P is the pressure of the specified gas, and E is the electric field.

While the ionization coefficient for oxygen is given by [34,36]:

$$\alpha_{O_2} = 7.5 \cdot P \cdot \exp(-220 \cdot P/E) \qquad (cm^{-1}) \qquad (1.4)$$

1.3.2 Attachment coefficients

The two-body attachment coefficient for oxygen depends upon the applied electrical field and is given by the following expression [34,36]:

$$\begin{cases} \eta_2 = 2.0 \cdot 10^{-24} \cdot N, & \text{when } \dfrac{E}{N} > 1.835 \cdot 10^{-16} \\ \eta_2 = 5.032 \cdot 10^{28} \cdot N \cdot (10^{-4} \cdot E/N)^{2.655} & \text{when } \dfrac{E}{N} < 1.835 \cdot 10^{-16} \end{cases} \quad (\text{cm}^{-1}) \qquad (1.5)$$

where N is the number density of oxygen molecules per unit volume.

Reference [34] expresses the rate coefficient for a three-body attachment as:

$$\eta_3 = N^2 \cdot K_{a3} / |W_e| , \qquad (1.6)$$

where K_{a3} is given by:

$$K_{a3} = \frac{3.0 \cdot 10^{-30}}{1 + [(E/N)/4.0 \cdot 10^{-17}]^{1.5}} , \qquad (\text{cm}^6/\text{s}) \qquad (1.7)$$

where $|W_e|$ is the drift velocity for the electrons in oxygen:

$$W_e = 5.747 \cdot 10^{18} \cdot (10^{-4} \cdot E/N)^{0.6064} \qquad (\text{cm/s}) \qquad (1.8)$$

Since our simulations are always performed for atmospheric pressure, the number density of oxygen molecules per volume unit is constant $N = 5.38 \cdot 10^{18} \text{cm}^{-3}$. Finally, we have combined the two- and three-body attachment coefficients to get the net coefficient [34]:

$$\eta = \eta_2 + \eta_3 \qquad (1.9)$$

1.3.3 Mobilities and diffusivities

The literature gives the following values for the mobility of electrons, of positive nitrogen ions, and of positive and negative oxygen ions (where the later two are assumed to be identical) [35,38]:

$$\mu_e = 2.9 \cdot 10^5 / P \qquad (\text{cm}^2/\text{Vs}) \qquad (1.10)$$

$$\mu_{N^+} = 2.6 \cdot 10^3 / P \qquad (\text{cm}^2/\text{Vs}) \qquad (1.11)$$

$$\mu_O = 1554 / P \qquad (\text{cm}^2/\text{Vs}) \qquad (1.12)$$

The drift velocities appearing in the continuity equations can be computed from the mobilities using the following relation:

$$\bar{v} = \mu \cdot \bar{E} \qquad (1.13)$$

We have also found values for the transverse and longitudinal diffusivities D_L and D_T for oxygen namely [34,36]:

$$D_T = 1800 \text{ cm}^2/\text{s}, \qquad (1.14)$$

$$D_L = 1800 \text{ cm}^2/\text{s},$$

while for nitrogen those values are [35]:

D_T =2190 cm^2/s, (1.15)

D_L =1800 cm^2/s,

1.4 Initial and boundary conditions

The system of differential equations that constitutes our model cannot be solved unless some initial and boundary conditions are specified. The idealized physical system of Fig. 1.1 is now supplemented by the more detailed electrical circuit shown in Fig. 1.2. The period of V is chosen to be much longer than the discharge duration, so that V can be considered to be a quasistatic potential. An external series resistance (Z_e=50 Ω; it is applied as a detection impedance in electric circuits) completes the circuit [36].

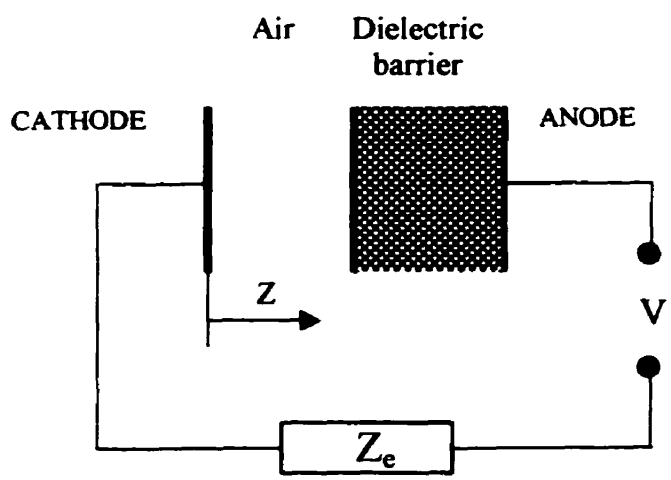

Figure 1.2 Dielectric barrier discharge configuration with external resistance.

For convenience, we have chosen to place the cathode at z=0 and the anode at z=d (Fig. 1.2). Therefore, the boundary conditions can be expressed follows [35]:

$$\begin{aligned} &\varphi(0,r,t) = 0, \\ &\varphi(d,r,t) = V - I_g(t)\cdot Z_e \end{aligned} \tag{1.16}$$

where I_g is a gap current, given by [39]:

$$I_g(t) = \frac{q_e}{d_g}\int_{gap}(n_{o^+}\vec{v}_{o^+} + n_{N^+}\vec{v}_{N^+} - n_e\vec{v}_e - n_{O^-}\vec{v}_{O^-})\cdot\hat{e}_z\cdot dV, \tag{1.17}$$

where d is the anode-cathode distance, d_g the gap distance and d_e the thickness of the electric barrier. Evidently:

$$d = d_g + d_e. \tag{1.18}$$

At the dielectric-gas interface, the boundary conditions are [36]:

$$\begin{aligned} &\varepsilon\varepsilon_0 E_z(d_g^+,r,t) - \varepsilon_0 E_z(d_g^-,r,t) = \sigma(r,t) \\ &E_r(z,0,t) = 0, \\ &E_r(z,R,t) = 0, \end{aligned} \tag{1.19}$$

where $\sigma(r,t)$ is the surface charge density accumulated at the dielectric-gas boundary, $E_z(d_g^+,r,t)$ is the axial field in a skin layer of dielectric, $E_z(d_g^-,r,t)$ is the axial field in vicinity of the dielectric surface, and E_r is the radial electric field.

CHAPTER II

NUMERICAL CONSIDERATIONS

In this chapter we will give a detailed description of the numerical algorithms used for integrating the model we have just presented. It is noteworthy that the algorithms presented here are not new, they have been adapted to FORTRAN 90 by the present author.

2.1 Integration of the Continuity equations

2.1.1 The FCT algorithm

The set of differential equations (Eq. 1.1) has been numerically integrated using a finite-difference technique, known as the flux-corrected transport (FCT). The FCT approach consists in using higher-order as well as first-order schemes, to construct the net transportive flux point-by-point, as a weighted average of a flux computed by a first-order scheme, and a flux computed by a higher-order scheme. This mixed technique was used to avoid false ripples near steep gradients in the case of higher-order scheme, and excessive diffusion in the first-order one. The order of the difference scheme determines the accuracy of method used. FCT techniques were first developed by Boris and Book [40] to model one-dimensional shock in fluids. An algorithm proposed later by Zalesak

[41] with multidimensional flux corrector for fluid problems has been used to write the continuity equations in our model.

We will now exemplify the FCT approach by considering the following system of equations for the two-dimensional case:

$$w_t + f_r + g_z = 0 \tag{2.1}$$

where w, f, and g are vector functions of the independent variables r, z, t:

$$\begin{aligned} w &= rN \\ f &= rNv_r \\ g &= rNv_z \end{aligned} \tag{2.2}$$

In finite difference flux form we have:

$$w_{i,j}^{n+1} = w_{i,j}^{n} - \Delta V_{i,j}^{-1}(F_{i+1/2,j} - F_{i-1/2,j} + G_{i,j+1/2} - G_{i,j-1/2}) \tag{2.3}$$

where w, g, f are defined on the spatial grid points r_i, z_i at time t^n and $\Delta V_{i,j}$ is a two-dimensional area element centered on the grid point (i, j). Now, there are two sets of transportive fluxes F and G. The steps comprising the FCT algorithm can be expressed as follows:

1) Compute $F^L_{i+1/2,j}, G^L_{i,j+1/2}$ by the first order scheme

2) Define $F^H_{i+1/2,j}, G^H_{i,j+1/2}$ by a higher order scheme

3) Compute the antidiffusive fluxes by using:

$$A_{i+1/2,j} = F^H{}_{i+1/2,j} - F^L{}_{i+1/2,j},$$
$$A_{i,j-1/2} = G^H{}_{i,j+1/2} - G^L{}_{i,j+1/2}. \tag{2.4}$$

4) Compute the first order time-advanced solution:

$$w_{i,j}{}^{td} = w_{i,j}{}^{n} - \Delta V_{i,j}{}^{-1}(F^L{}_{i+1/2,j} - F^L{}_{i-1/2,j} + G^L{}_{i,j+1/2} - G^L{}_{i,j-1/2}) \tag{2.5}$$

5) Limit the antidiffusive fluxes:

$$A^C{}_{i+1/2,j} = A_{i+1/2,j}C_{i+1/2,j}, 0 \le C_{i+1/2,j} \le 1,$$
$$A^C{}_{i,j+1/2} = A_{i,j+1/2}C_{i,j+1/2}, 0 \le C_{i,j+1/2} \le 1, \tag{2.6}$$

where $C_{i+1/2,j}$ and $C_{i,j+1/2}$ are calculated by using the algorithm given in [41].

6) Finally, apply these limited antidiffusive fluxes:

$$w_{i,j}{}^{n+1} = w_{i,j}{}^{td} - \Delta V_{i,j}{}^{-1}(A^C{}_{i+1/2,j} - A^C{}_{i-1/2,j} + A^C{}_{i,j+1/2} - A^C{}_{i,j-1/2}) \tag{2.7}$$

2.1.2 Application to our model

The convective contribution to the derivative of the densities shown in Eq. 1.1 for the density of the relevant species N and drift velocity v is:

$$\frac{\partial N}{\partial t}\Big|_{conv} = -\nabla \bullet (Nv), \tag{2.8}$$

For the axially symmetric geometry treating (rN) as the dependent variable we have:

$$\frac{\partial(rN)}{\partial t}\Big|_{conv} = -\frac{\partial f}{\partial r} - \frac{\partial g}{\partial z}, \tag{2.9}$$

where (see also Eq. 2.2)

$$\begin{aligned} f &= rNv_r, \\ g &= rNv_z,. \end{aligned} \tag{2.10}$$

and

$$\bar{v} = v_r\bar{e}_r + v_z\bar{e}_z \tag{2.11}$$

The density of the relevant species was defined at each grid point (i, j) for i^{th} point in radial direction and j^{th} in axial direction. A space of 50x50 points has been chosen for the program, with the same weights for the r and z directions. The simulations made with a space of 100x100 grids shown similar results of discharge propagation, but it involves a more time consuming procedure. All values $N_{i,j}, f_{i,j}, g_{i,j}$ were defined at all grid points at t=0. The Euler finite-difference approximation for Eq. 2.9, in flux form for higher-order calculation is:

$$\begin{aligned} N^{t+\Delta T/2}{}_{i,j} &= N^{t}{}_{i,j} - \frac{\Delta T}{2r_{i,j}V_{i,j}}(F^{t}{}_{i+1/2,j} - F^{t}{}_{i-1/2,j} + G^{t}{}_{i,j+1/2} - G^{t}{}_{i,j-1/2}), \\ N^{t+\Delta T}{}_{i,j} &= N^{t}{}_{i,j} - \frac{\Delta T}{2r_{i,j}V_{i,j}}(F^{t+\Delta T/2}{}_{i+1/2,j} - F^{t+\Delta T/2}{}_{i-1/2,j} + \\ & G^{t+\Delta T/2}{}_{i,j+1/2} - G^{t+\Delta T/2}{}_{i,j-1/2}), \end{aligned} \tag{2.12}$$

where $V_{i,j}$ and $r_{i,j}$ are the volume and radius of the (i,j) cell, and F^t, G^t are the fluxes corresponding at time t to values:

$$f = rNv_r$$
$$g = rNv_z \tag{2.10}$$

Using the eighth-order fluxes calculated by Zalesak, and assuming that all the grids have the same dimension in z direction for values of F^t and G^t, we have:

$$F_{i+1/2,j} = \pi\Delta z(r_{i,j} + r_{i+1,j})(A(f_{i+1,j} + f_{i,j}) + B(f_{i+2,j} + f_{i-1,j}) + C(f_{i+3,j} + f_{i-2,j}) + D(f_{i+4,j} + f_{i-3,j})),$$
$$G_{i,j+1/2} = \frac{\pi(r_{i-1,j} + 2r_{i,j} + r_{i+1,j})(r_{i+1,j} - r_{i-1,j})}{4} \cdot \tag{2.13}$$
$$(A(g_{i,j+1} + g_{i,j}) + B(g_{i,j+2} + g_{i,j-1}) + C(g_{i,j+3} + g_{i,j-2}) + D(g_{i,j+4} + g_{i,j-3})),$$

where

$$A = \frac{533}{840}$$
$$B = -\frac{139}{840}$$
$$C = \frac{29}{840} \tag{2.14}$$
$$D = -\frac{1}{280}$$

The first-order calculation of the convective contribution was handled using a donor cell algorithm with simple Eulerian time integration:

$$N^{t+\Delta T}_{i,j} = N^{t}_{i,j} - \frac{\Delta T}{V_{i,j}}(F^{t}_{i+1/2,j} - F^{t}_{i-1/2,j} + G^{t}_{i,j+1/2} - G^{t}_{i,j-1/2}), \tag{2.15}$$

where donor cell fluxes are given by:

$$\begin{aligned} F_{i+1/2,j} &= \pi\Delta z(r_{i,j} + r_{i+1,j})(\tilde{v}_r)_{i+1/2,j} \cdot N_{i,j}, for(\tilde{v}_r)_{i+1/2,j} \geq 0, \\ F_{i+1/2,j} &= \pi\Delta z(r_{i,j} + r_{i+1,j})(\tilde{v}_r)_{i+1/2,j} \cdot N_{i+1,j}, for(\tilde{v}_r)_{i+1/2,j} < 0, \end{aligned} \tag{2.16}$$

$$\begin{aligned} G_{i,j+1/2} &= \pi \frac{\pi(r_{i-1,j} + 2r_{i,j} + r_{i+1,j})(r_{i+1,j} - r_{i-1,j})}{4} \cdot (\tilde{v}_z)_{i,j+1/2} \cdot N_{i,j} \\ &, \text{for } (\tilde{v}_z)_{i,j+1/2} \geq 0, \\ G_{i,j+1/2} &= \pi \frac{\pi(r_{i-1,j} + 2r_{i,j} + r_{i+1,j})(r_{i+1,j} - r_{i-1,j})}{4} \cdot (\tilde{v}_z)_{i,j+1/2} \cdot N_{i,j+1} \\ &, \text{for } (\tilde{v}_z)_{i,j+1/2} < 0, \end{aligned} \tag{2.17}$$

Recalculated radial drift velocities values are:

$$\begin{aligned} (\tilde{v}_r)_{i+1/2,j} &= [(v_r)_{i,j} + (v_r)_{i+1,j}]/2, \\ (\tilde{v}_z)_{i,j+1/2} &= [(v_z)_{i,j} + (v_z)_{i,j-1}]/2, \end{aligned} \tag{2.18}$$

The contributions from ionization, attachment, and diffusion terms for Eq. 1.1 are calculated and added to the convective term $\frac{\partial N}{\partial t}\Big|_{conv}$ at each time step. The diffusion term is defined as:

$$\frac{\partial N}{\partial t}\Big|_{diff} = D_L(N^t_{i,j+1} + N^t_{i,j-1} - 2N^t_{i,j})/\Delta z^2 + \pi D_T(\frac{r_{i+1}+r_i}{r_{i+1}-r_i}\cdot (N^t_{i+1,j} + N^t_{i,j}) - \frac{r_i + r_{i-1}}{r_i - r_{i-1}}(N^t_{i,j} + N^t_{i-1,j}))\frac{\Delta z}{V_{i,j}}. \quad (2.19)$$

To include the importance of rapid variation of the impact ionization term α, a second-order scheme is used:

$$N^{t+\Delta T/2}_{i,j} = 0.5\cdot(N^t_{i,j} + N^{t+\Delta T}_{i,j}) + 0.5\cdot\Delta T\cdot N^t_{i,j}\cdot|v_e|\cdot\alpha,$$
$$\frac{\partial N}{\partial t}\Big|_{ion} = \alpha\cdot|v_e|\cdot N^{t+\Delta T/2}_{i,j}. \quad (2.20)$$

2.2 Poisson's solver

In addition to including the continuity equations, the model presented in Chapter I also included the Poisson equation (Eq. 1.2). In its most familiar form, it is written:

$$\nabla^2\phi = -\rho/\varepsilon_0 \quad (2.21)$$

Poisson's equation was used to determine the electric field caused by the presence of charged particles.

The algorithm for directly solving Poisson's equation in axially symmetric geometry was proposed by Kunhardt and collaborators [42,43]. It is based on the use of

a Fast Fourier Transform algorithm (FFT) for the axial solution, and expansion in cubic splines for the radial solution.

Consider that the potential ϕ in cylindrical coordinates, which must satisfy the relation:

$$\frac{1}{r}\frac{\partial}{\partial r}\left(r\frac{\partial}{\partial r}\phi(r,z)\right)+\frac{\partial^2}{\partial r^2}\phi(r,z)=-\rho(r,z)/\varepsilon_0 \tag{2.22}$$

with the boundary conditions:

$$\phi(r,0)=\phi(r,d)=0 \tag{2.23}$$

For:

$$\begin{aligned} &0\le z\le d\\ &0\le r\le R \end{aligned} \tag{2.24}$$

the functions ϕ and ρ were expanded as follows:

$$\phi(r,z)=\sum_{n=0}^{N-1}\phi_n(r)\sin\frac{n\pi}{d}z \tag{2.25}$$

$$\rho(r,z)=\sum_{n=0}^{N-1}\rho_n(r)\sin\frac{n\pi}{d}z \tag{2.26}$$

Using the orthogonality properties of the sine function, Eq. 2.22 can be rewritten in the following form:

$$\frac{\partial^2\phi_n}{\partial r^2}+\frac{1}{r}\frac{\partial\phi_n}{\partial r}+\frac{2}{\Delta z^2}\left(\cos\frac{n\pi}{N}-1\right)\phi_n=-\frac{\rho_n}{\varepsilon_0}. \tag{2.27}$$

The inverse Fourier transform algorithms may be used to obtain $\phi(r,z)$ from $\phi_n(r)$ in Eq. 2.27. The r-axis is partitioned into a set of $N_r - 1$ points $\{r_i\}$, with separation h_i between points r_i and r_{i+1} such that h_i was constant for every point i in the program. The set of N_r cubic spline functions was introduced to approximate the transformed potential $\phi_n(r)$ for $r_{i-1} < r < r_i$:

$$S_i(r) = \sum_{j=0}^{3} \frac{1}{j!} T_{i,j} (r - r_i)^j \tag{2.28}$$

The coefficients $T_{i,j}$ can only be determined if the transformed potential and its first three derivatives are continuous at each grid point. These conditions imply:

$$\begin{aligned}
T_{i,0} &= T_{i-1,0} + h_{i-1} T_{i-1,1} + \frac{1}{2} h^2_{i-1} T_{i-1,2} + \frac{1}{6} h^3_{i-1} T_{i-1,3} \\
T_{i,1} &= T_{i-1,1} + h_{i-1} T_{i-1,2} + \frac{1}{2} h^2_{i-1} T_{i-1,3} \\
T_{i,2} &= T_{i-1,2} + h_{i-1} T_{i-1,3} \\
T_{i,2} &+ f_i T_{i,1} + g_i T_{i,0} = \rho_n(r_i) \\
T_{i-1,2} &+ f_{i-1} T_{i-1,1} + g_{i-1} T_{i-1,0} = \rho_n(r_{i-1})
\end{aligned} \tag{2.29}$$

where

$$\begin{aligned}
f_i &= \frac{1}{r_i}, \\
g_i &= \frac{2}{h_z^{\,2}} \left(\cos \frac{n\pi}{N_z + 1} - 1 \right).
\end{aligned} \tag{2.30}$$

To solve the system of Eq. 2.29, we need two boundary conditions:

$$\begin{aligned} T_{0,1} &= 0, \\ T_{R,1} &= 0. \end{aligned} \tag{2.31}$$

Now Eq. 2.27 can be solved to find the solution of $4N_r$ simultaneous, linear equations with $4N_r$ unknowns. Based on the calculations by Kunhardt and Williams, the system of Eq. 2.29 can be simplified to:

$$\sum_j Q_{i,j} T_{j,0} = \sigma_i, \tag{2.32}$$

where σ_i are related to the original driving function, $\rho_n(r_i)$, and the matrix $\underline{\underline{Q}}$ is of tridiagonal form.

For Eq. 2.32 and points $2 < i < N_r - 1$, defining $f_i = \frac{1}{r_i}$ and $g_i = \frac{2}{h_z^2}(\cos\frac{n\pi}{N_z + 1} - 1)$, the matrix $\underline{\underline{Q}}$ has an expression described in the above-mentioned algorithm proposed by Kunhardt and Williams [42]:

$$Q_{i,j} = A_{i,1} E_i \delta_{i,j+1} + (A_{i,0} + A_{i,1} F_i - B_{i,1} E_{i+1}) \delta_{i,j} - (B_{i,0} + B_{i,1} F_{i+1}) \delta_{i,j-1} \tag{2.33}$$

The driving vector $\underline{\sigma}$ is given by:

$$\sigma_i = X_i + B_{i,1} W_{i+1} - A_{i,1} W_i \tag{2.34}$$

where

$$
\begin{aligned}
&A_{i,0} = 1 - \frac{1}{3}h^2 g_i, A_{i,1} = h(1 - \frac{1}{3}hf_i),\\
&B_{i,0} = 1 + \frac{1}{6}h^2 g_{i+1}, B_{i,1} = \frac{1}{6}h^2 f_{i+1},\\
&C_{i,0} = -\frac{1}{2}hg_i, C_{i,1} = 1 - \frac{1}{2}hf_i,\\
&D_{i,0} = \frac{1}{2}hg_{i+1}, D_{i,1} = 1 + \frac{1}{2}hf_{i+1},\\
&X_i = -\frac{1}{6}h^2(\rho_{i+1} + 2\rho_i), Y_i = -\frac{1}{2}h(\rho_{i+1} + \rho_i),\\
&h = r_{i+1} - r_i
\end{aligned}
\tag{2.35}
$$

Since a term of the form $\frac{1}{r}\frac{\partial \phi_n}{\partial r}$ appears in Eq. 2.22, the point $r = 0$ is singular and must be the object of a special treatment. Expanding the derivative in a Taylor series and keeping the lowest non-vanishing term, the last equation in the system of Eq. 2.29 becomes:

$$
2T_{0,2} + g_0 T_{0,0} = \rho_n(0) \tag{2.36}
$$

and the following expressions can be used in this case:

$$
\begin{aligned}
&Q_{0,0} = D_{0,1}A_{0,0} - B_{0,1}C_{0,0},\\
&Q_{0,1} = B_{0,1}D_{0,0} - D_{0,1}B_{0,0},\\
&Q_{1,1} = A_{1,0} + A_{1,1}F_1 - B_{1,1}E_2,\\
&\sigma_0 = D_{0,1}X_0 - B_{0,1}Y_0,\\
&\sigma_1 = X_1 - B_{1,1}W_2 - A_{1,1}W_1,
\end{aligned}
\tag{2.37}
$$

where

$$
\begin{aligned}
&A_{0,0} = 1 - \frac{1}{6}h^2 g_0, A_{0,1} = h, \\
&B_{0,0} = 1 + \frac{1}{6}h^2 g_1, B_{0,1} = \frac{1}{6}h^2 f_1, \\
&C_{0,0} = -\frac{1}{4}h g_0, C_{0,1} = 1, \\
&D_{0,0} = \frac{1}{2}h g_1, D_{0,1} = 1 + \frac{1}{2}h f_1, \\
&X_0 = -\frac{1}{6}h^2(\rho_0 + \rho_1), Y_0 = -\frac{1}{4}h(\rho_0 + 2\rho_1)
\end{aligned}
\tag{2.38}
$$

The boundary conditions for potential $\phi_n(R)$ are:

$$
\begin{aligned}
&Q_{N,N-1} = 0, \\
&Q_{N,N} = 1, \\
&\sigma_N = \phi_n(R).
\end{aligned}
\tag{2.39}
$$

Equation 2.32 is solved to determine the spline coefficients $\{T_{i,0}\}$. And, finally, the coefficients $T_{i,j}$ may be determined from the system of equations given below:

$$T_{i,1} = W_i + E_i T_{i-1,0} + F_i T_{i,0} \tag{2.40}$$

$$T_{i,2} = \rho_i - g_i T_{i,0} - f_i T_{i,1} \tag{2.41}$$

$$T_{i,3} = \frac{1}{h_i}(T_{i+1,2} - T_{i,2}) \tag{2.42}$$

2.3 Calculations of the discharge parameters

Before the simulation of discharge propagation can be performed, it is still necessary to compute some parameters of the partial discharge. The main purpose of these calculations is to estimate the time between two pulses in an idealized system whose behavior depends mostly on the slope of the applied voltage, as shown in Fig. 2.1.

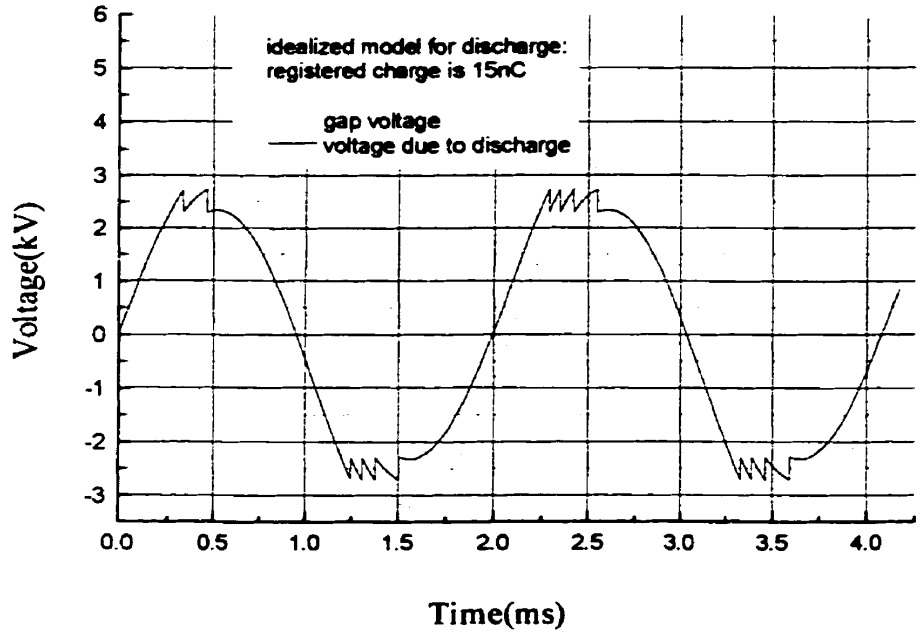

Figure 2.1 Idealised breakdown model: the applied voltage is 4 kV, the voltage in the gap is 3.2 kV and the breakdown voltage is 2720 V.

Let us assume that the applied voltage equals zero at t=0; the first discharge will occur when:

$$T_1 = \frac{1}{2\pi\nu}\arcsin(\frac{V_{br}}{V_{\max}}), \tag{2.43}$$

where V_{br} is the breakdown voltage, $V_{\max}$ is the amplitude of the applied voltage, and ν is the frequency. The last discharge in this positive voltage half-cycle occurs when the applied AC voltage reaches a maximum:

$$T_2 = \frac{1}{4\nu} \tag{2.44}$$

Thus, the time between two PD pulses can be easily calculated from:

$$\Delta t = t^{i+1} - t^i = \frac{1}{2\pi\nu}(\arcsin\frac{V_{br} + \Delta V \cdot (i+1)}{V_{\max}} - \arcsin\frac{V_{br} + \Delta V \cdot i}{V_{\max}}), \tag{2.45}$$

where i is the index of the discharge, t^i is the time at which the ith PD starts, t^{i+1} is the time for the next PD, and ΔV is the voltage change due to one discharge.

As can be seen in Fig. 2.1, the time between two consecutive discharges increases each time the polarity is reversed. The field collapse due to a PD is the difference between the field prior to the PD and the residual field after it. The average field prior to the PD comprises two contributions, namely, the field from the applied voltage and the field caused by the electrical charge left in the gap and on the surface from the previous PD. Assuming an ellipsoidal void in the dielectric (Fig. 2.2), the latter can be expressed as [44,45]:

$$\bar{E}_q = \frac{q_s}{\varepsilon_0 \pi b^2 [1 + \varepsilon_r (K(a/b) - 1)]} \tag{2.46}$$

where q_s is the residual charge from the previous PD, and ε_r is the relative permittivity. $K(a/b)$ is a geometric factor that can be obtained from references[44,45]:

$$K \begin{cases} \approx 1, & a/b << 1 \\ = 3, & a/b = 1 \\ \approx 4 \cdot a/b, & 1 < a/b < 10 \end{cases} \tag{2.47}$$

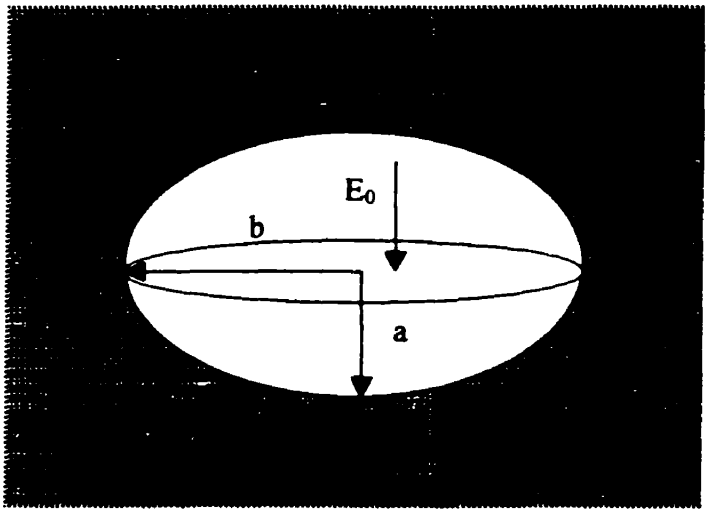

Figure 2.2 Ellipsoidal void in the dielectric, with half-axes a and b.

The dependence between the surface charge and the average field in the gap for a=0.025 cm and b=2.5 cm is shown in Fig. 2.3. The form of the charge distribution is accounted for a dimensionless proportionality factor [44,45]:

$$g(\frac{a}{b},\varepsilon_r)=\frac{1}{4}\frac{1}{(\frac{a}{b})^2}\left[1+\varepsilon_r(K\left(\frac{a}{b}\right)-1)\right] \tag{2.48}$$

The contribution of space and surface charges to the voltage can be deduced from Eq. 2.46 by using [44,45]:

$$\Delta U = 2\cdot a\cdot \bar{E}_q \tag{2.49}$$

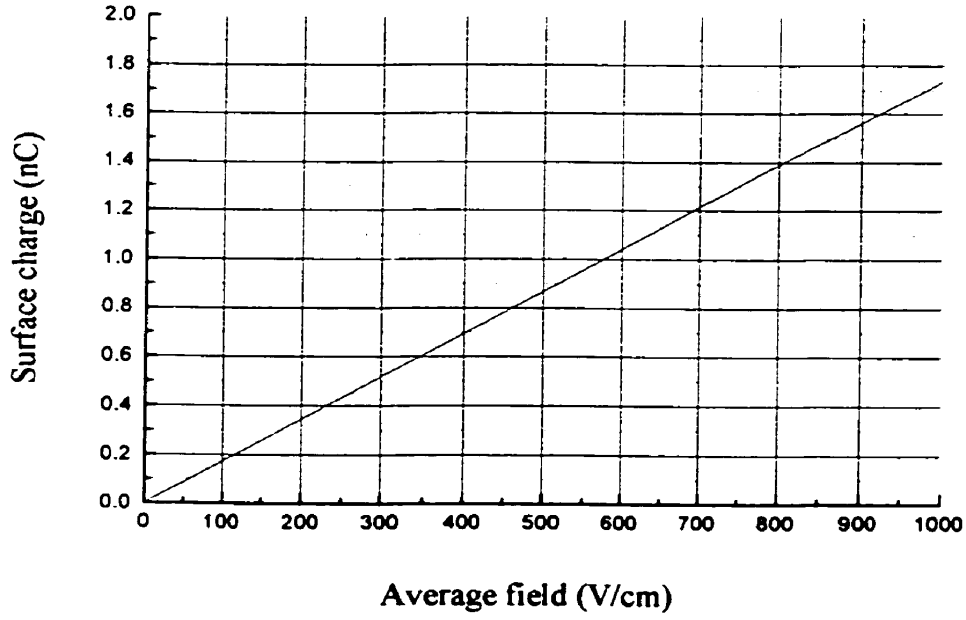

Figure 2.3 Average field contribution in the gap due to surface charge.

The time taken by the discharge to propagate through the void can be obtained from simulations. It will be shown in the next Chapter that this propagation time turns out to be much shorter than the time between two consecutive discharges. Eq. 2.46 is used for computing the average field value due to space and surface charge in the gap for discharge simulation in dielectric defect void.

CHAPTER III

DISCHARGE TOWARD THE DELECTRIC-COATED ANODE

Simulations of discharge toward the dielectric-coated anode can be found in the literature [36]. In order to test the validity of our software, we have chosen to apply it to this very same problem, so as to compare its results with those published earlier.

3.1 The physical system and assumptions

The system under study is shown schematically in Fig. 1.2. The anode and cathode are parallel metal disks separated by an air-filled gap; one of the electrodes, the anode at the moment of the discharge, is covered with a layer of dielectric material. For the external voltage V, we have chosen a step voltage applied at t=0, in series with a $50\,\Omega$ external resistance. Epoxy is chosen as the dielectric material ($\varepsilon_r = 4$), and the air gap is considered to be filled with a mixture of 80% N_2 and 20% O_2 at atmospheric

pressure (760 Torr, 100kPa) and at room temperature (20^0 C, 293K). The transport parameters of this idealized air mixture were computed from the values mentioned in Chapter I.

Streamer-like breakdowns are reported to be more probable when the pressure-gap distance product is higher than 10 Torr·cm, *e.g.*: with atmospheric pressure and a gap distance larger than 100 μm [46]. This is the situation under study here. The widths of the gap and of the dielectric were both fixed at identical values, d=0.05 cm. Under those conditions, the value of the breakdown voltage across the air gap could be established at 2720 V, with the help of the following expression [47]:

$$V_{br} = 24.41(\rho d) + 6.73\sqrt{\rho d} \qquad (3.1)$$

where V_{br} is the breakdown voltage in kV, d is the gap width in cm, and ρ is a normalized air density (equal to unity under our operating conditions). A similar calculation for the case of a metallic cathode and anode yields a breakdown voltage of 3400V, which corresponds to an electric field value of 54.4 kV/cm. The corresponding field value is 13.6 kV/cm inside the void-free dielectric on the anode. In discharge simulation, it is often assumed that a single electron avalanche takes place at the cathode surface at t=0. Instead, we have opted for initial Gaussian-shaped plasma. This approach is advantageous because it allows us to bypass the Townsend phase of the simulation, as discussed elsewhere [36]. The surface charge at the metallic cathode was modeled with an array of two-dimensional Gaussian profiles having a peak electron density of $n_0=10^{13}$ (cm^{-3}) and a $1/e$ radius of 0.1 mm:

$$n_e = n_0 \cdot \exp(-(i^2 + j^2)/\delta^2) \qquad (3.2)$$

where i and j are the grid indices for radial and axial directions respectively, and the decay parameter is δ =10. Contribution of surface charge in voltage across air gap is 643 V; it was calculated by using the Poisson's Equation (Section 2.2) and Eq. 2.49 (Section 2.3). So, it gives us the high overvoltage case of 30%.

In order to simulate the photoionization process, we also assume an initially quasi-neutral, uniform plasma background with a density of 10^7 cm^{-3}, an approach already used by several authors [35,37], instead of calculation of photoelectron density (see Appendix I). The same values are used for the initial sparse concentrations of both oxygen and nitrogen positive ions. Finally, we used the discharge parameters presented in Table 3.1. Section 2.3 explains how those values have been computed.

Table 3.1 Discharge parameters (computed in Section 2.3).

Space charge in the air gap	40 pC
Voltage change per discharge	1.2 V
Contribution per discharge to the average field change in the gap	23 V/cm
Number of pulses per half cycle of ac voltage in the gap	416
Average time between two close discharges	4.1 μs
Time between the first two discharges in a half cycle	1.8 μs
Time between the last two discharges in a half of voltage cycle	31.4 μs
Contribution of total charge accumulation for half of ac voltage cycle to the voltage drop in the gap	479 V

3.2 Results of simulation

3.2.1 Macroscopic results

Figure 3.1 shows that the maximum velocity of discharge propagation varies from $3 \cdot 10^7 cm/\text{sec}$ (after the simulation has taken a few steps to stabilize in the program calculations), up to a maximum value $6.25 \cdot 10^7 cm/\text{sec}$ when the discharge begins to reach the dielectric surface of the anode. The streamer velocity strongly depends on the potential of the charged dielectric surface, as will be shown in Chapter IV. The electrons

travel through the gap in 0.7 ns. The electric field in the gap, in the dielectric, and the electron velocity all attain their maximum values simultaneously.

Figure 3.2 shows that the gap field attains its maximum value of slightly more than 200 kV/cm, while Figure 3.6 shows a value slightly greater than 50 kV/cm just inside the dielectric layer. The electron space charge reaches a value of ~30pC in 0.7ns, as shown in Fig. 3.3; at the same instant, the discharge current reaches 15 mA (Fig. 3.5), causing a voltage drop ΔV of 1.5V in the gap (Fig. 3.4). The shape of the current decay is primarily determined by the distribution of charge on the dielectric surface, since accumulated surface charges produce a radial electric field on the dielectric. This tends to uniformly redistribute the surface charge until the field in the gap falls below its breakdown value. The charge accumulation effect, in turn, strongly depends on the nature of the dielectric surface. The current decays more slowly when the charge spreads over a wider area of the dielectric surface [36]. Surface charge accumulation strongly depends on the presence of inhomogeneities at the dielectric surface, as will be discussed in Section 4.2, while Section 4.3 presents simulations showing the effect of surface charge accumulation, and Chapter V discusses how the discharge characteristics are affected by surface charge decay due to surface conductivity.

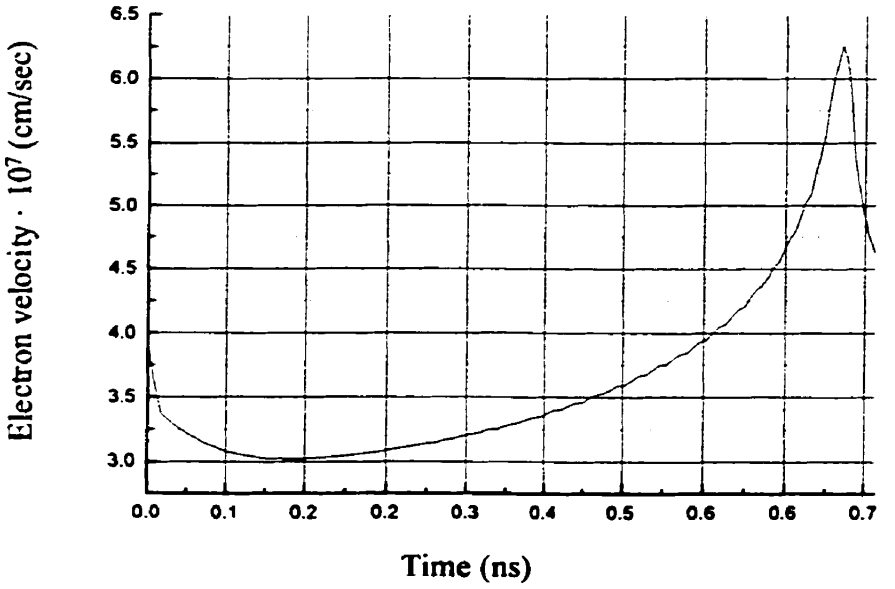

Figure 3.1 Maximum electron drift velocity vs time.

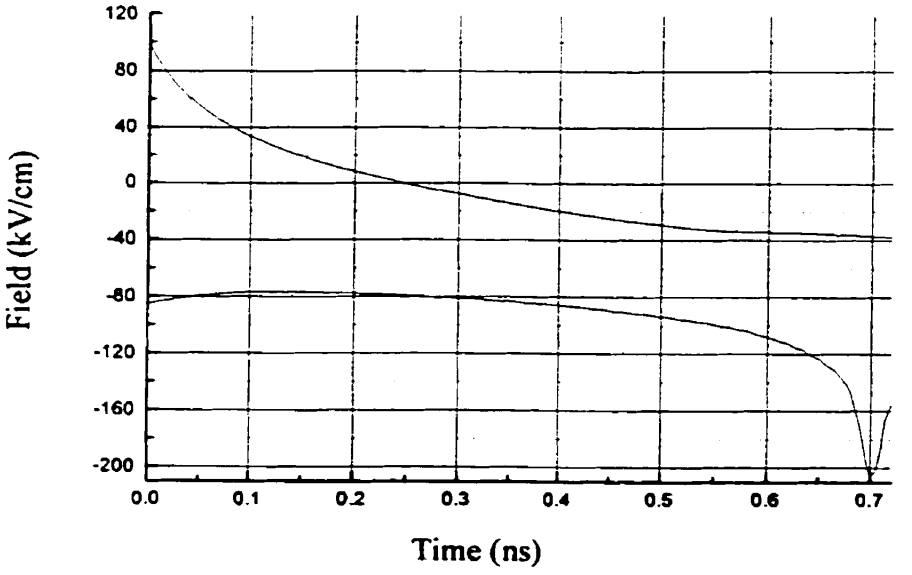

Figure 3.2 Maximum and minimum axial field in the gap vs time.

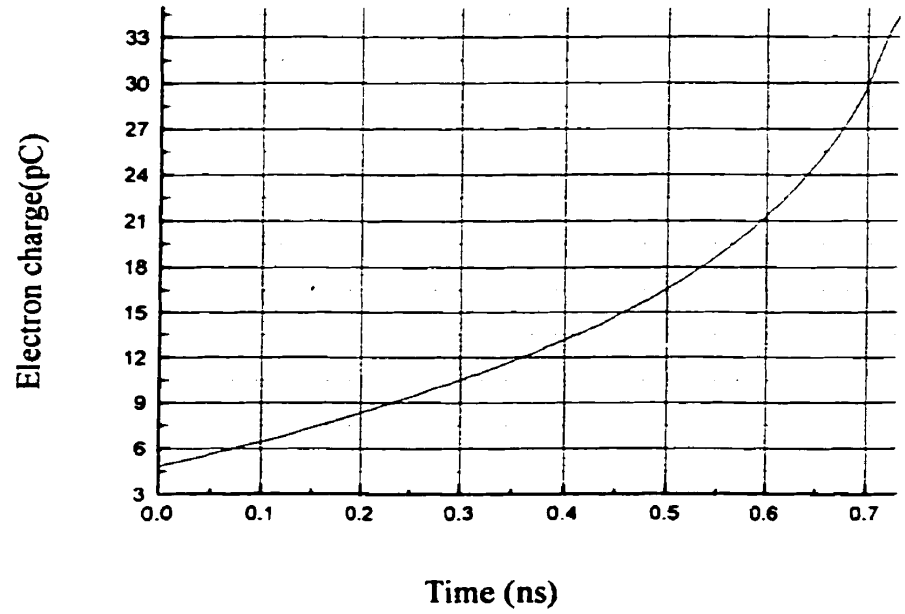

Figure 3.3 Electron charge vs time.

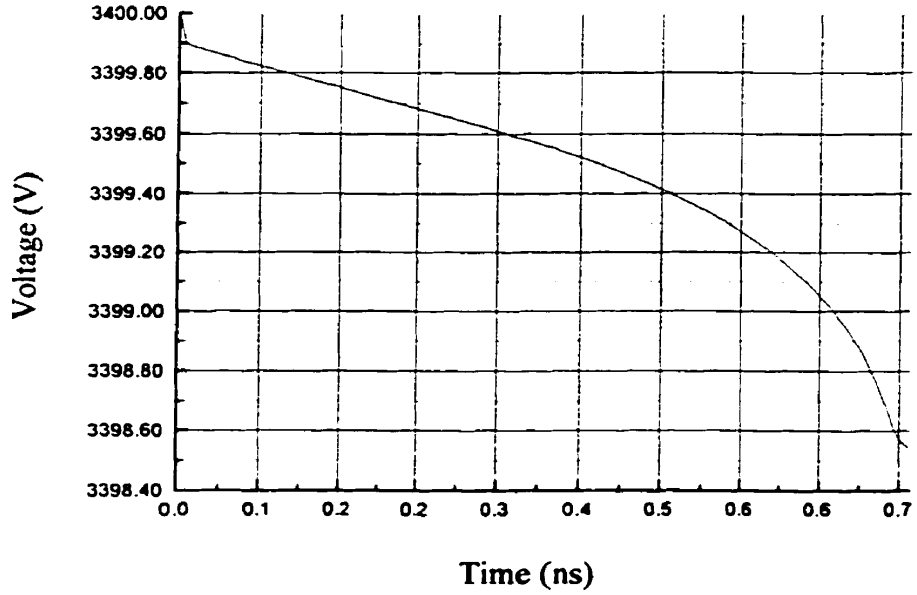

Figure 3.4 Voltage contribution in the gap due to space and surface charge.

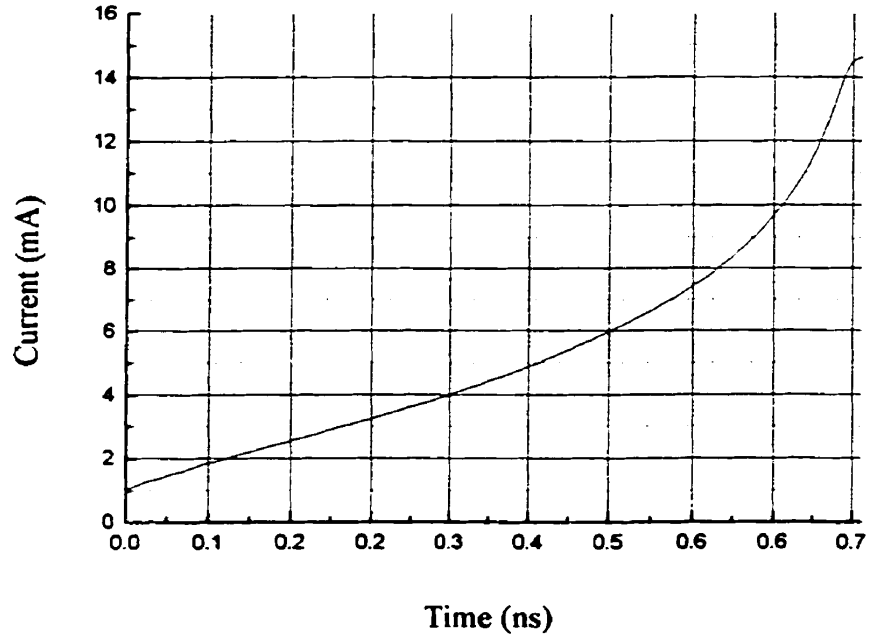

Figure 3.5 Current in the gap due to space charge.

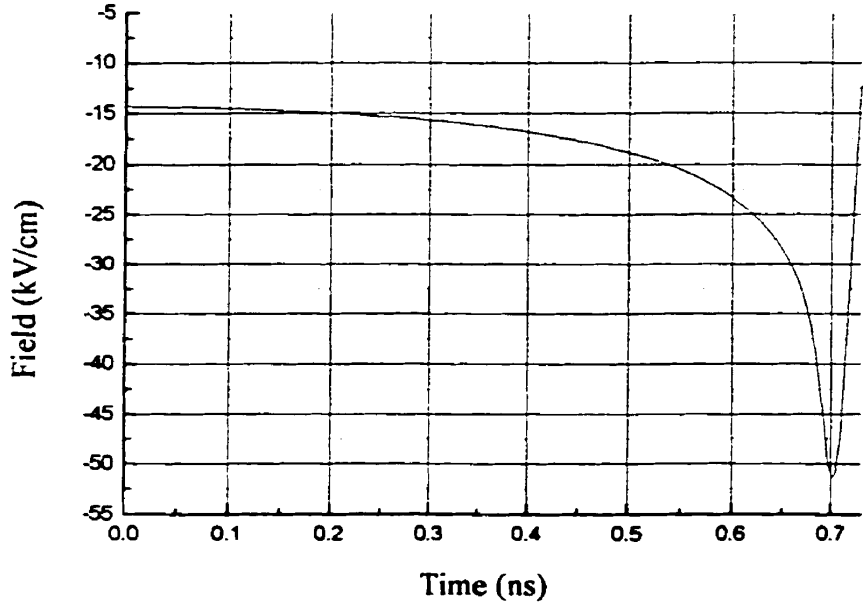

Figure 3.6 Field modification inside the dielectric skin layer due to space and surface charges in the gap.

3.2.2 Distribution of charged species

We have computed the evolution of the density distribution of electrons (Figs. 3.7-3.8), nitrogen ions (Figs. 3.9-3.10), positive oxygen ions (Figs. 3.11-3.12), and negative oxygen ions (Figs. 3.13-3.14). It can be observed that a high electric field and increasing electron density due to ionization lead to a steep density gradient at 0.7 ns for all these species. The negative oxygen ion density strongly depends upon the field distribution in the gap, and on the electron drift velocity, as was already discussed in Section 1.3.2. Negative oxygen ions mostly concentrate close to the cathode, as shown in Figs. 3.13 and 3.14.

Figures 3.15 and 3.16 show the evolution of the total net charge density, from which we note that high electron mobility and the resulting field distribution in the radial direction lead to a depression of the net density in the middle of the gap, and to a sharp peak near the anode near t=0.7 ns.

Density distribution profiles for different kinds of charged particles for two particular times, namely, 0.1 ns and 0.7 ns, are shown in Fig. 3.17.

The Poisson solver was used to compute the potential due to the charge distribution (Figs. 3.18 and 3.19), confirming the data shown in Figs. 3.15, 3.16 and 3.17. It is readily seen that the total net charge density is positive close to the cathode, resulting in a potential maximum of 50 V at t=0.7 ns, while ϕ=-425 V at t=0.6 ns close to the anode because of the net negative charge in this region.

Figures 3.20-3.21 shows the axial field distribution as a function of time. As the discharge approaches the dielectric, the field inside the latter medium rises up to 55 kV/cm, as seen in Fig. 3.26. The electric field in the gap reaches its maximum value when most electrons concentrate in the vicinity of the anode ($t \approx 0.7$ ns), at which moment its amplitude attains more than 200 kV/cm (Fig. 3.21). The simulation results of present model were compared to those reported in the literature [35]. The field due to applied voltage in our model is 54.4 kV/cm, compared with 52 kV/cm in [35]. The simulations show that the drift velocity of electrons is in the range of $3 - 6.25 \cdot 10^7$ cm/s in our case, and $4 \cdot 10^7$ cm/s reported in Ref. 35. The axial field is 150 kV/cm in Ref. 35, as a result of discharge propagation, compared with 80 - 210 kV/cm in our model. So, these results prove that the present program is compatible with published data. Meanwhile, our program improves earlier ones as follows:

- it permits one to study effects of surface charge and to estimate field stresses inside of dielectric,

- it permits estimation of the photo-ionization rates for different $P \cdot d$ products (see Appendix I),

- the time interval was taken from the Courant condition, namely, $\delta t = 0.25 \cdot \delta x / \upsilon_{max}$, where δx is the space of the grid in the radial/axial direction, and υ_{max} is the maximum value of the drift velocity.

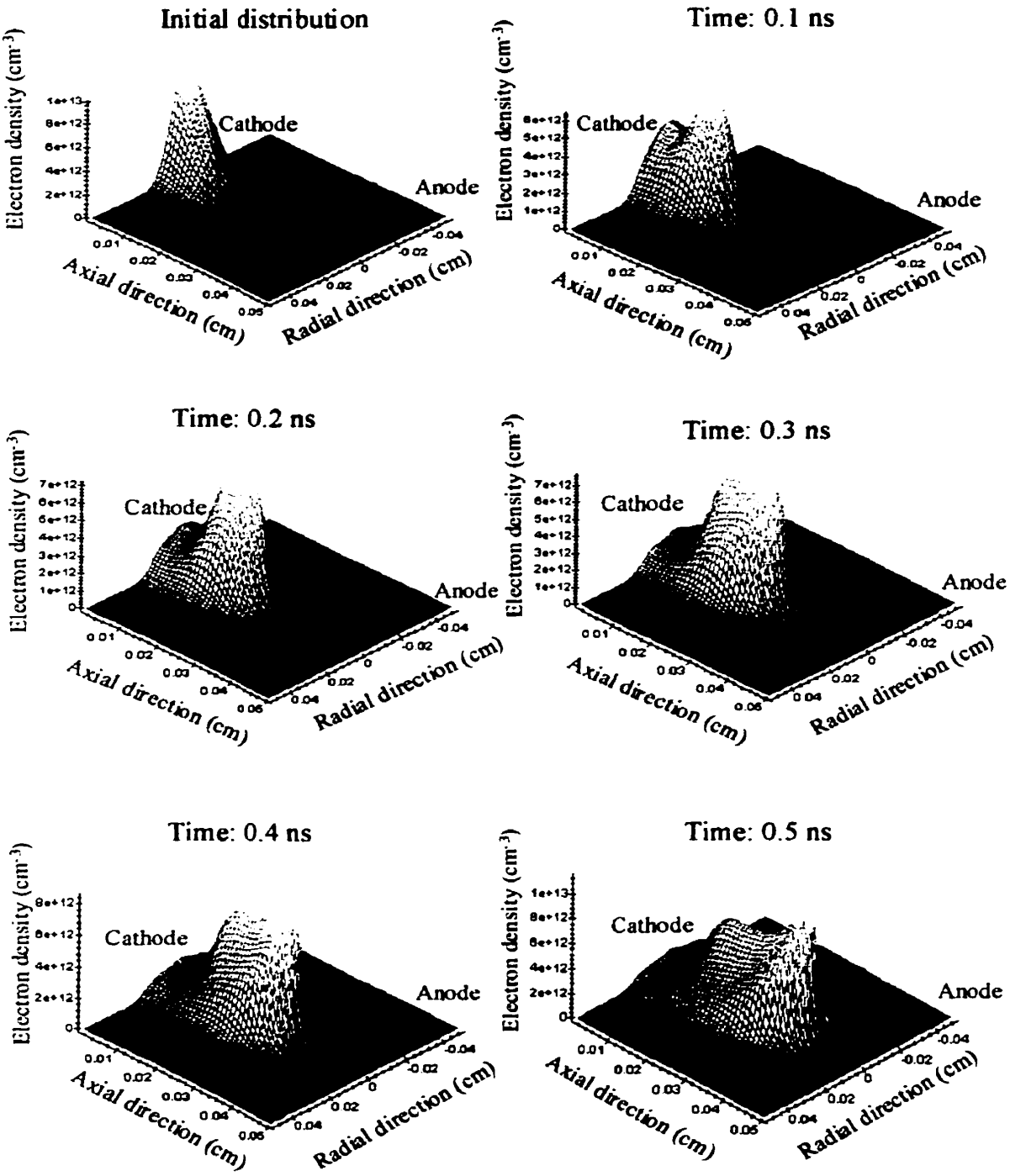

Figure 3.7 Electron density distribution at different times of discharge propagation.

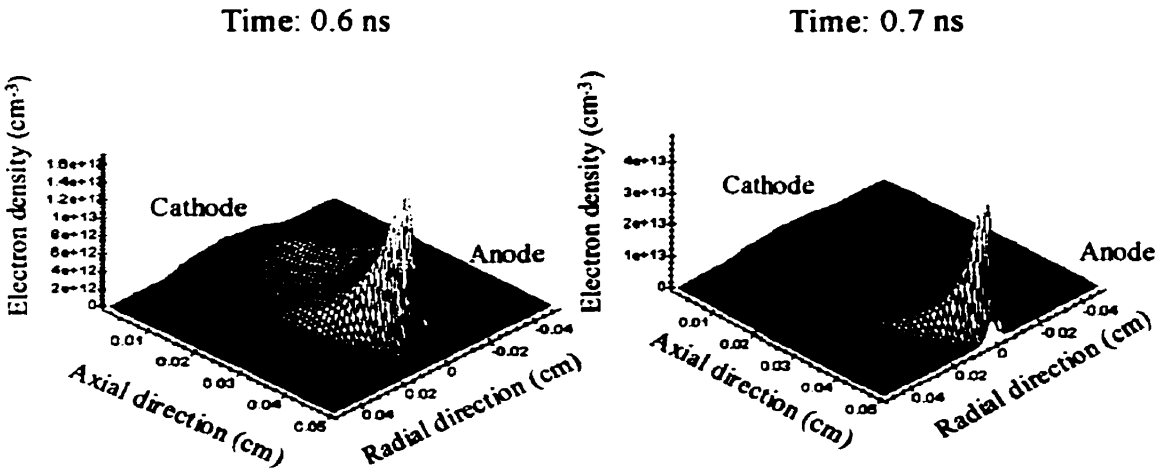

Figure 3.7 (continued) Electron density distribution at different times of discharge propagation.

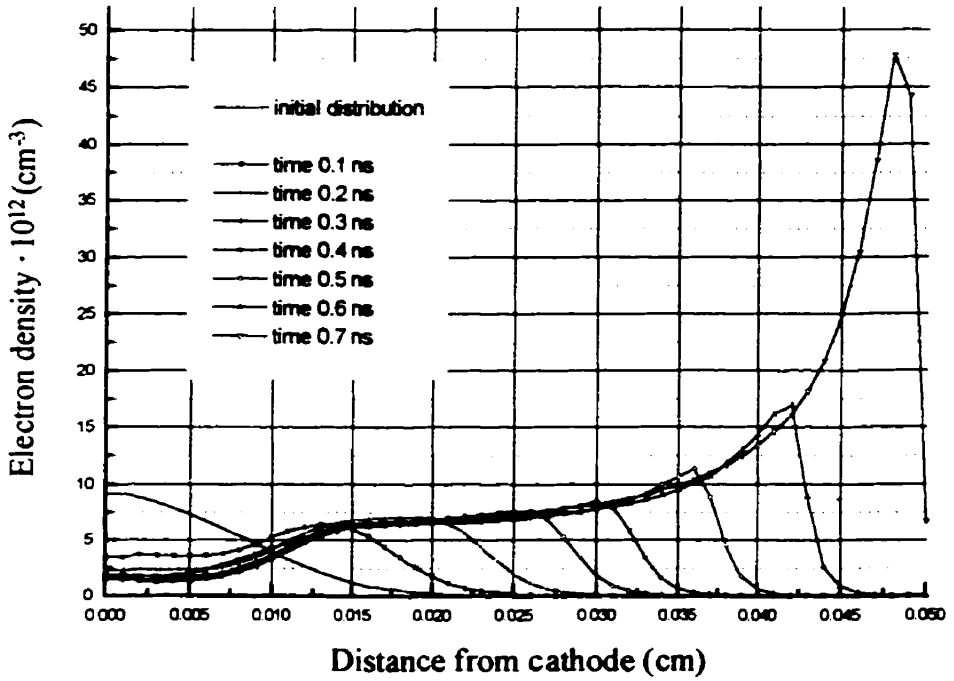

Figure 3.8 Axial electron density profile (r=0) vs time.

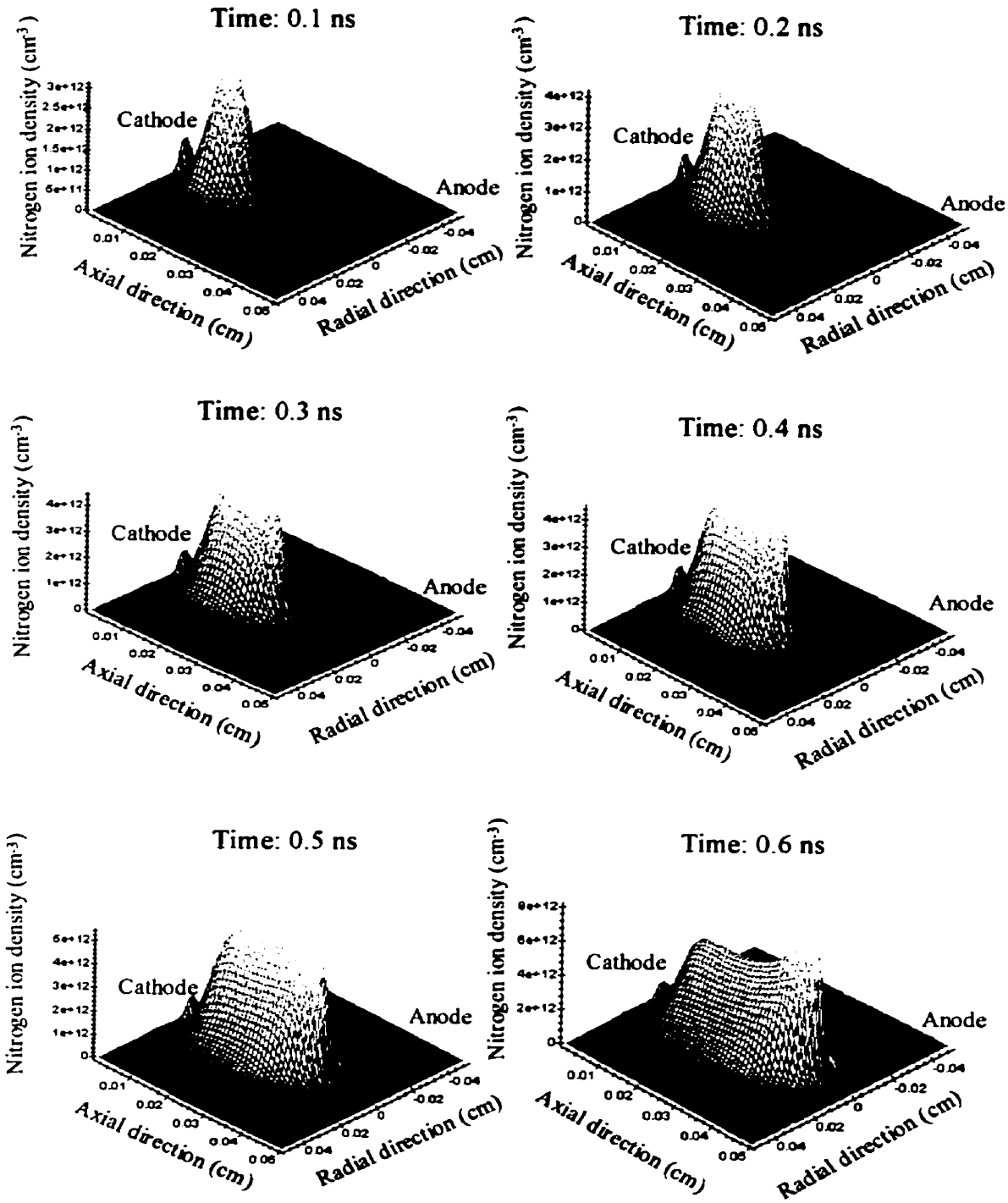

Figure 3.9 Nitrogen ion density distribution at different times of discharge propagation.

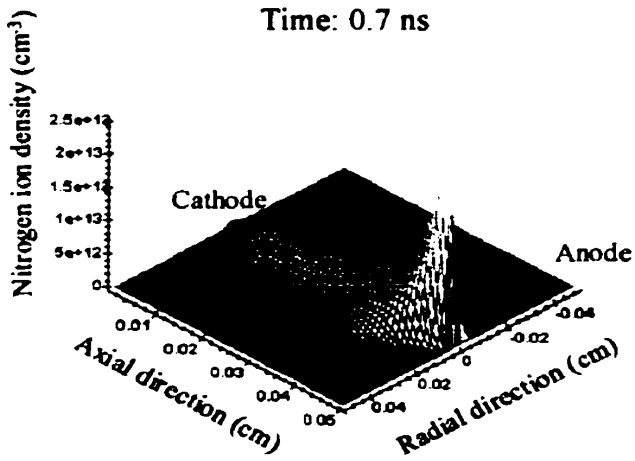

Figure 3.9 (continued) Nitrogen ion density distribution at different times of discharge propagation.

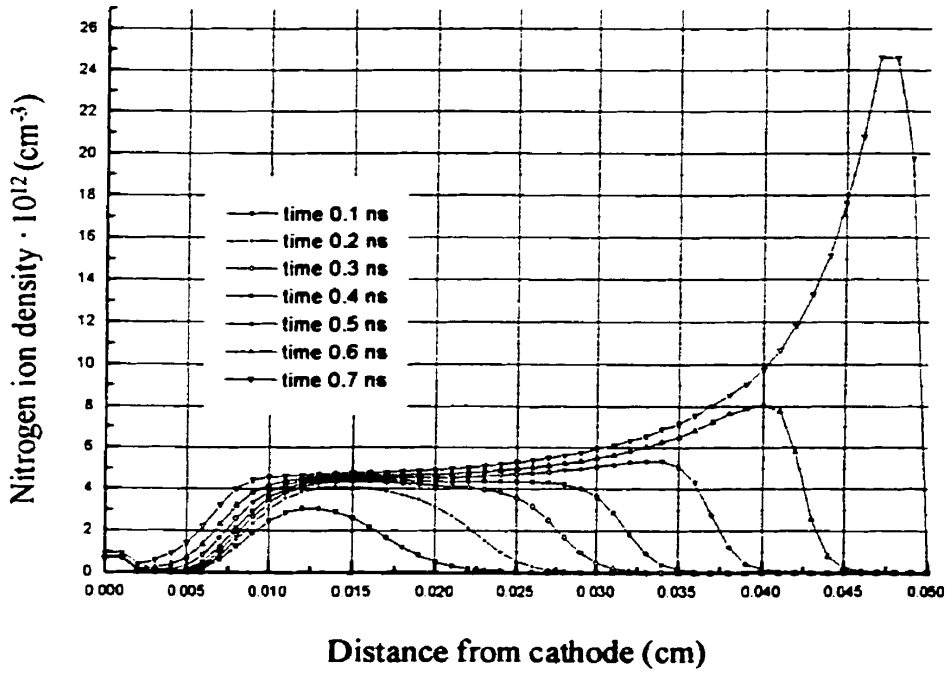

Figure 3.10 Nitrogen ion density profile (r=0) vs time.

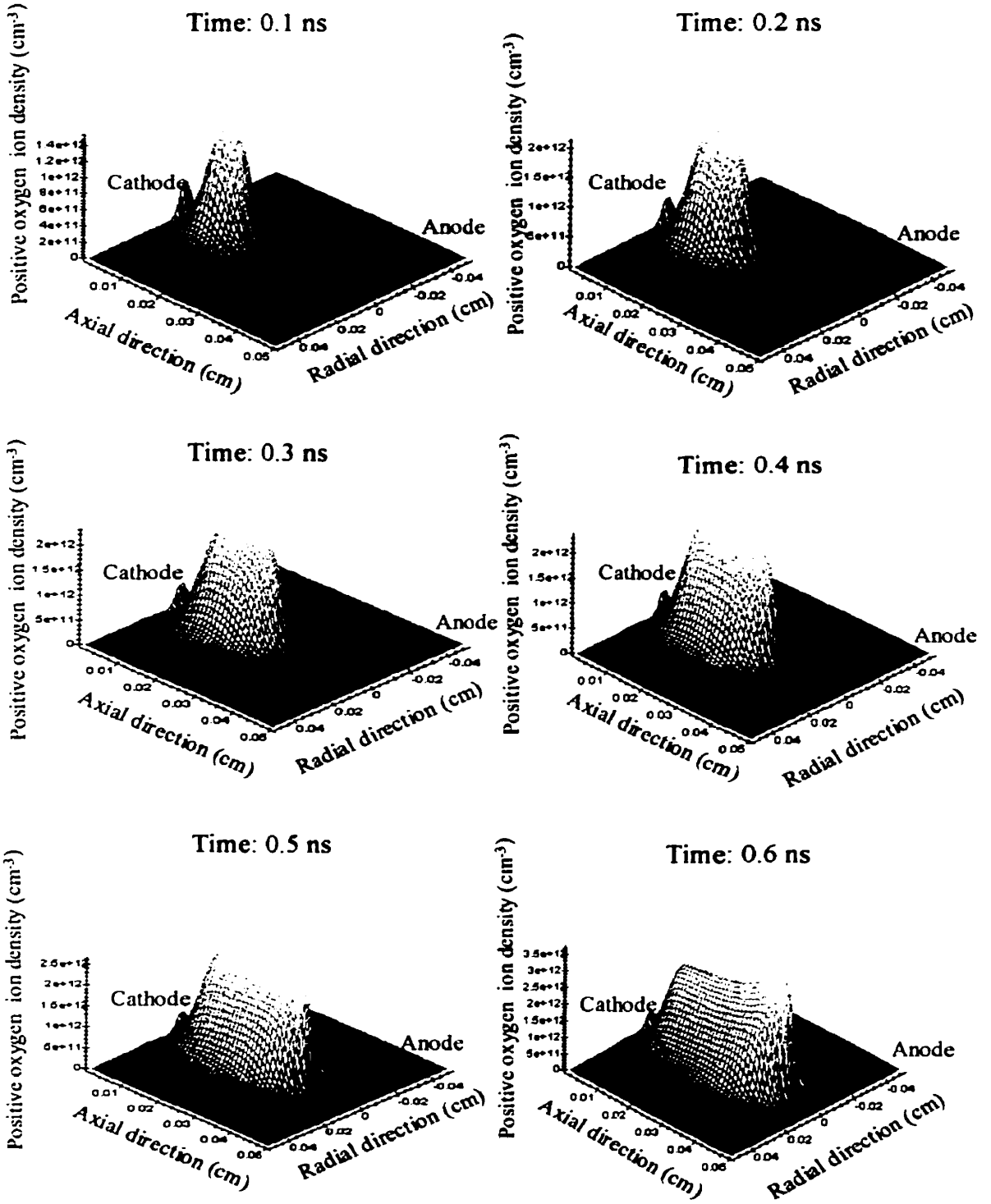

Figure 3.11 Density distribution of positive oxygen ions at different times of discharge propagation.

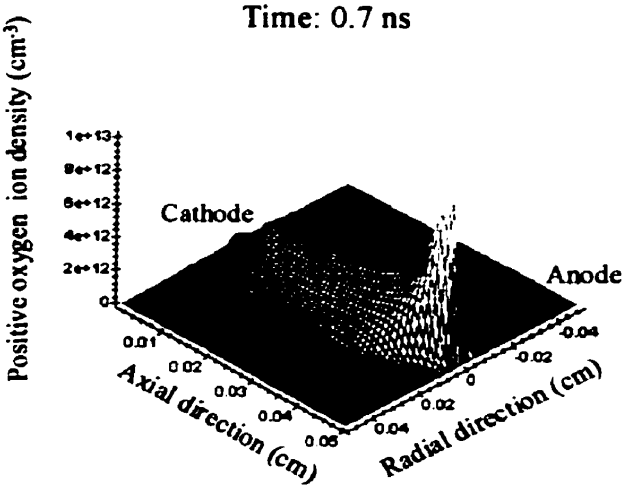

Figure 3.11 (continued) Density distribution of positive oxygen ions at different times of discharge propagation.

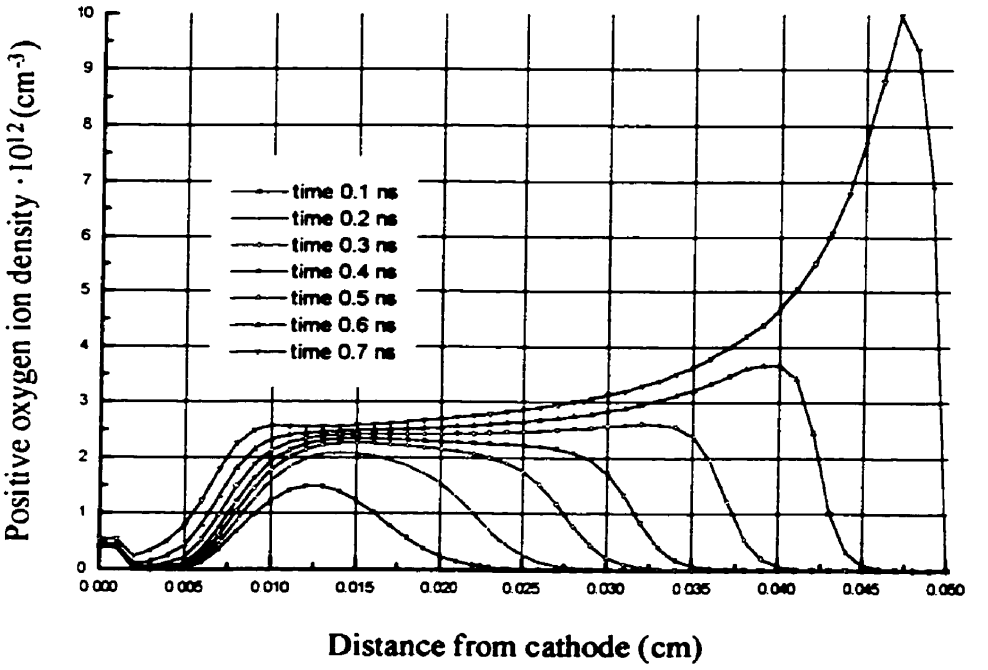

Figure 3.12 Positive oxygen ion density profile vs time.

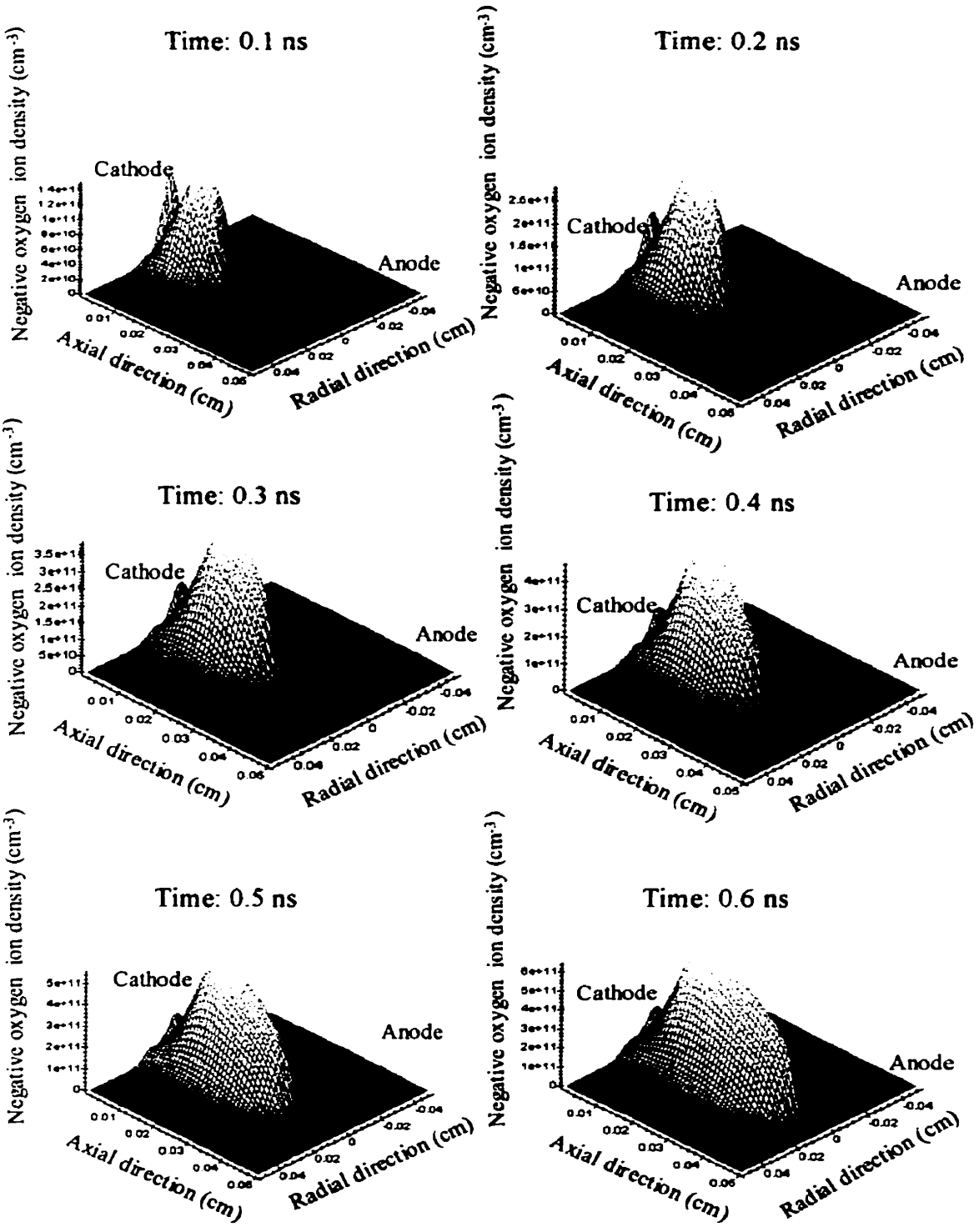

Figure 3.13 Density distribution of negative oxygen ions at different times of discharge propagation.

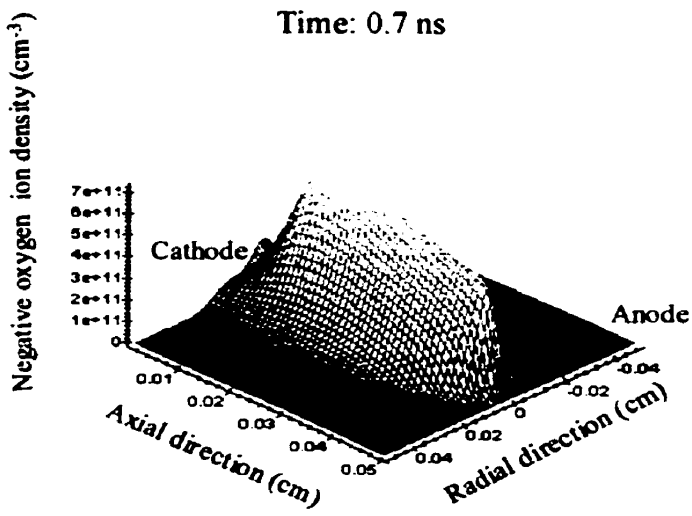

Figure 3.13 (continued) Density distribution of negative oxygen ions at different times of discharge propagation.

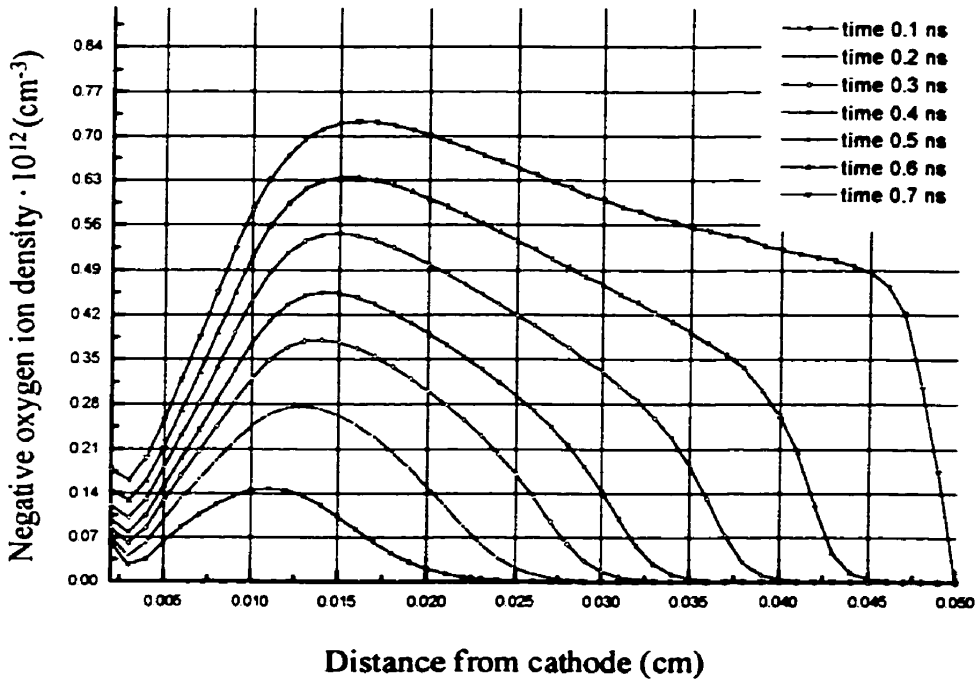

Figure 3.14 Negative oxygen ion density profile vs time.

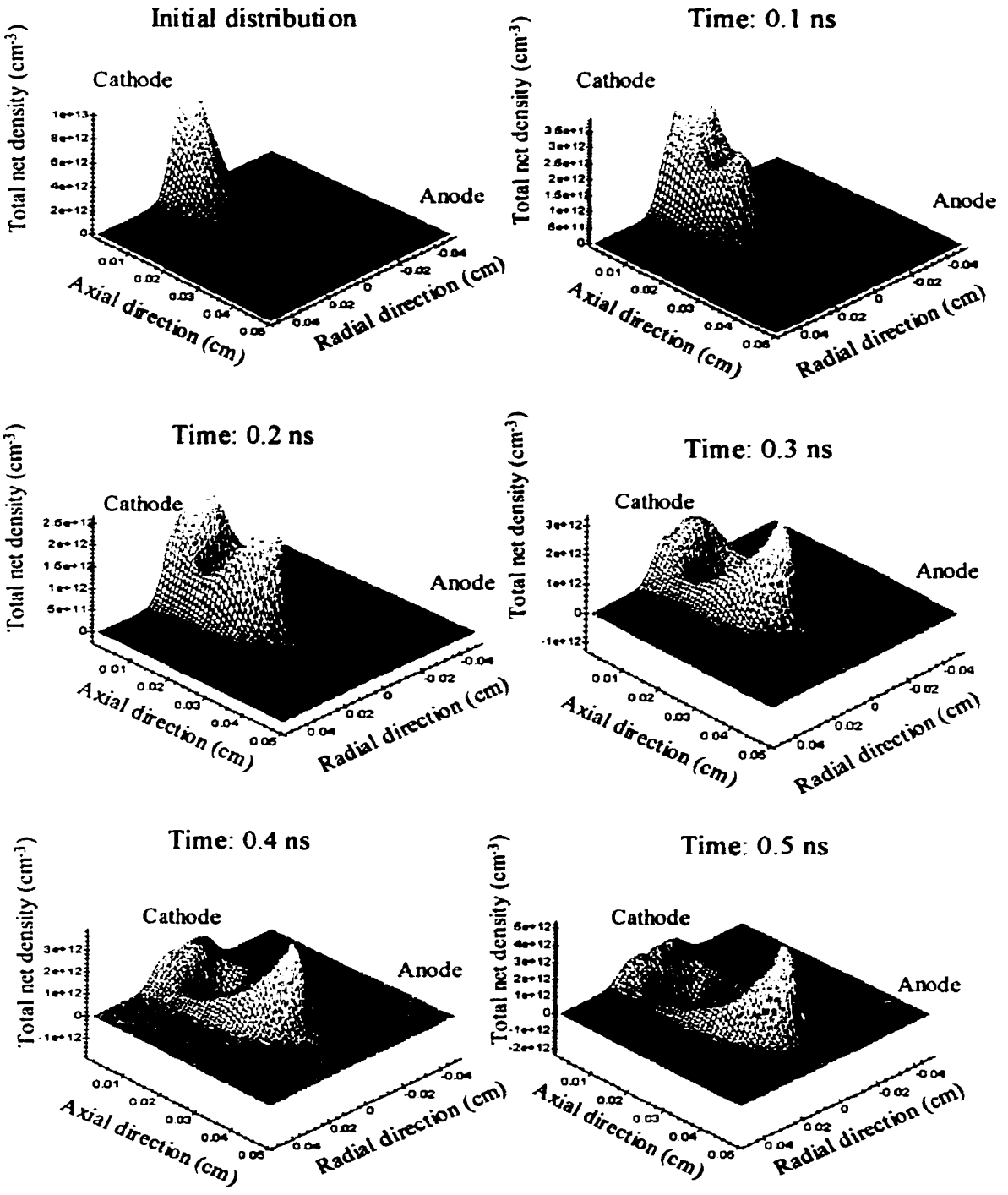

Figure 3.15 Total net charge density distribution at different times of discharge propagation.

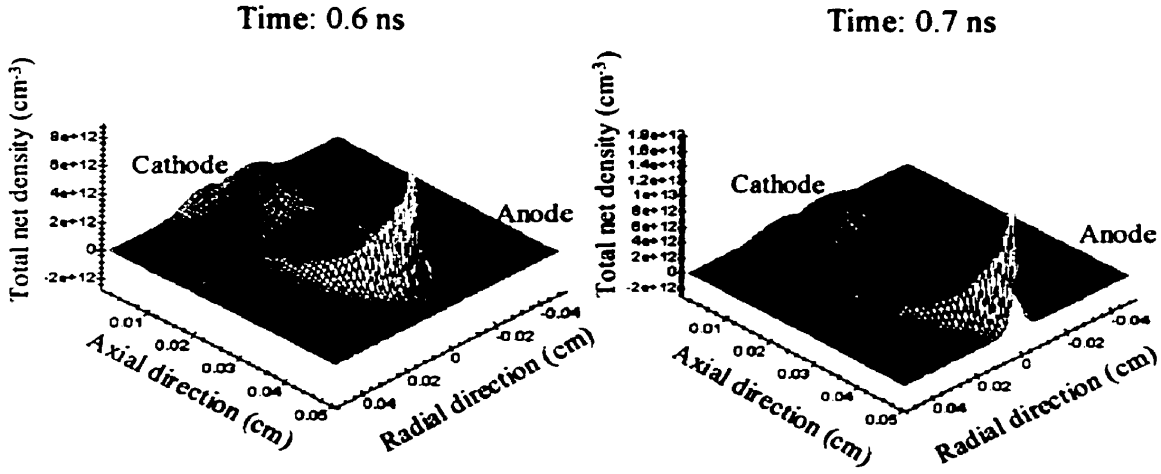

Figure 3.15 (continued) Total net charge density distribution at different times of discharge propagation.

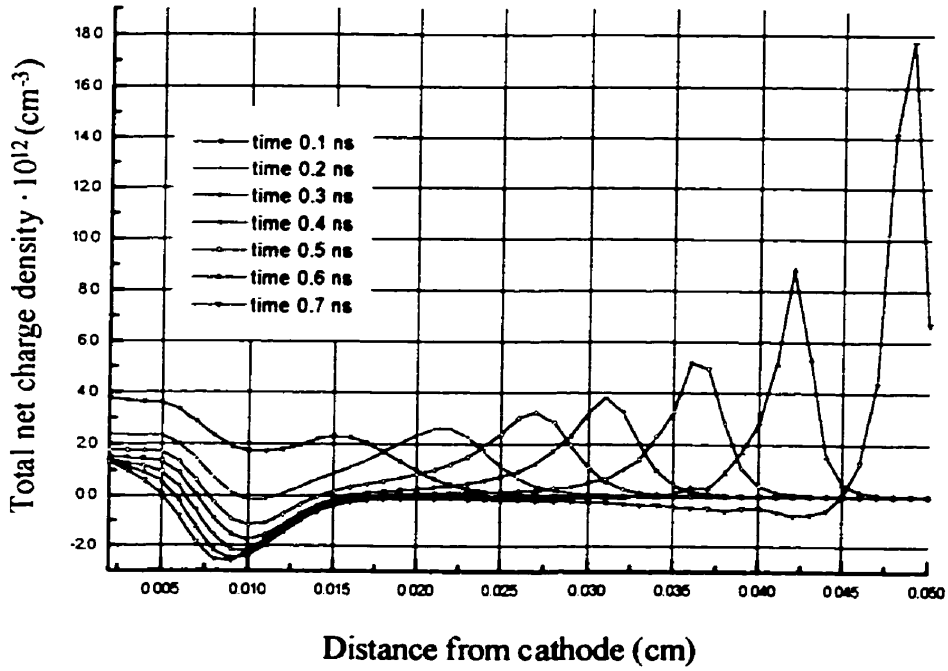

Figure 3.16 Total net charge density profile vs time.

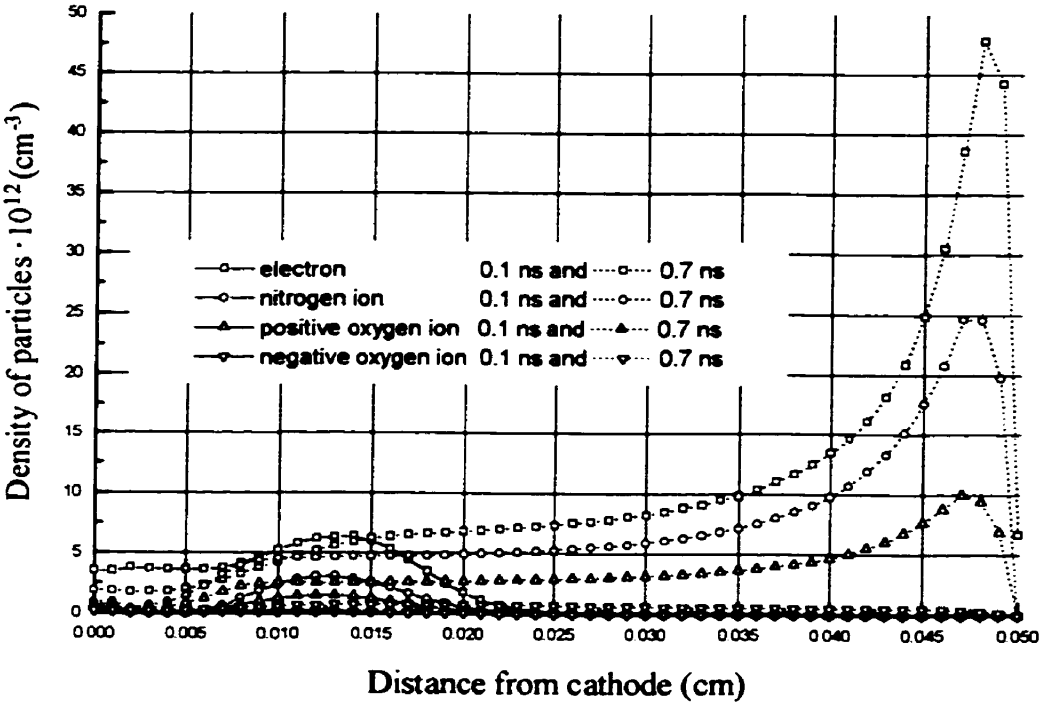

Figure 3.17 Density distribution profile for different kinds of charged particles at t=0.1 ns and t=0.7 ns.

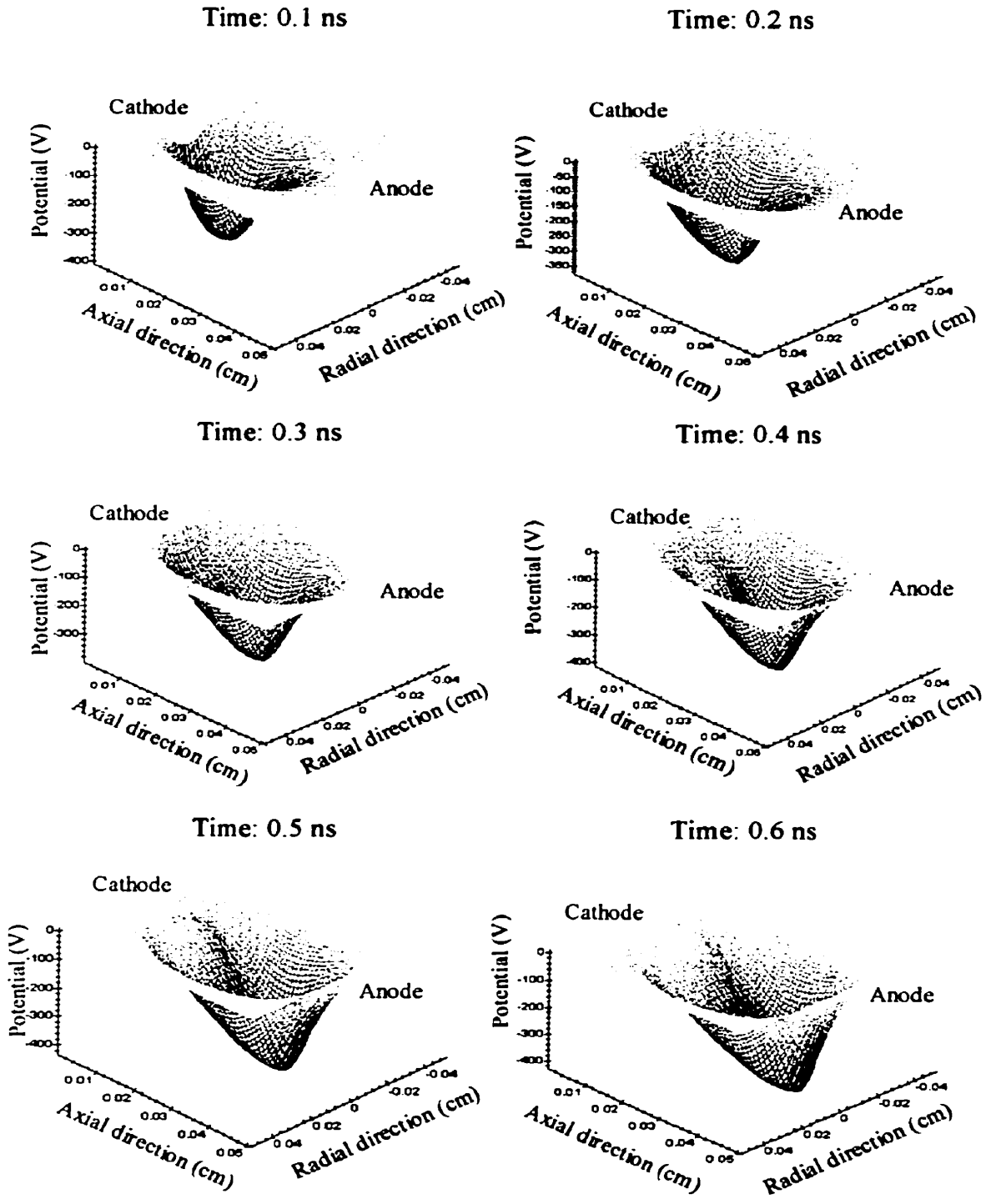

Figure 3.18 Potential due to space charge in the gap at different times of discharge propagation.

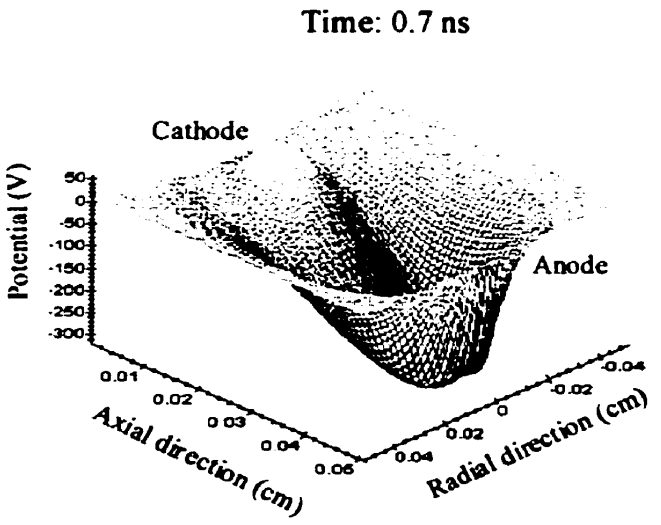

Figure 3.18 (continued) Potential due to space charge in the gap at different times of discharge propagation.

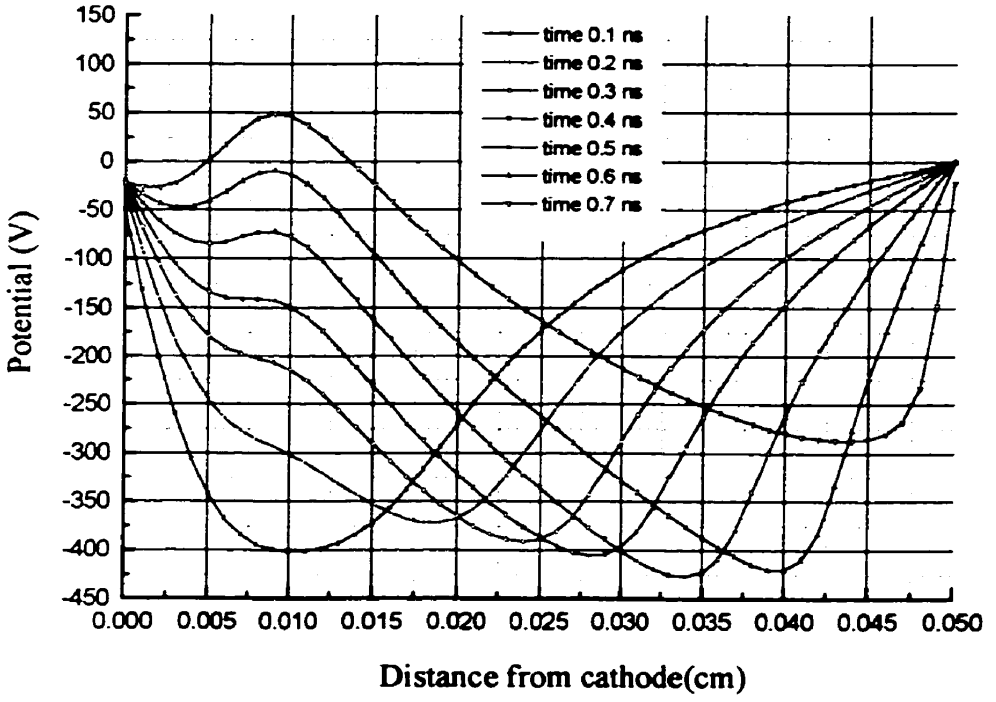

Figure 3.19 Potential profile due to space charge in the gap vs time.

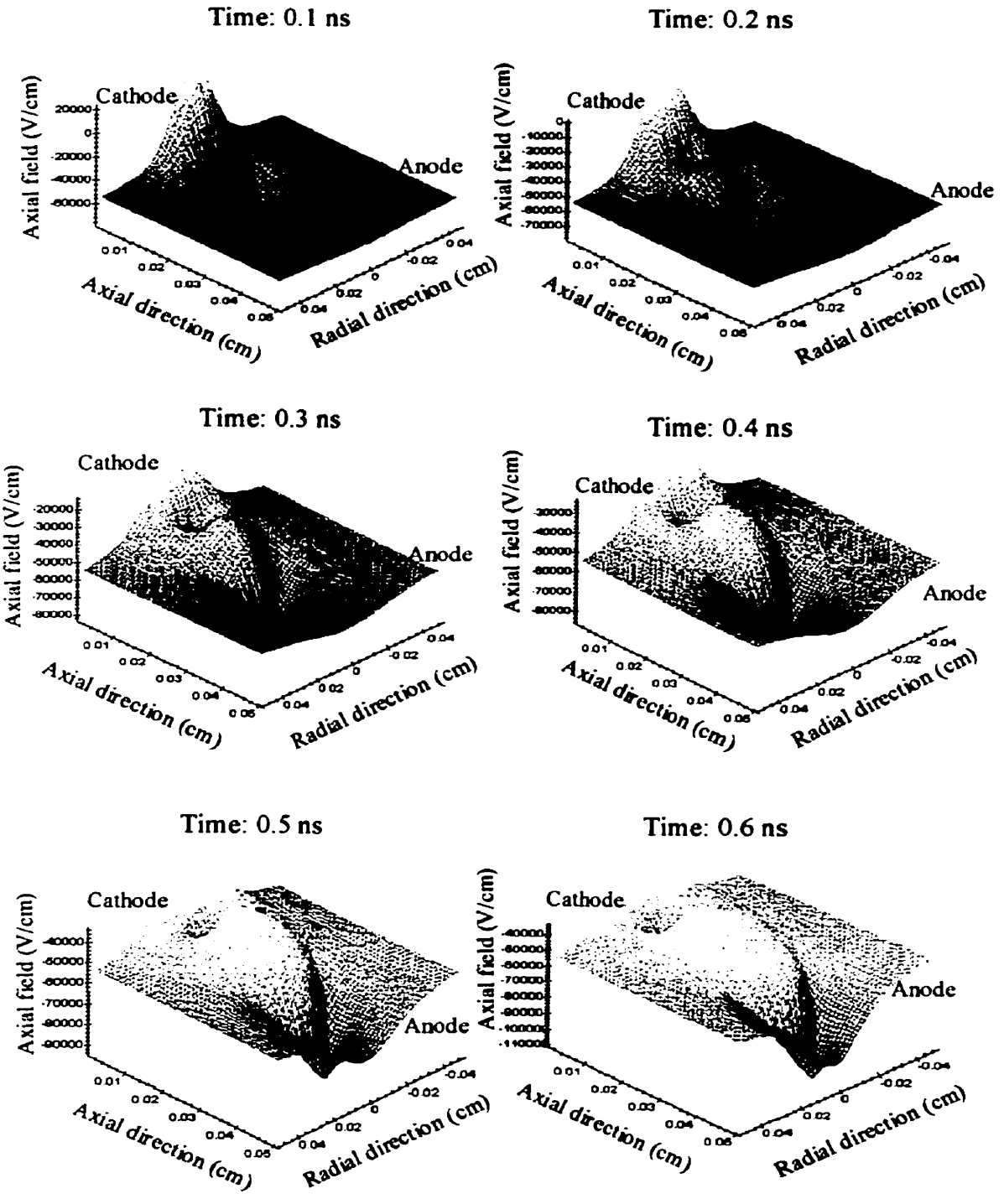

Figure 3.20 Axial field in the gap at different times of discharge propagation.

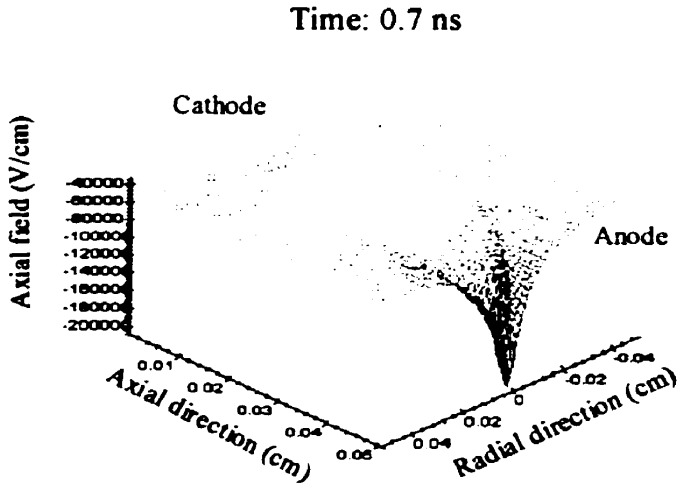

Figure 3.20 (continued) Axial field in the gap at different times of discharge propagation.

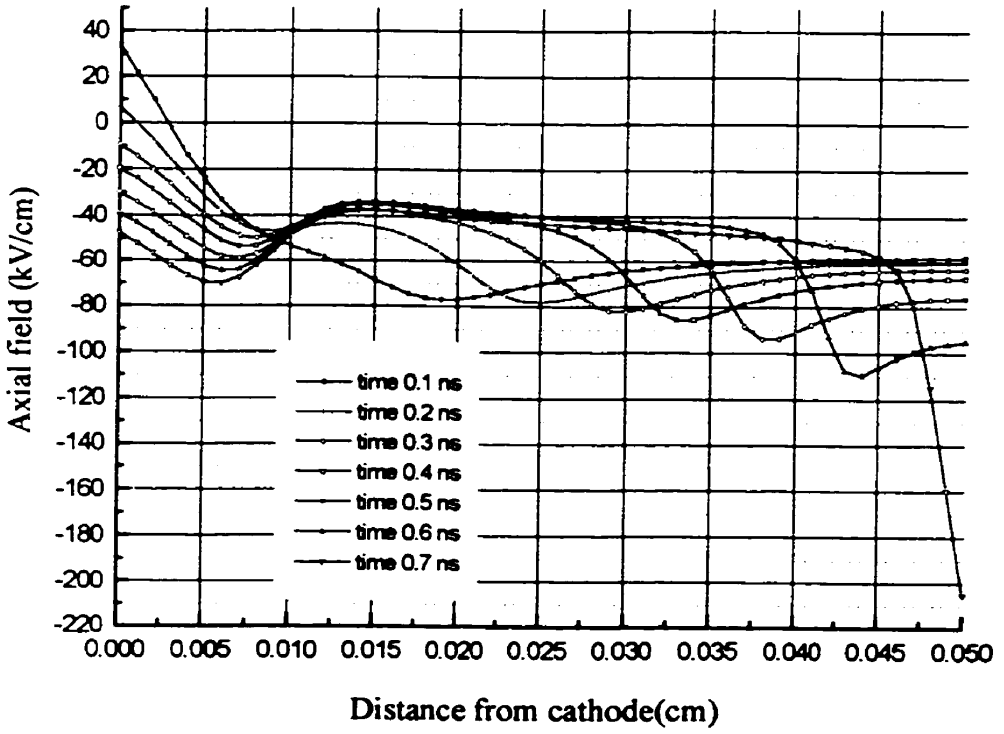

Figure 3.21 Axial field distribution profile vs time.

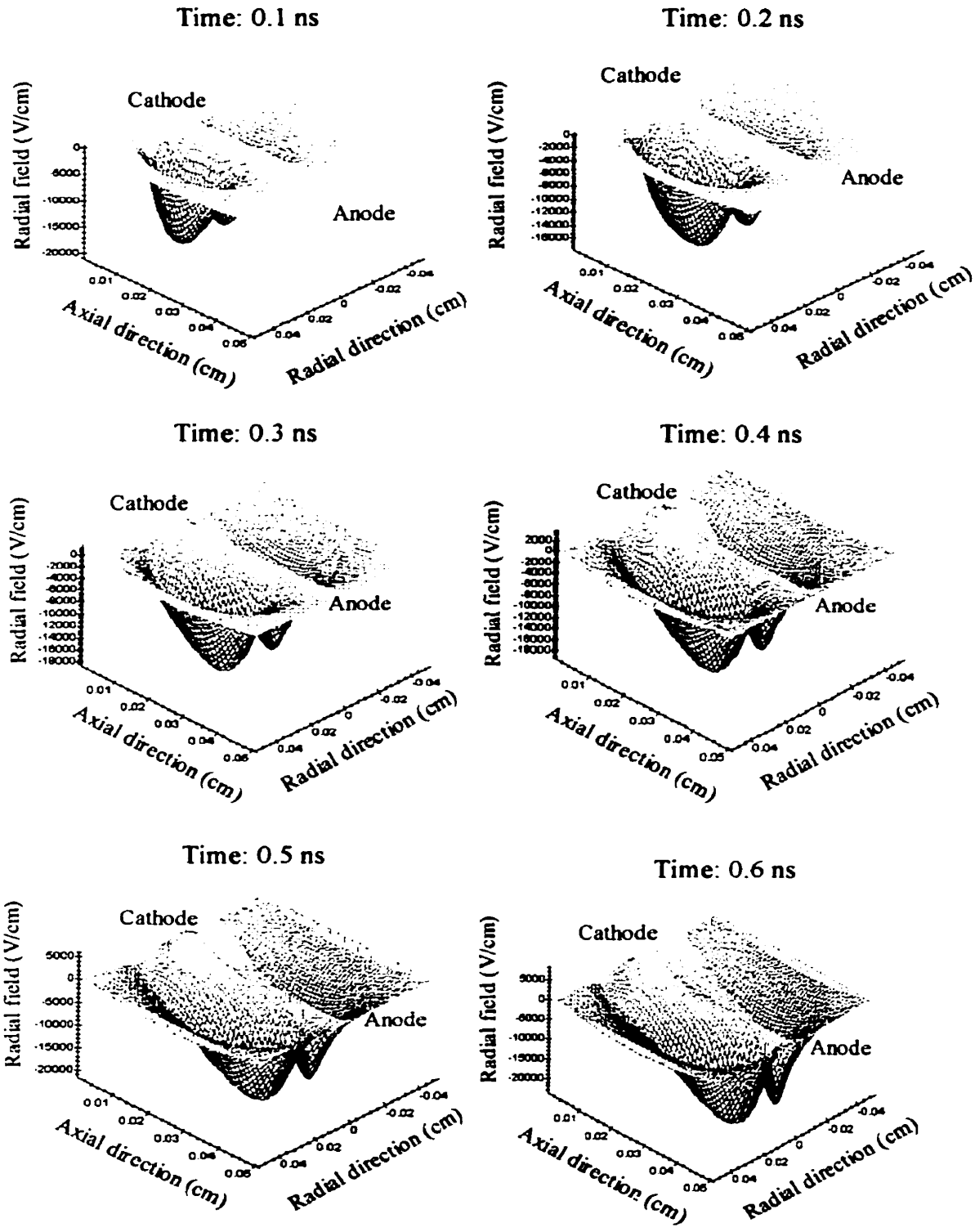

Figure 3.22 Radial field in the gap at different times of discharge propagation.

Time: 0.7 ns

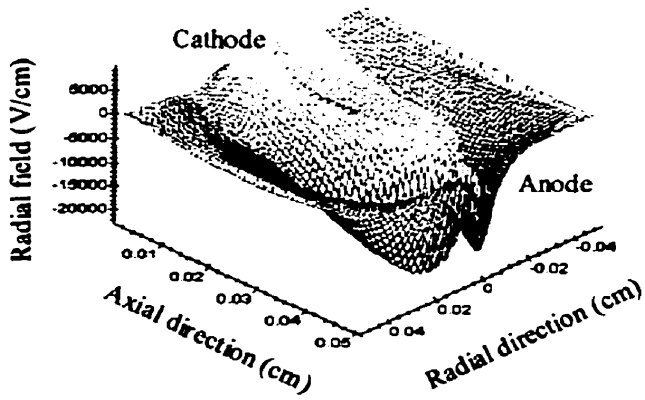

Figure 3.22 (continued) Radial field in the gap at different times of discharge propagation.

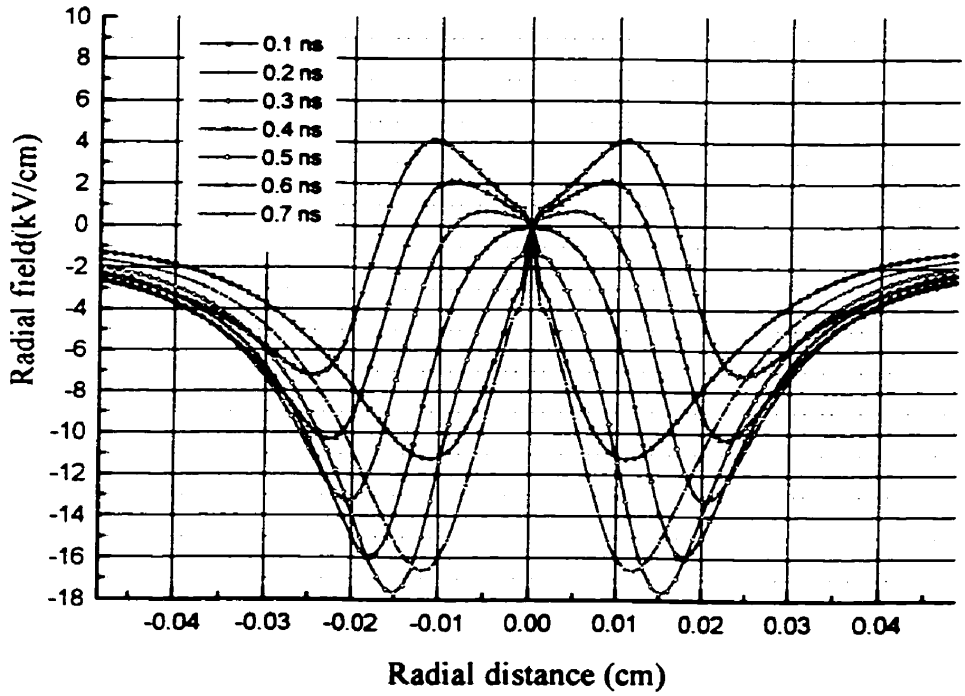

Figure 3.23 Radial field development at different times of discharge propagation. Distance from cathode is 0.02 cm.

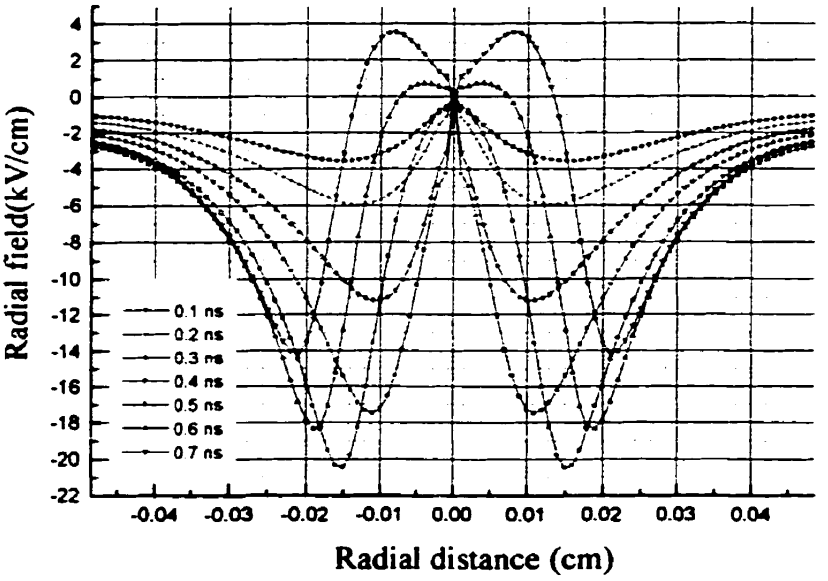

Figure 3.24 Radial field development at different times of discharge propagation. Distance from cathode is 0.03 cm.

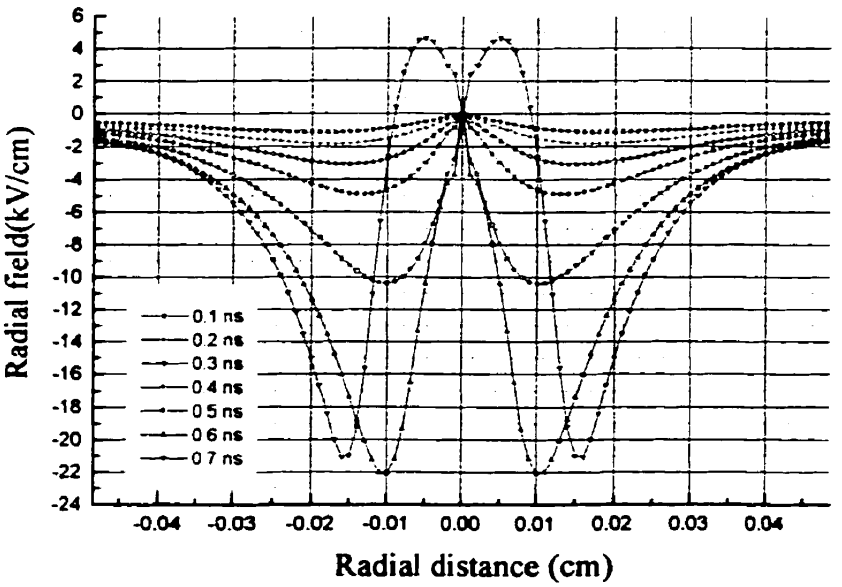

Figure 3.25 Radial field development at different times of discharge propagation. Distance from cathode is 0.04 cm.

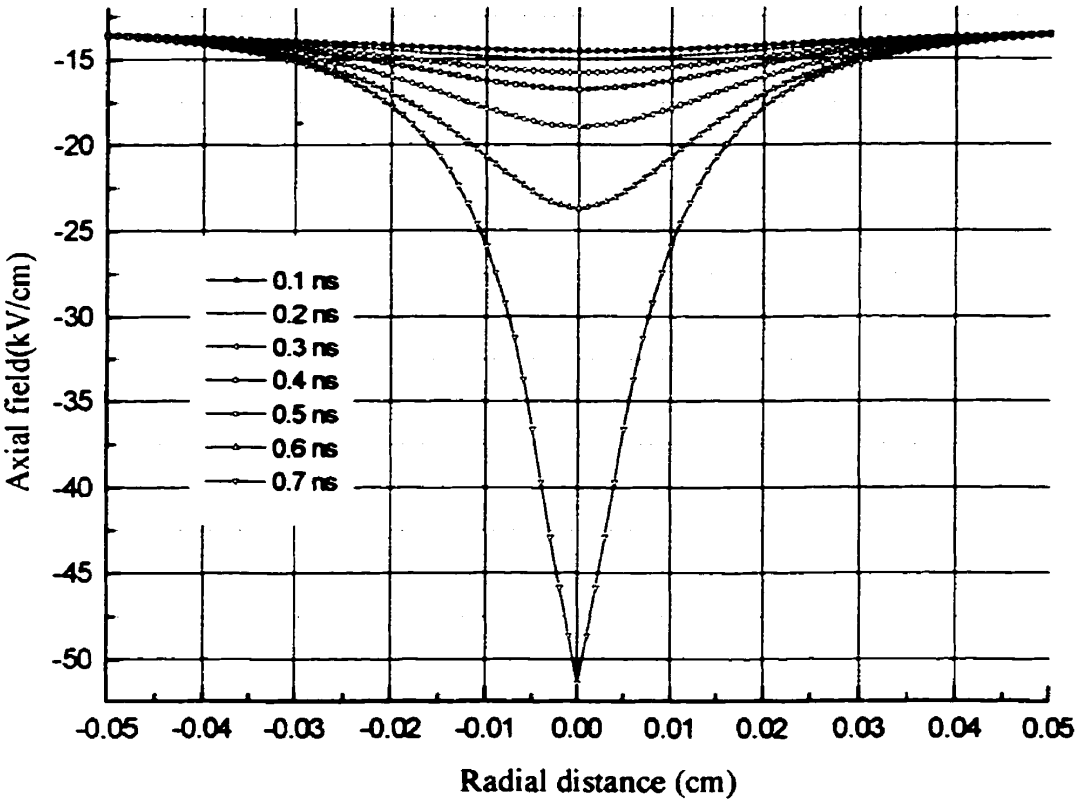

Figure 3.26 Axial induced field inside of dielectric at different times of discharge propagation. The values of the axial field inside the dielectric skin layer were calculated from the formula: $E_r(d^-) = \frac{\sigma}{\varepsilon_0 \cdot \varepsilon_r} + \frac{E_r(d^-)}{\varepsilon_r}$

CHAPTER IV

THE EFFECT OF SURFACE CHARGE ACCUMULATION

This chapter discusses the effects of surface degradation of dielectrics caused by the effect of partial discharges. It includes a brief review of published experimental results [2,3], a theoretical approach to the effects of dielectric surface inhomogeneities on charge accumulation [48], along with some original simulation results.

4.1 The influence of partial discharge plasma on dielectric surface degradation

Hudon, Bartnikas and Wertheimer have studied physico-chemical surface modifications of epoxy resin-coated electrodes submitted to partial discharges [2,3]. This work has shown that degradation of the epoxy surface is accompanied by drastic modifications in the discharge behavior, and of the specimen's surface conductivity.

The degradation of the virgin surface first results from high-amplitude pulse discharges which can attain several 100 pC and which form narrow luminous channels. This kind of discharge leads to extensive surface damage, both chemical changes and mechanical roughening. The production of low molecular weight organic oxidation products such as formic, glycolic and glyoxalic acids and other products such as aldehydes and alcohols were demonstrated [2,3]. Since the electrical conductivity of the

above-mentioned acids is much higher than that of the epoxy matrix, this degradation process enhances the surface conductivity of the dielectric after PD exposure, by more than six orders of magnitude [2,3]. As already mentioned, these chemical transformations are also found to be accompanied by modifications of the surface morphology [8].

The charge redistribution process caused by physical and chemical modifications of the dielectric surface are felt to be responsible for the appearance of a new form of discharge, namely a glow discharge. An intermediate state, comprising a mixture of spark and glow discharges is known as a pseudoglow discharge. Glow and pseudoglow were first observed in 1968 by Bartnikas [49] while investigating discharge phenomena of short gaps in helium. Pseudoglow discharges exhibit pulses with amplitudes in the range of 1-10 pC, compared to values inferior to 1 pC for a true glow regime. Both these forms of discharges have been found to lead to formation and growth of oxalic acid crystals in the presence of O_2 [2,3].

4.2 Effect of dielectric surface inhomogeneity on the charge distribution

Jing has shown that field theory, when applied to lossy and inhomogeneous media, predicts the possible occurrence of surface charge accumulation [48]. We present here part of his work which is relevant to our studies.

The electric field $\bar{E}$ and the current density $\bar{J}$ are linked by Ohm's law:

$$\bar{J} = \sigma \bar{E} \tag{4.1}$$

where σ is the electrical conductivity of the material.

Gauss's theorem tells us that:

$$\nabla \bullet \bar{D} = \nabla \bullet \varepsilon \bar{E} = \rho \tag{4.2}$$

where $\bar{D}$ represents the electric flux density, ε $(\varepsilon = \varepsilon_O \varepsilon_r)$ is the dielectric permittivity, and ρ is the free space charge density. The connection between $\bar{J}$ and ρ is expressed by:

$$\nabla \bullet \bar{J} + \frac{\partial \rho}{\partial t} = 0 \tag{4.3}$$

It follows from Eqs. 4.1 and 4.3 that:

$$\bar{E} \cdot \nabla \sigma + \sigma \nabla \bullet \bar{E} = -\frac{\partial \rho}{\partial t} \tag{4.4}$$

Expanding Eq. 4.2 yields:

$$\bar{E} \cdot \nabla \varepsilon + \varepsilon \nabla \bullet \bar{E} = \rho \tag{4.5}$$

Elimination of $\nabla \bullet \bar{E}$ between Eqs. 4.4 and 4.5 gives [48,50]:

$$\frac{\partial \rho}{\partial t} + \rho \frac{\sigma}{\varepsilon} = \sigma \bar{E} \left[\frac{\nabla \varepsilon}{\varepsilon} - \frac{\nabla \sigma}{\sigma} \right] \tag{4.6}$$

which admits as a solution:

$$\rho = \varepsilon \vec{E}\left[\frac{\nabla\varepsilon}{\varepsilon} - \frac{\nabla\sigma}{\sigma}\right]\left(1 - \exp\left[-t/\tau\right]\right) \tag{4.7}$$

where τ is a time constant given by:

$$\tau = \varepsilon/\sigma \tag{4.8}$$

For a virgin epoxy surface, we have $\sigma_0 = 9 \times 10^{-17}$ S/cm, and the time constant is so large that Eq. 4.7 reduces to [48]:

$$\rho = \varepsilon \vec{E}\left[\frac{\nabla\varepsilon}{\varepsilon} - \frac{\nabla\sigma}{\sigma}\right] \tag{4.9}$$

It follows from Eq. 4.9 that possible charge accumulation occurs mostly in the 'inhomogeneous' areas of dielectric materials. This process will especially be present at interfaces, including a gas-dielectric boundary, or in the places of different materials interfaces, for example in solid or solid-liquid composites, or in locations of different materials formations due to chemical reactions [3,51,52], e.g. where surface stress induces local changes in σ and ε over time.

4.3 Results of simulation

Novak and Bartnikas have shown that the presence of a dielectric surface affects the mechanism of partial discharges [1]. According to these authors, the effect occurs because charge accumulation on the dielectric surface modifies the electric field distribution in the gap; this may cause a discharge channel to expand over the electrode surface, thereby contributing to forming a glow (or pulseless) discharge. Another interesting aspect of their work is that they have compared the radial distribution of the relative charge density for metal and epoxy-coated electrodes [1]. We have applied our simulation software to this problem to confirm that conducting and insulating electrodes exhibit different axial and radial field distributions, total net density distributions, different time evolutions of the electronic space charges, a deposition of electronic charge on the anode surface, and to calculate the propagation time of the discharge.

The effect of surface charge accumulation was investigated, by using a breakdown model for epoxy resin-coated electrodes (ε_r =4). The initial electron density distribution for the cases of an uncharged anode and a charged one (peak of electronic density n_0=3·10^{12} cm^{-3}, and decay parameter discussed in Section 3.1 δ = 22) are shown in Figs. 4.1 and 4.2, respectively. In the FCT algorithm, surface charge accumulation is made possible by imposing a zero-valued axial component for the drift velocity on the anode surface.

Equations 2.43 and 2.44 were used to compute the total duration of the discharges during a half-cycle of the applied voltage, while Eq. 2.45 yields the time

between two PD pulses. The time between two consecutive discharges increases each time the polarity is reversed (see Fig. 2.1). Therefore, we estimate the average time interval between two consecutive discharges as 1.0113 μs (see Section 2.3). This is three orders of magnitude greater than the discharge propagation time (1.5 ns and 2 ns for the uncharged and charged anode, respectively, as shown in Fig. 4.5). The contribution of the surface charge to the gap voltage was computed directly from Poisson's equation, instead of using Eq. 2.46. The applied voltage was chosen so that the gap voltage was equal to the breakdown value.

Figure 4.3 shows the simulated total net charge density distribution at different times. At t=1 ns, the distributions for charged and uncharged anodes are seen to be very similar, indicating that the charge on the anode does not have a significant effect during the first stages of the discharge. This is further confirmed by Fig. 4.4, which shows that the total space charge does not differ much between the two cases during the first nanosecond or so.

At t=1.5 ns, the total net charge density (uncharged anode) shows a peak at the head of the propagating discharge and a depression in the density surface (Fig. 4.3), while the charged anode case exhibits a homogeneous plateau with more pronounced radial spread. This difference is also reflected in Fig. 4.4, where marked differences are seen to occur for t>1 ns, the space charge being lower in the charged anode case, because of lower field value close to the anode. The presence of surface charge also causes the density of negative charge to rise in the middle of the gap (Fig. 4.3): not only does this cause a drop of the axial field value in the gap (Fig. 4.7, see also [1]), but also

an increase of the radial field, as shown in Figs. 4.8 and 4.9. Thus, the broader radial distribution of space charge (charged anode case) observed in Fig. 4.3 for t=2 ns and t=2.5 ns, and also in Fig. 4.6, is caused not only by charge diffusion but mostly by the high radial field and space charge (Fig. 4.4).

Figure 4.6 also shows that more electronic charge is deposited in the case of an uncharged anode, hence that the space charge remaining in the volume between the two electrodes is greater in the charged anode case. The field close to the surface is decreased due to surface charge accumulation (Fig. 4.7), leading mostly to shallow traps formation at the dielectric surface [46]. The flux of positive ions from the gap to the dielectric surface favors the release of these trapped electrons, and thereby the formation of a glow discharge [46].

Finally, the field modification due to surface charge accumulation also explains why the propagation time of the discharge across the gap rises from 1.5 ns to 2 ns in the uncharged and charged anode cases, respectively (Fig. 4.5).

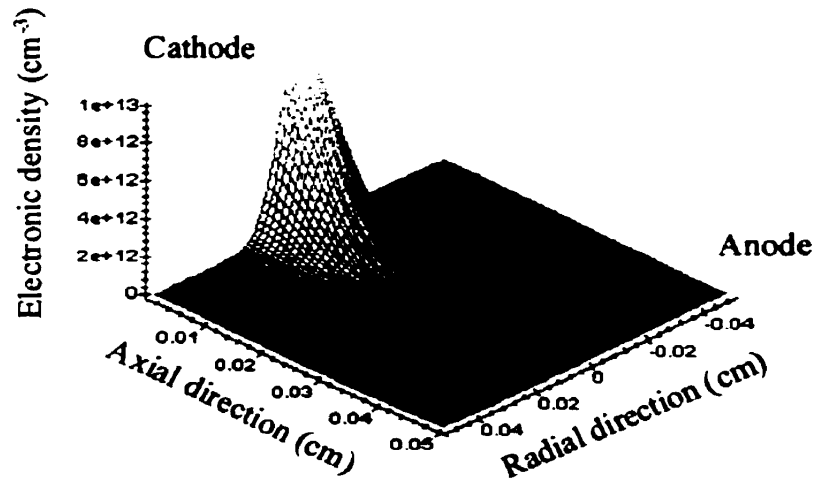

Figure 4.1 Initial conditions ($t=0^+$ ns): distribution of electron density for an uncharged anode and a charged cathode.

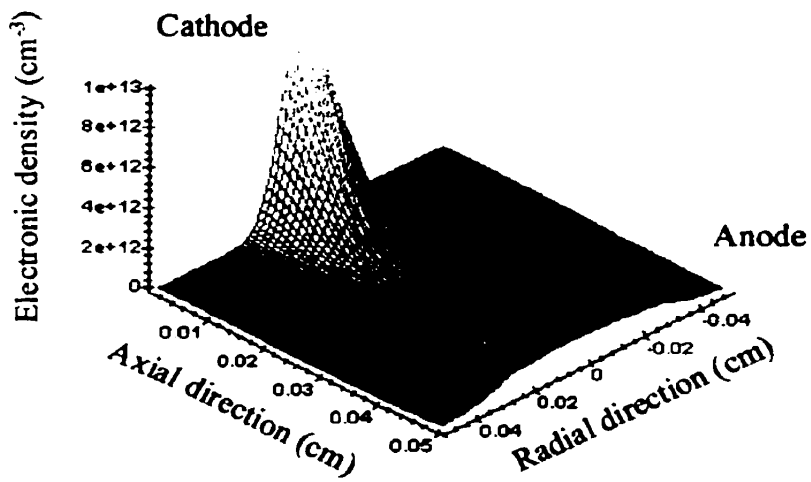

Figure 4.2 Initial conditions ($t=0^+$ ns): distribution of electron density for a charged anode and a charged cathode (peak of electronic density $n_0=3\cdot10^{12}$ cm^{-3}).

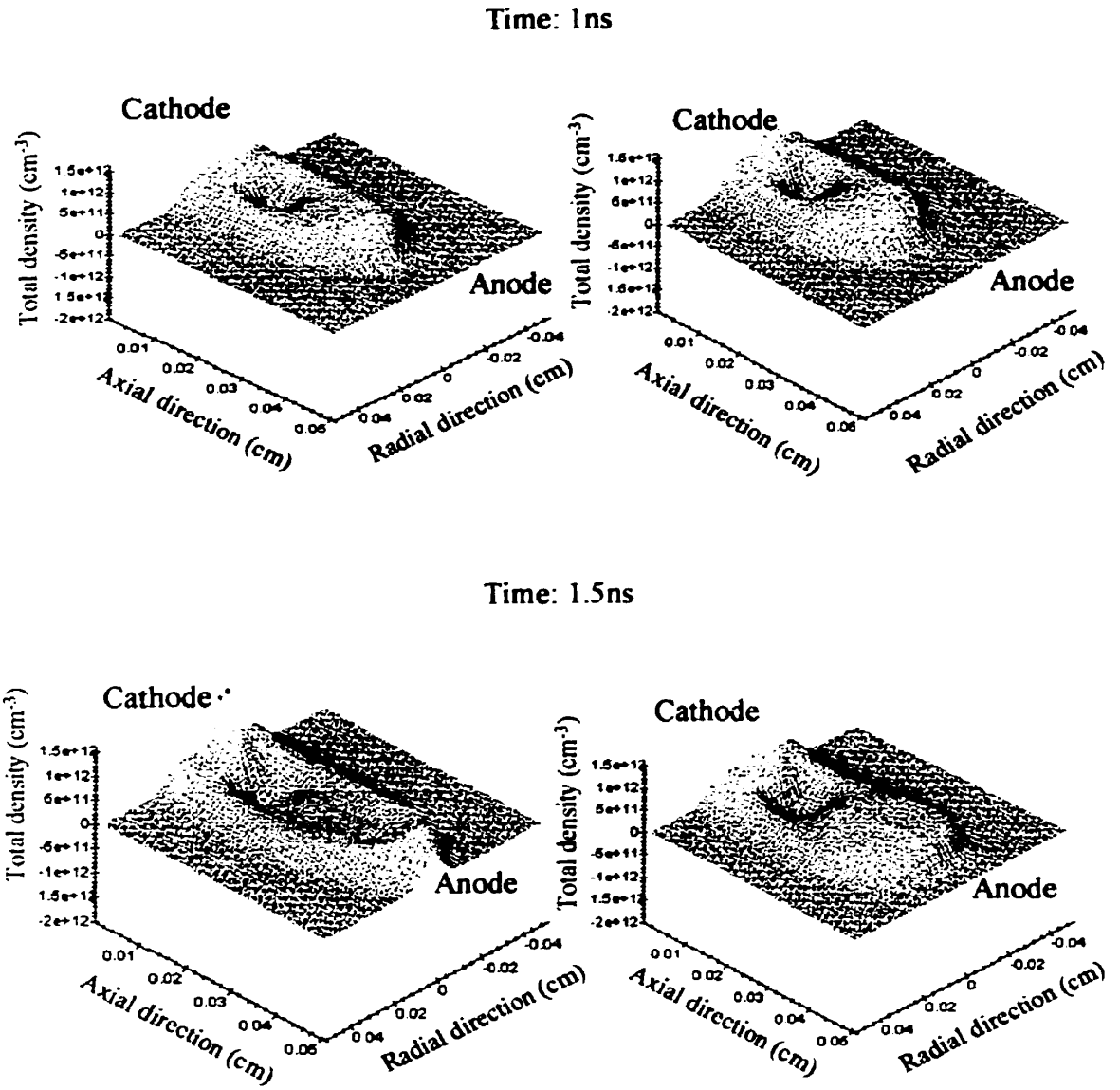

Figure 4.3 Total net charge density distribution for two cases: uncharged anode (left side) and charged anode (right side) at times 1 ns and 1.5 ns.

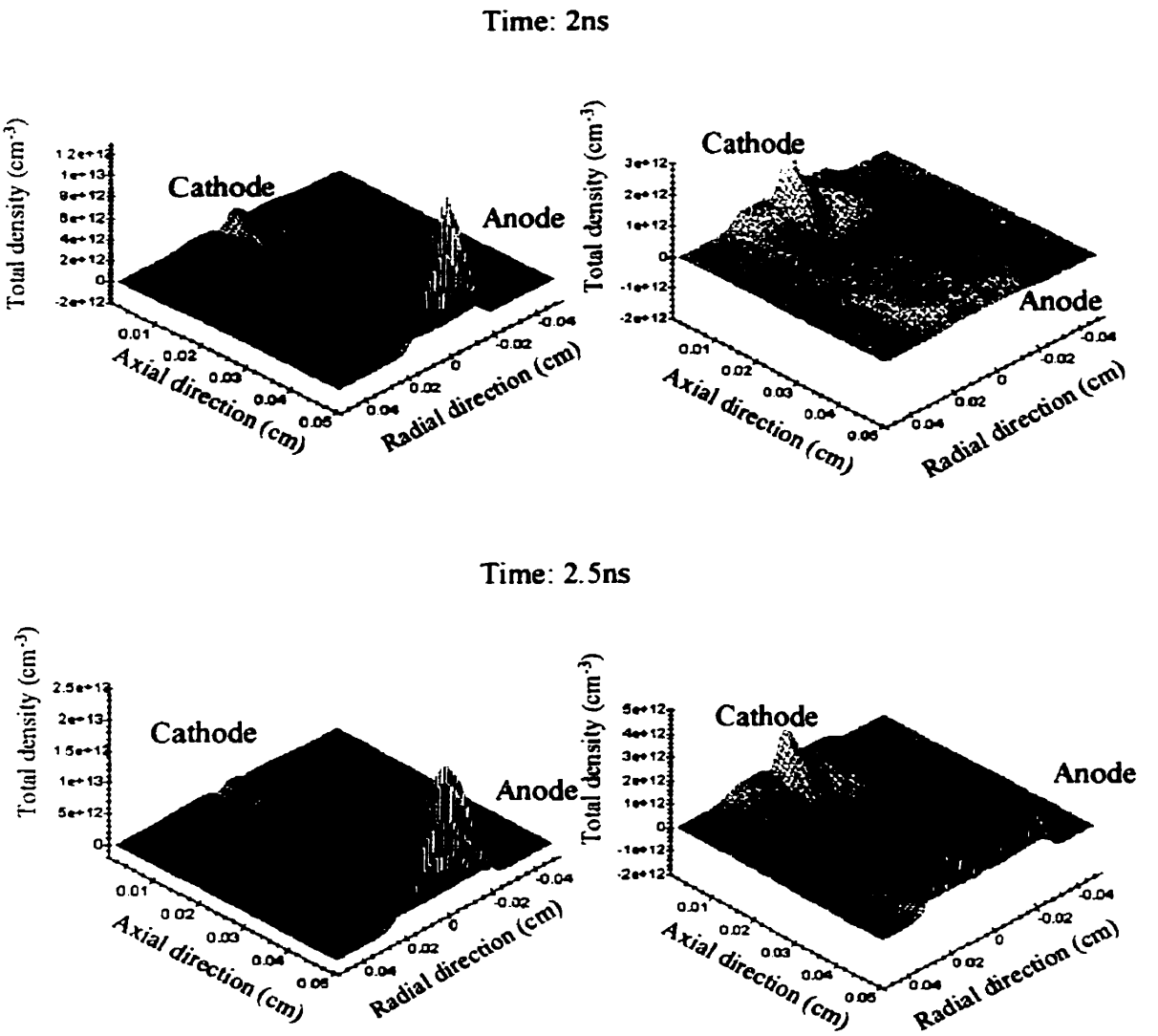

Figure 4.3 (continued) Total net charge density distribution for two cases: uncharged anode (left side) and charged anode (right side) at times 2 ns and 2.5 ns.

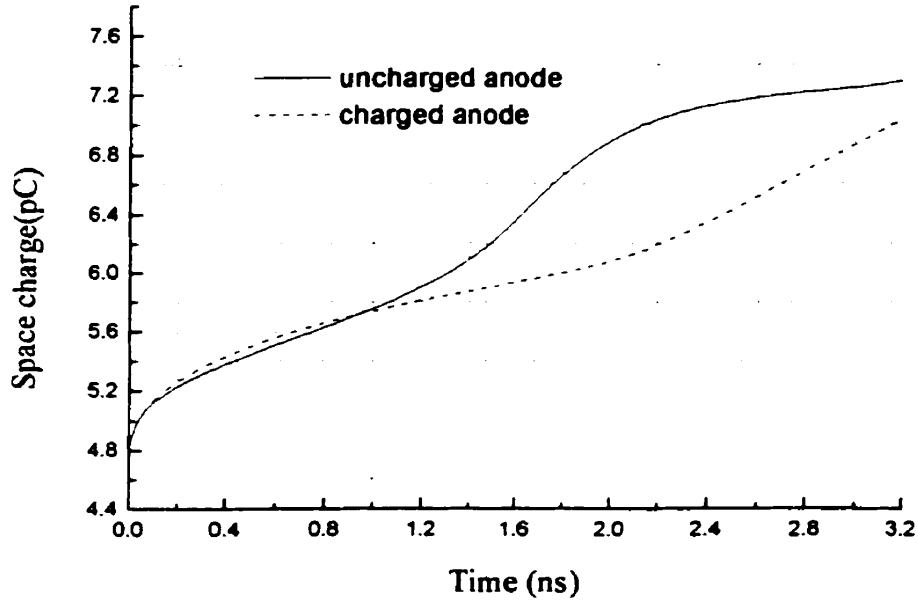

Figure 4.4 Space charge evolution for uncharged and charged anodes.

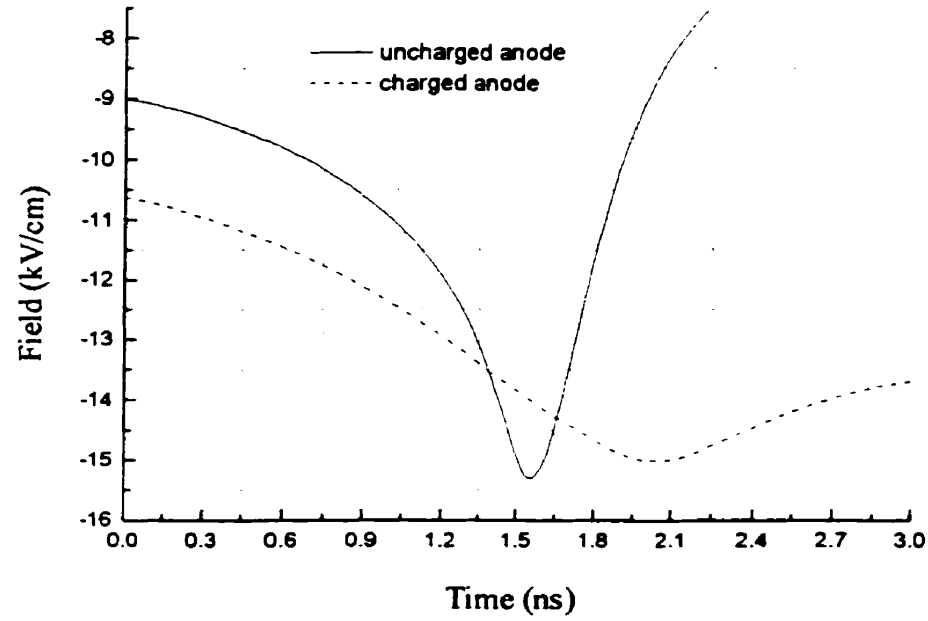

Figure 4.5 As a result of surface accumulation the time of discharge propagation is changed from 1.5 ns to 2 ns.

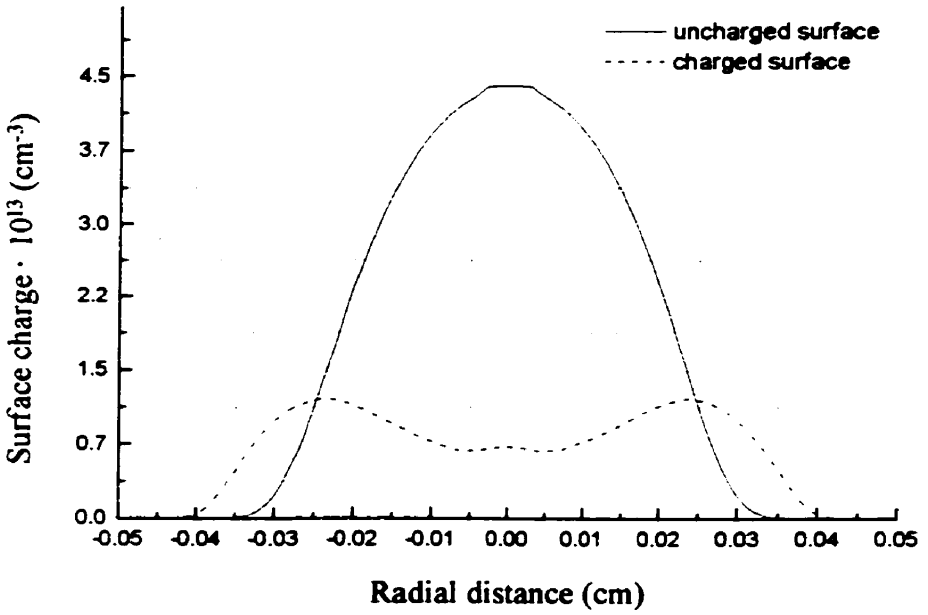

Figure 4.6 Electronic charge deposited on the anode, for the uncharged and charged cases.

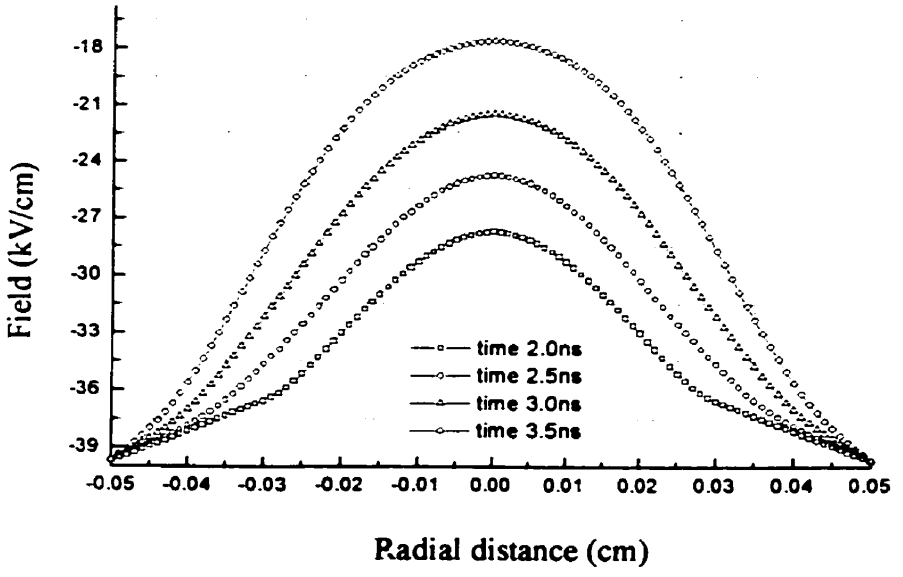

Figure 4.7 Axial field distribution at different times of discharge propagation (distance from cathode 0.04 cm).

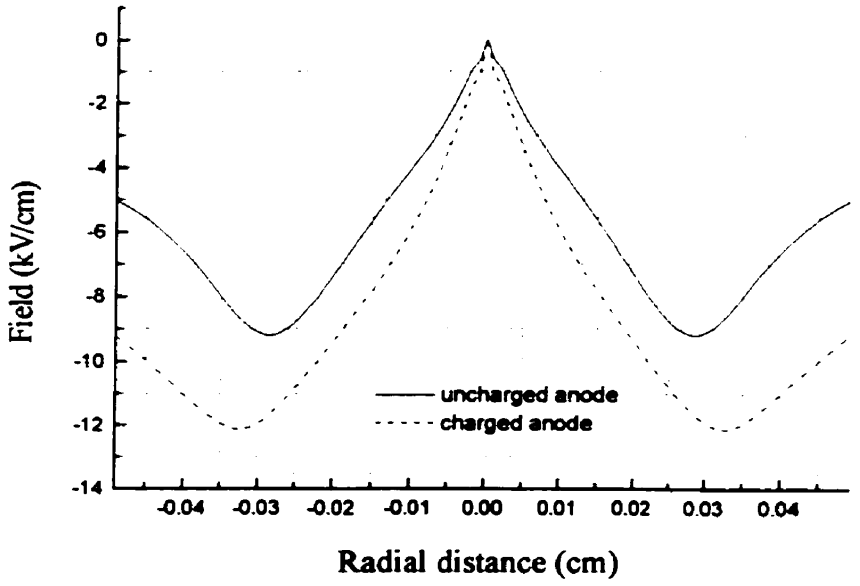

Figure 4.8 Radial field distribution for uncharged and charged anodes. Time is 3.5 ns and distance from cathode is 0.03 cm.

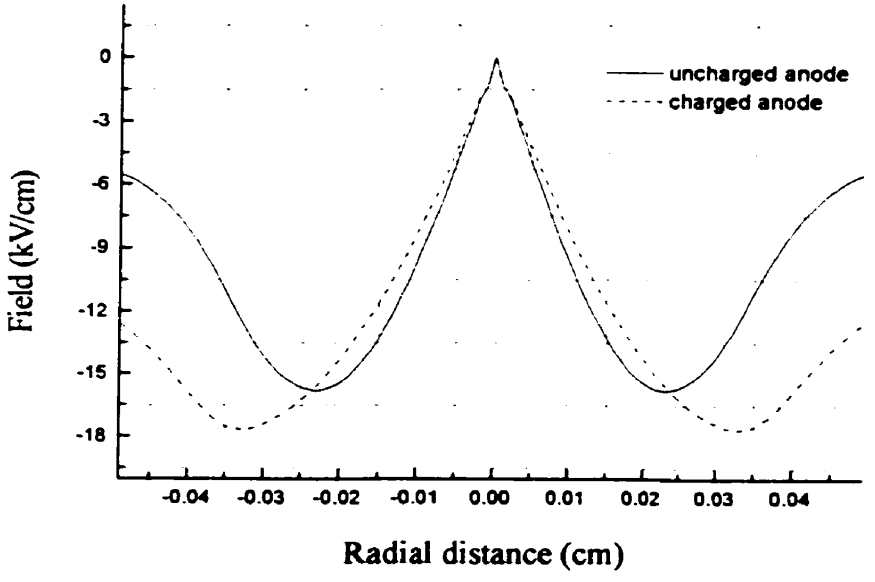

Figure 4.9 Radial field distribution for uncharged and charged anodes. Time is 3.5 ns and distance from cathode is 0.04 cm.

4.4 Simulation of discharge propagation for a negative applied voltage

Here we report the results of simulations performed under the same conditions as in Section 4.3 for uncharged anode case, except that the applied voltage is now negative. The initial electron density distribution is shown in Fig. 4.10 (the same as in Fig. 4.1). Figure 4.11 shows the distribution of a total net charge density in the gap at times t=1 ns and 1.5 ns. Those results are identical to ones for the case of a positive applied voltage in Fig. 4.3. The evolution of the space electronic charge in Fig. 4.12 is the same as for the electronic charge calculated in Section 4.3 (Fig. 4.4). Thus, the presented results of simulation prove us the validity of the FCT algorithm described in Section 2.1.1.

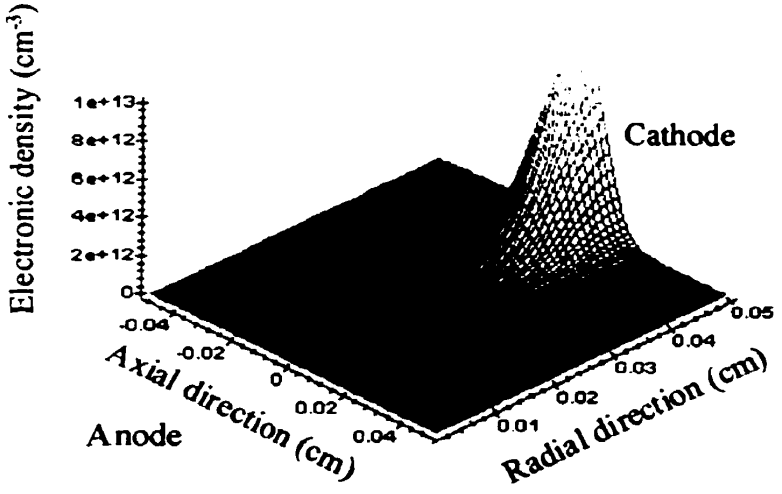

Figure 4.10 Initial conditions ($t=0^+$ ns): distribution of electron density for a negative applied voltage.

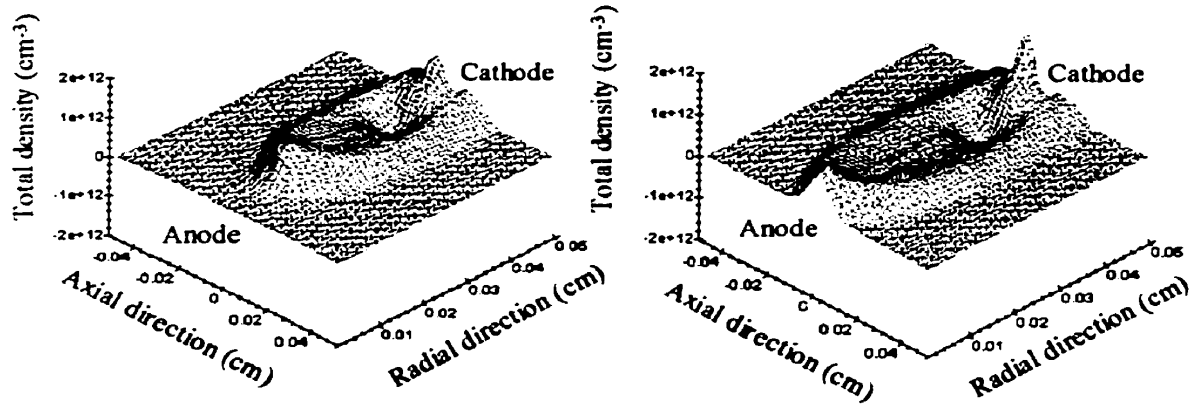

Figure 4.11 Total net charge density distribution for a negative applied voltage at times 1 ns (left side) and 1.5 ns (right side).

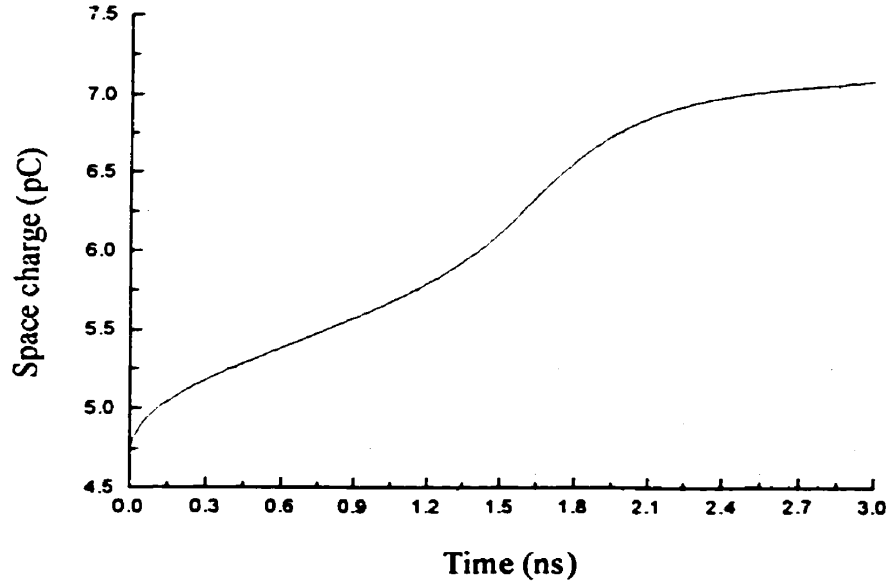

Figure 4.12 Space charge evolution for a negative applied voltage.

CHAPTER V

EFFECTS OF CHARGE DECAY ON THE ANODE SURFACE

We now report computations, which illustrate the effect on PD of charge decay on the anode surface. For this purpose, we use the exact analytical solution proposed by Somerville and Vidaud [53] for the spreading of surface charge by ohmic conduction. This model is applied to the case of a plane interface between two isotropic insulators (epoxy and air, say), each having zero bulk conductivity. In addition, we assume that an arbitrary charge distribution, due to the formation of localised degradation products having high electrical conductivity, is present on the solid dielectric surface [2].

5.1 Estimation of charge spreading time

The analytical solutions for two cases; namely a strip (width x = $2a$, and infinite length) and a square (width x = y = $2a$) of surface charges, were applied to evaluate the charge spreading time, as follows: the time-dependent charge distribution for a strip of charge is given by [53]:

$$\rho_s(x,t) = \frac{Q(x)}{\pi}\left[\arctan\left(\frac{x+a}{\upsilon t}\right) - \arctan\left(\frac{x-a}{\upsilon t}\right)\right]_{t\geq 0} \tag{5.1}$$

where $Q(x)$ is the charge distribution:

$$Q(x) = \begin{cases} Q_s, & -a \le x \le a \\ 0, & \text{elsewhere} \end{cases} \tag{5.2}$$

For the second case, where surface charge has a square form, an analytical solution is:

$$\begin{aligned} \rho_s(x,t) = \frac{Q(x)}{\pi}[&\arctan\left(\frac{(y-a)(x-a)}{\upsilon t[(x-a)^2+(y-a)^2+\upsilon^2 t^2]^{\frac{1}{2}}}\right) \\ &+\arctan\left(\frac{(y+a)(x+a)}{\upsilon t[(x+a)^2+(y+a)^2+\upsilon^2 t^2]^{\frac{1}{2}}}\right) \\ &-\arctan\left(\frac{(y+a)(x-a)}{\upsilon t[(x-a)^2+(y+a)^2+\upsilon^2 t^2]^{\frac{1}{2}}}\right) \\ &-\arctan\left(\frac{(y-a)(x+a)}{\upsilon t[(x+a)^2+(y-a)^2+\upsilon^2 t^2]^{\frac{1}{2}}}\right)]_{t\ge 0}, \end{aligned} \tag{5.3}$$

where charge distribution $Q(x)$ is given by:

$$Q(x) = \begin{cases} Q_s, & -a \le x \le a \quad \text{and} \quad -a \le y \le a \\ 0, & \text{elsewhere} \end{cases} \tag{5.4}$$

The effective normal velocity, υ, is expressed by:

$$\upsilon = \frac{\sigma}{2(\varepsilon_0 \varepsilon_{eff})}, \tag{5.5}$$

where σ is the surface conductivity, and the effective relative permittivity ε_{eff} is given by:

$$\varepsilon_{eff} = \frac{1}{2}(\varepsilon_1 + \varepsilon_2) \tag{5.6}$$

In the present case, ε_1=1 (air) and ε_2=4 (epoxy resin). Now, we evaluate the time of charge spreading for the case of exponential charge redistribution (due to decay of the above-mentioned strip and square charge distributions forms). The initial charge distribution (a=0.015 cm) in Fig. 5.1 has a decay parameter δ=19 (see Section 3.1) in the x direction at the initial time t=0, where δ equals to the grid index for radial direction, where the peak of electronic density is decreased by 1/*e* (see Section 3.1).

The charge spreading, computed from Eqs. 5.1 and 5.3 for a surface conductivity of 10^{-9} S at any particular instant t>0, is shown in Fig. 5.1 (the curves are chosen so that Δδ=1), where the effect of the external field has not been included. For the above-cited value of surface conductivity ($\sigma=10^{-9}$ S), the time between two neighboring curves in Fig. 5.1 is Δt=0.7 μs (for the square charge distribution) and Δt=0.5 μs (for the strip of charge), which is much less than a half-period of the applied voltage. For surface conductivity of $9\cdot10^{-17}$ S (virgin epoxy), we have Δt=4 s for a square of charge, and Δt=3 s for a strip of charge, respectively. The initial charge width influences the spreading time, Δt, as follows: for a=0.005, 0.015 and 0.020 cm, Δt=0.46, 0.7 and 0.8 μs (square distribution), and Δt=0.35, 0.5 and 0.6 μs (strip distribution), respectively. So, we can conclude that the distribution of surface charge with time strongly depends on σ and only slightly on the initial form and width of the surface charge.

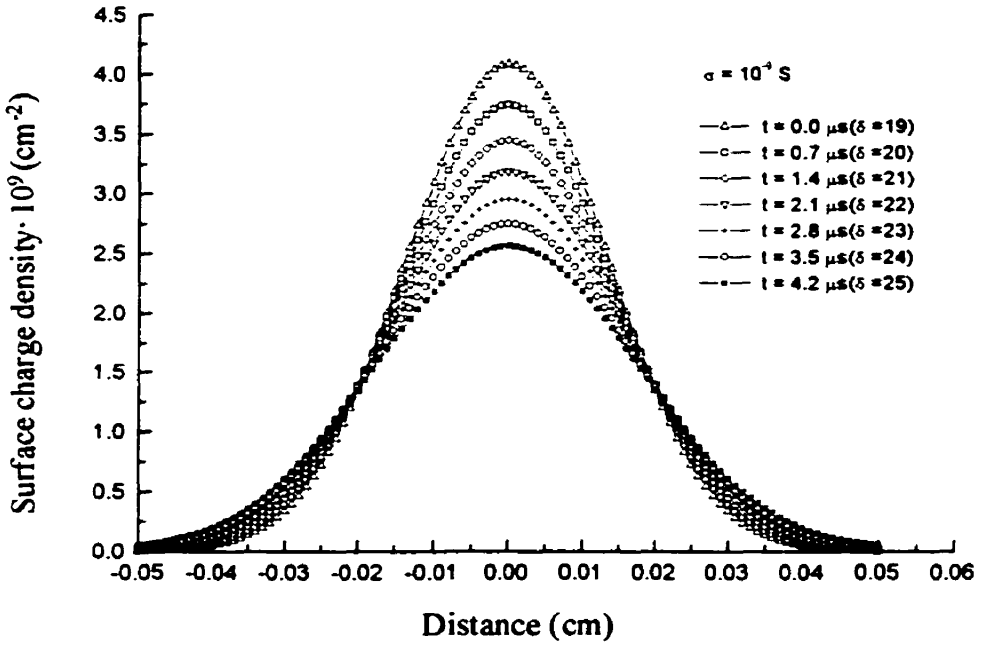

Figure 5.1 Kinetic model of surface charge spreading on the anode (a=0.015 cm).

5.2 Results of simulation

The results of simulation for the various parameters of interest, relating to each case of charge spreading in Fig. 5.1 ($19 \le \delta \le 25$, $0\ \mu s \le t \le 4.2\ \mu s$), are shown in Figs. 5.2 to 5.7: The charge spreading increases the maximum field value in the gap from 58 kV/cm to 62 kV/cm, as shown in Fig. 5.2, while it decreases the time of discharge propagation by 0.2 ns (Fig. 5.2). Another interesting aspect of our work is that the total electronic charge in the gap is increased (Fig. 5.3), when surface charge spreading occurs. The condition of the charged surface strongly affects the shape of the deposited electronic charge density, as shown in Fig. 5.4; it shows a central minimum in the case t=0 (δ=19), which is replaced by a much smoother, more uniform distribution in the case t=4.2 μs (δ=25).

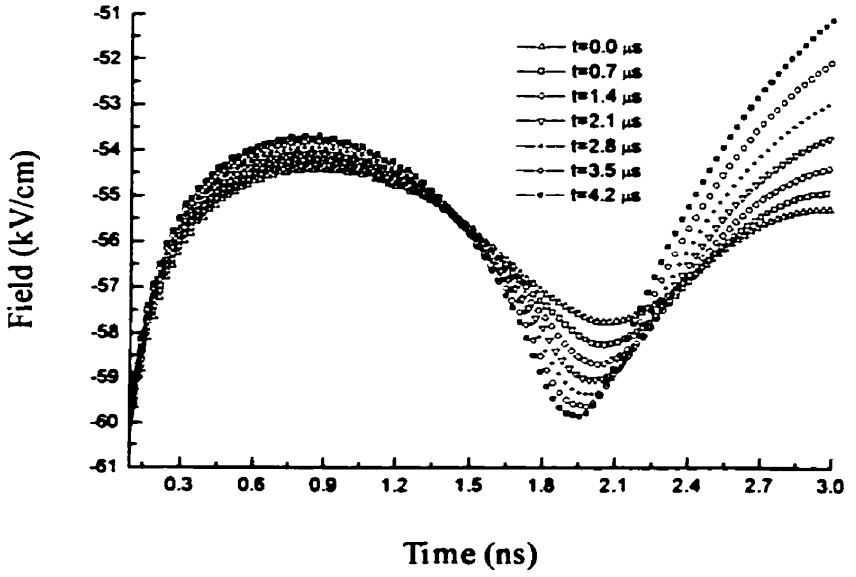

Figure 5.2 Effect of surface charge spreading on maximum axial field value in the gap.

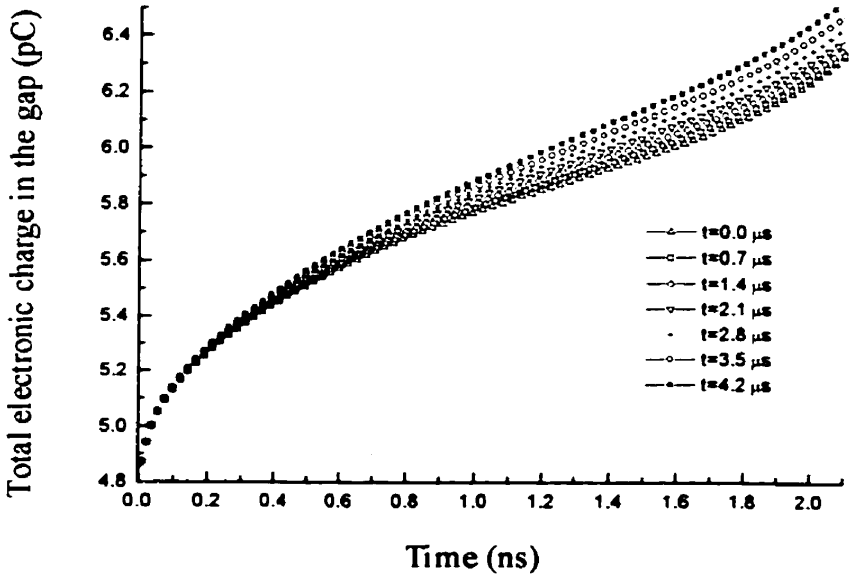

Figure 5.3 Influence of surface charge spreading on the total electronic charge in the volume of the gap.

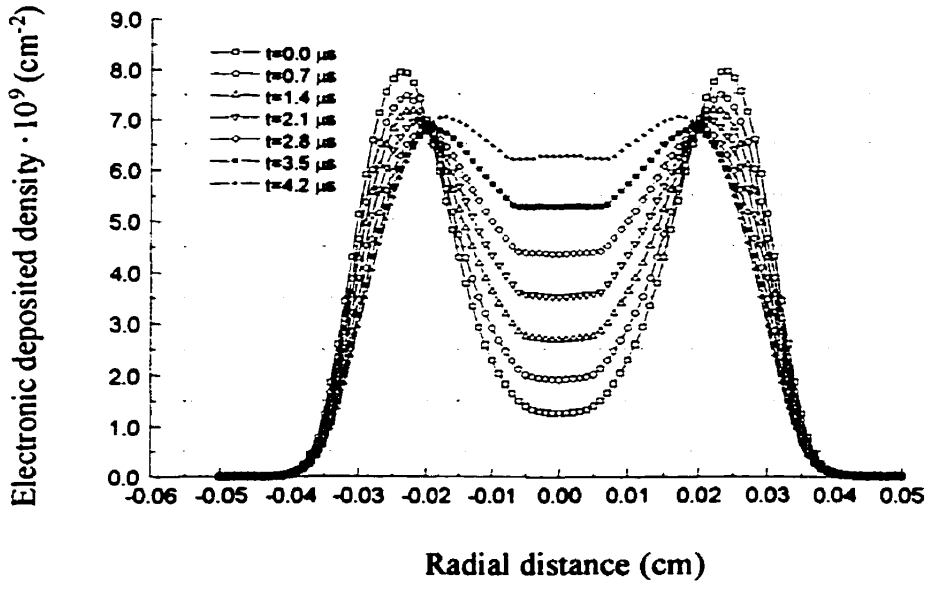

Figure 5.4 Effect of surface charge spreading on the electronic surface charge density deposited on the anode as a result of the discharge in the gap.

We use the so-called charge rings decay model (Fig. 5.5), with initial constant charge density on the anode, and a separation between the charge density peaks in the radial direction (Δr=0.015 cm) to demonstrate the effect of surface charge spreading on deposited charge density. Figure 5.5 shows two initial distributions of the electronic charge density; namely before and after the occurrence of charge spreading (left and right, respectively). The corresponding axial field distributions in the gap due to the two cases of electronic charge density on the anode was computed directly using Poisson's equation, and it is shown in Fig. 5.6. The value of maximum field due to surface charge spreading is decreased from 40 kV/cm to 30 kV/cm and field distribution becomes smoother (Fig. 5.6).

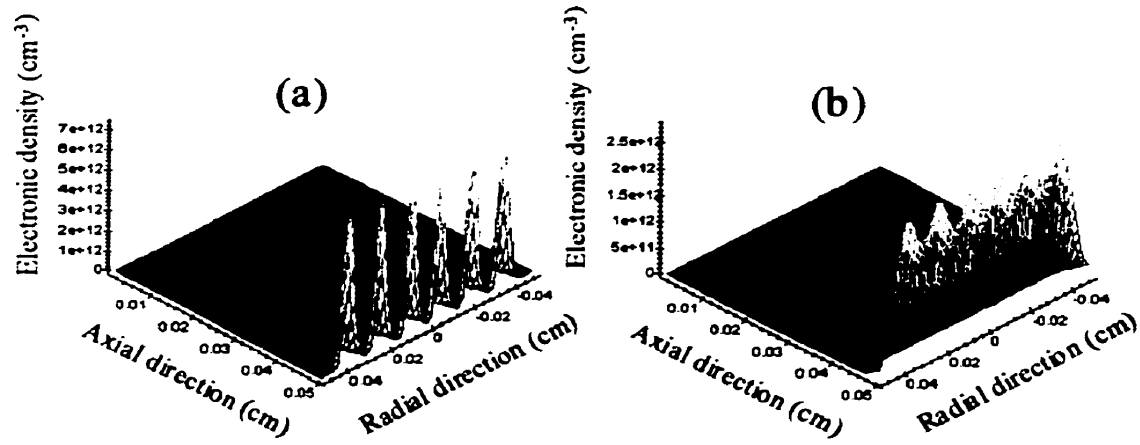

Figure 5.5 Electronic charge density distribution on the anode: before the occurrence of surface charge spreading (a) and after charge spreading (b).

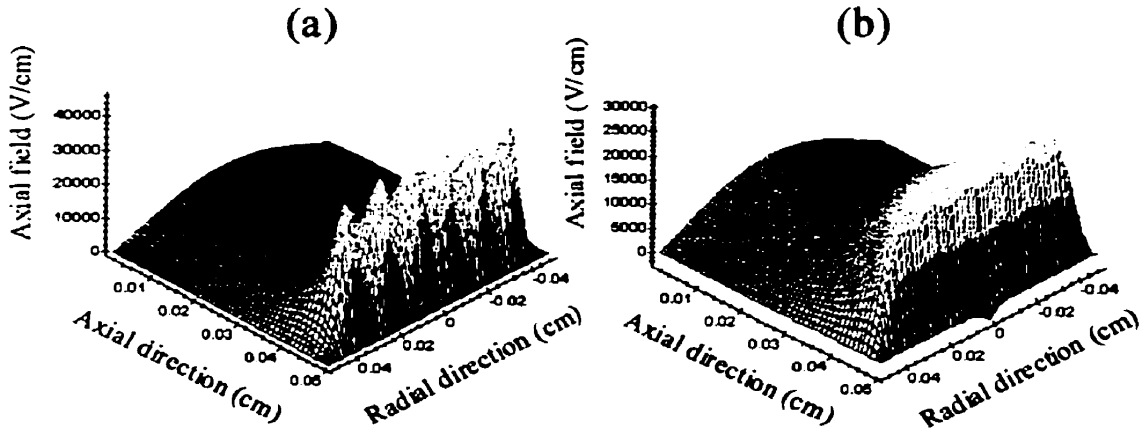

Figure 5.6 Axial field distribution in the gap for the two cases of anode charge: before the occurrence of surface charge spreading (a) and after charge spreading (b).

The new field distribution close to the dielectric surface due to the charge spreading on it's surface influences the deposited charge density as shown in Fig. 5.7: before the occurrence of surface charge decay (a), where there are non-uniform distributions of charge density on the surface, and after it (b), when one smooth spatial distribution of electronic surface charge occurs.

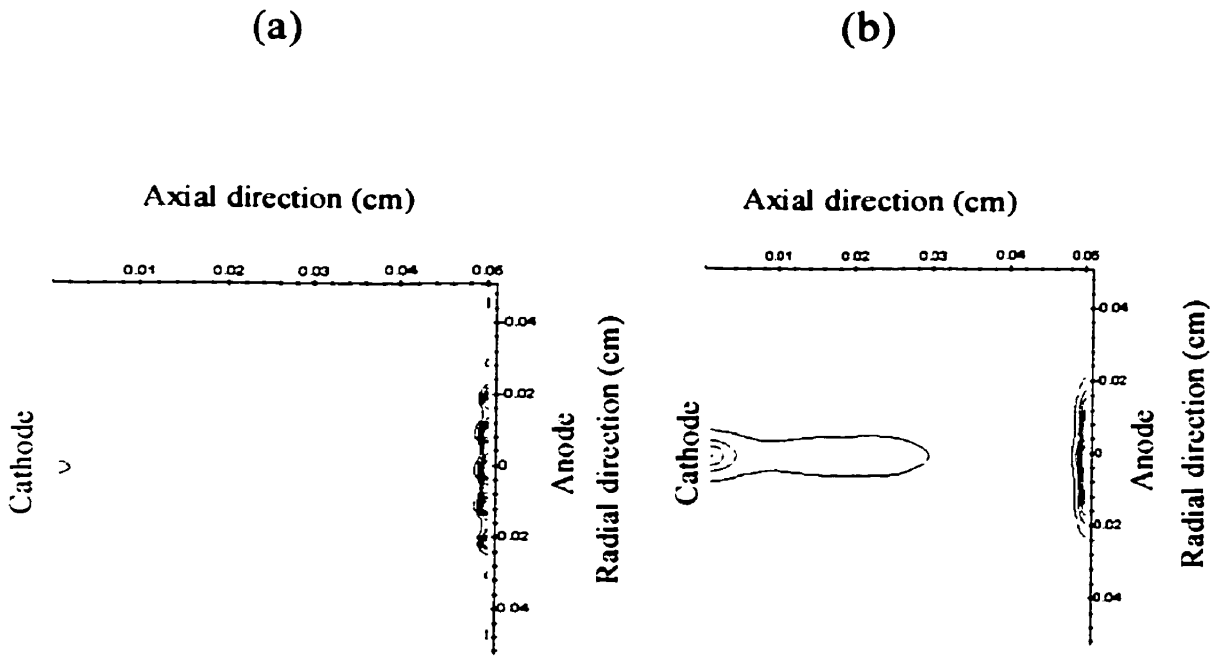

Figure 5.7 Electronic deposited charge density for the two cases of anode charge: before the occurrence of surface charge spreading (a) and after charge spreading (b).

CONCLUSION

We have developed an improved program to analyse the breakdown characteristics of a short gap having a dielectric-covered anode and metallic cathode. The calculations were carried out further to demonstrate the influence of surface charges and their distribution on the dielectric surfaces upon the breakdown process. Distribution of the surface charge strongly influences the radial distribution of charge density in the volume of the gap, time of discharge traversing the distance between the electrodes, charge remaining in the gap, etc.

In the case of a filamentary discharge, which was described in Sections 3.2.2 and 4.3 (uncharged anode case), an avalanche grows rapidly forming a narrow discharge channel during a short time of the discharge traversing the gap: t=0.7 ns in overvoltage case (Fig. 3.6), and t=1.5 ns in breakdown one (Fig. 4.5). The streamer breakdown condition described here is in a local avalanche of space charge. As a result of the discharge, the field due to electron space charge reaches a very high value (Fig. 3.2), which, in turn, leads to the generation of "hot" electrons in the dielectric, and to associated degradation of the dielectric material by impact of these electrons with the constituent molecules [2,3]. Some chemical products and defects formed at the dielectric surface have potential wells (charge traps), which are deeper than the surrounding medium [57]. As a result of charge carrier pile-up or trapping at interfaces within the inhomogeneous dielectric, distortions of the macroscopic field in the volume of the gap occur ([58], Section 5.2), leading to new filamentary discharges.

The charge accumulated at the dielectric surface drops the electric field value close to the anode, leading to channel expansion ([1], Section 4.3), and increasing of the time of discharge traversing the gap to t=2 ns (Section 4.3), as well as the remaining charge density in the gap (Section 4.3). The latter effect increases the value of radial field in the gap (Section 4.3, Figs. 4.8-4.9), leading to a broader radial distribution of space charge in the case of the charged anode (Fig. 4.3). The effect of a charged surface consists mostly in the formation of shallow traps of electrons in the dielectric [46], from where the trapped electrons can be released easily due to recombination with incident ions. The latter effect increases the photon emission from the cathode [58]. So, there is an increase in the probability of obtaining a glow discharge under the conditions of a charged surface, when the density of electrons, remaining in the gas before the occurrence of a new discharge, becomes higher.

When the decay process of surface charge occurs as shown in Section 5.2 (Fig. 5.1), the total electron charge (Fig. 5.3), remaining in the gap, and gap field (Fig. 5.2) are increased. The process of the surface charge spreading due to surface conductivity smoothes the peaks of field distribution close to the dielectric surface, remaining after the previous discharges (see Section 5.2, Figs. 5.5 and 5.6), leading to uniform distribution of electron density along the dielectric surface as shown in Fig. 5.7.

The long term process of charge accumulation and spreading on the dielectric surface leads to discharge modification from spark to glow form, leading to the new distributions of chemical products in the volume of the gap (see Appendix II), and

photoelectron emission at the cathode (see Appendix III); this latter aspect is the object of ongoing modeling studies.

REFERENCES

[1] BARTNIKAS, R. and NOVAK, J.P. (to be published). Effect of Dielectric Surfaces on the Nature of Partial Discharges.

[2] HUDON, C., BARTNIKAS, R. and WERTHEIMER, M.R. (1993). Spark-to-glow Discharge Transition due to Increased Surface conductivity on Epoxy Resin Specimens. IEEE Trans. Electr. Insul., 28, 1-8.

[3] HUDON, C., BARTNIKAS, R. and WERTHEIMER, M.R. (1995). Effect of Physico-chemical Degradation of Epoxy Resin on Partial Discharge Behavior. IEEE Trans. Electr. Insul., 2, 1083-1094.

[4] ELIASSON, B. and KOGELSCHATZ, U. (1991). Nonequilibrium Volume Plasma Chemical Processing. IEEE Trans. Plasma Sci., 19, 1063-1077.

[5] ELIASSON, B., HIRTH, M. and KOGELSCHATZ, U. (1987). Ozone synthesis from oxygen in dielectric barrier discharges. J. Phys. D, 20, 1421-1437.

[6] DHALI, S.K. and SARDJA, I. (1991). Dielectric-barrier discharge for processing of SO_2/NO_x. J. Appl. Phys., 69, 6319-6324.

[7] STORCH, D.G. and KUSHNER, M.J. (1993). Destruction mechanisms for formaldehyde in atmospheric pressure low temperature plasmas. J. Appl. Phys., 73, 51-55.

[8] VAN BRUNT, R.J. (1994). Physics and Chemistry of Partial Discharge and Corona. Recent Advances and Future Challenges. IEEE Trans. Electr. Insul., 1, 761-784.

[9] EVANS, D., ROSOCHA, L.A., ANDERSON, G.K. , COOGAN, J.J. and KUSHNER, M.J. (1993). Plasma remediation of trichloroethylene in silent discharge plasmas. J. Appl. Phys., 74, 5378-5386.

[10] CHANG, B., BALBACH, J.H., ROOD, M. J. and KUSHNER, M.J. (1991). Removal of SO_2 from gas streams using a dielectric barrier discharge and combined plasma photolysis. J. Appl. Phys., 69, 4409-4417.

[11] JING, LI, SUN, W., PASHAIE, B. and DHALI, S.K. (1995). Streamer Discharge Simulation in Flue Gas. IEEE Trans. Plasma Sci., 23, 672-678.

[12] ROSOCHA, L.A., ANDERSON, G.K. , COOGAN, J.J., HECK, H.G., KANG M., MCCULLA, W.H., BECHTOLD, L.A., TENNANTAND, R.A., and WANTUCK,

P.J. (1993). Treatment of hazardous organic wastes using silent discharge plasmas. NATO ASI Series, G34, Part B, 282-308.

[13] YAMAMOTO, T., LAWLESS, P.A., OWEN, M.K. and ENSOR, D.S. (1993). Decomposition of volatile organic compounds by a packed-bed reactor and a pulsed-corona plasma reactor. NATO ASI Series, G34, Part B, 224-237.

[14] BARTNIKAS, R. (1971). Some Observations on the Character of Corona Discharges in Short Gap Spaces. IEEE Trans. Electr. Insul., 6, 63-75.

[15] BARTNIKAS, R. and NOVAK, J.P. (1987). Breakdown model of a short plane-parallel gap. J. Appl. Phys., 62, 3605-3615.

[16] BARTNIKAS, R. and NOVAK, J.P. (1988). Early stages of channel formation in a short-gap breakdown. J. Appl. Phys., 64, 1767-1774.

[17] NOVAK, J.P. and BARTNIKAS, R. (1988). Density profiles, electric field and energy dissipation in a short gap breakdown: a two dimensional model. J. Phys. D: Appl. Phys., 21, 896-903.

[18] BARTNIKAS, R. and NOVAK, J.P. (1990). Collisional Phenomena and Current Buildup in the Electrical Breakdown of Hydrogen. IEEE Trans. on Plasma Science, 18, 775-783.

[19] BARTNIKAS, R. and NOVAK, J.P. (1991). Theoretical and Experimental Investigations on the Process of High-Pressure Discharge Development. IEEE Trans. Electr. Insul., 19, 95-101.

[20] BARTNIKAS, R. and NOVAK, J.P. (1992). On the Spark to Pseudoglow and Glow Transition Mechanism and Discharge Detectability. IEEE Trans. Electr. Insul., 27, 3-14.

[21] BARTNIKAS, R. and NOVAK, J.P. (1992). Effect of Air Admixture in Helium on the Rate of the Breakdown Current Rise. IEEE Trans. on Plasma Science, 20, 487-492.

[22] BARTNIKAS, R. and NOVAK, J.P. (1993). On the Character of Different Forms of Partial Discharge and their Related Terminologies. IEEE Trans. Electr. Insul., 28, 956-968.

[23] BARTNIKAS, R. and NOVAK, J.P. (1995). Effect of Overvoltage on the Risetime and Amplitude of PD Pulses. IEEE Trans. Electr. Insul., 2, 557-565.

[24] NOVAK, J.P. and BARTNIKAS, R. (1996). Quantative Model of a Short-Gap Breakdown in Air. IEEE XVIIth International Symposium on Discharges and Electrical Insulation in Vacuum, Berkeley, 60-64.

[25] NIEMEYER, L., ULLRICH, L. and WIEGART, N. (1989). The Mechanism of Leader Breakdown in Electronegative Gases. IEEE Trans. Electr. Insul., 24, 309-324.

[26] WU, C. and KUNHARDT, E.E. (1988). Formation and propagation of streamers in N_2 and N_2-SF_6 mixtures. Physical Review A, 37, 4396-4406.

[27] ELIASSON, B. and KOGELSCHATZ, U. (1991). Modeling and Applications of Silent Discharge Plasmas. IEEE Trans. Plasma Sci., 19, 309-323.

[28] WANG, M.C. and KUNHARDT, E.E. (1990). Streamer dynamics. Physical Review A, 42, 2366-2373.

[29] YOSHIDA, K. and TAGASHIRA, H. (1976). Computer simulation of a nitrogen discharge considering the radial electron drift. J. Phys. D: Appl. Phys., 9, 485-490.

[30] CRICHTON, G.C., KARLSSON, P.W. and PEDERSEN, A. (1989). Partial Diascharges in Ellipsoidal and Spheroidal Voids. IEEE Trans. Electr. Insul., 24, 335-342.

[31] MORROW, R. (1987). Properties of streamers and streamer channels in SF_6. Physical Review A, 35, 1778-1785.

[32] DHALI, S.K. (1989). Electrical Characteristics of Pulsed Glow Discharges. IEEE Trans. Plasma Sci., 17, 603-611.

[33] MECHTLY, E.A. (1964). The International System of Units, Physical Constants and Conversion Factors. George C. Marshall Space Flight Center, NASA, Washington, D. C.

[34] MORROW, R. (1985). Theory of negative corona in oxygen. Physical Review A, 32, 1799-1809.

[35] DHALI, S.K. and WILLIAMS, P.F. (1987). Two dimensional studies of streamers in gases. J. Appl. Phys., 62, 4696-4707.

[36] DHALI, S.K. and LI, J. (1997). Simulation of microdischarges in a dielectric-barrier discharge. J. Appl. Phys., 82, 4205-4210.

[37] VITELLO, P.A., PENETRANTE, B.M. and BARDSLEY, J.N. (1994). Simulation of negative-streamer dynamics in nitrogen. Physical Review E, 49, 5574-5598.

[38] DAVIES, A.J., DAVIES, C.S. and EVANS, C.J. (1971). Computer simulation of rapidly developing gaseous discharges. Proc. IEE, 118, 816-823.

[39] SATO, N. (1980). Discharge current induced by the motion of charged particles. J. Phys. D, 13, L 3-6.

[40] BORIS, J.P. and BOOK, D.L. (1973). Flux-Corrected Transport.1. SHASTA, A Fluid Transport Algorithm That Works. J. Comput. Phys., 11, 38-69.

[41] ZALESAK, S.T. (1979). Fully Multidimensional Flux-Corrected Transport Algorithms for Fluids. J. Comput. Phys., 31, 335-362.

[42] KUNHARDT, E.E. and WILLIAMS, P.F. (1985). Direct Solution of Poisson's Equation in Cylindrically Symmetric Geometry: A Fast Algorithm. J. Comput Phys., 57, 403-414.

[43] WU, C. and KUNHARDT, E.E. (1989). Numerical Solution of Poisson's Equation for Rapidly Varying Driving Functions. J. Comput Phys., 84, 247-254.

[44] NIEMEYER, L. (1995). A Generalized Approach to Partial Discharge Modeling. IEEE Trans. Electr. Insul., 2, 510-528.

[45] GUTFLEISCH, F. and NIEMEYER, L. (1995). Measurement and Simulation of PD in Epoxy Voids. IEEE Trans. Electr. Insul., 2, 729-743.

[46] MASSINES, F., RABEHI, A., DECOMPS, P. and MAYOUX, C. (1998). Experimental and theoretical study of a glow discharge at atmospheric pressure controlled by dielectric barrier. J. Appl. Phys., 83, 2950-2957.

[47] MEEK, J.M. and GRAGGS, J.D. (1978). Electrical Breakdown of gases. John Wiley & Sons, Ltd., New York, 535-567.

[48] JING, T. (1995). Surface Charge Accumulation. IEEE Trans. Electr. Insul., 2, 771-778.

[49] BARTNIKAS, R. (1968). Note on Discharges in Helium Under AC Conditions. British J. Appl. Phys., (J. Phys. D.), 1, 659-661.

[50] MCALLISTER, I.W. (1991). Surface Current Density $\bar{K}$. IEEE Trans. Electr. Insul., 28, 416-417.

[51] GAMEZ-GARCIA, M., BARTNIKAS, R. and WERTHEIMER, M.R. (1987). Synthesis Reactions Involving XLPE Subjected To Partial Discharges. IEEE Trans. Electr. Insul., 22, 199-205.

[52] GAMEZ-GARCIA, M., BARTNIKAS, R. and WERTHEIMER, M.R. (1990). Modification of XLPE Exposed to Partial Discharges at Elevated Température. IEEE Trans. Electr. Insul., 25, 688-692.

[53] SOMERVILLE, I. and VIDAUD, P. (1985). Surface spreading of charge due to ohmic conduction. Proc. Royal Soc. Lond. A, 399, 277-293.

[54] ZHELEZNYAK, M.B., MNATSAKANIAN, A.K. and SIZYKH, S.V. (1982). Photoionization of mixtures of nitrogen and oxygen by gas discharge radiation (in Russian). Teplofizika Vysokih Temperatur, 20, 423-428.

[55] KOSSYI, I.A., KOSTINSKI, A.Y., MATVEEV, A.A. and SILAKOV, V.P. (1994). Plasma-chemical processes in non-equilibrium mixture of nitrogen and oxygen (in Russian). Proc. Inst. Gen. Phys., 47, 37-57.

[56] DAVIES, A.J., EVANS, C.J. , TOWNSEND, P. and WOODISON, P.M. (1977). Computation of axial and radial development of discharges between plane parallel electrodes. Proc. IEE, 124, 179-182.

[57] GONG, H., CHOOI, K.M. and ONG, C.K. (1995). Charging of Deformed Semicrystalline Polymers Observed with a Scanning Electron Microscope. IEEE Trans. Electr. Insul., 2, 1123-1131.

[58] BARTNIKAS, R. (1997). Performance Characteristics of Dielectrics in the Presence of Space Charge. IEEE Trans. Electr. Insul., 4, 544-557.

[59] WEAST, R. C. (1985). Handbook of Chemistry and Physics. CRC Press Inc., 66th edition, E-254.

[60] ROBINSON, J. W. (1974). Handbook of Spectroscopy. CRC Press Inc., Cleveland, 1.

APPENDIX I: CALCULATION OF THE RATE OF PHOTOIONIZATION

The aim of present calculations is to determine the rate of photoionization and production of photoelectrons in the volume of the gap as a result of the discharge. The conditions in the air gap at atmospheric pressure were similar to those given in Section 3.1; the calculated densities of photoelectrons are compared to the neutral pre-ionisation background of 10^7 cm^{-3} electrons and ions, as well as with the total net electron density in the gap. It is known [54] that the molecular bands of excited N_2 emit UV photons, which cause the direct ionisation of molecular oxygen O_2. The rate of photoionization from the small volume $dV_1=r_1 \cdot dr_1 \cdot dz_1 \cdot d\phi_1$ of a cylindrical ring at element (r_2, z_2) shown in Fig. 1 is calculated.

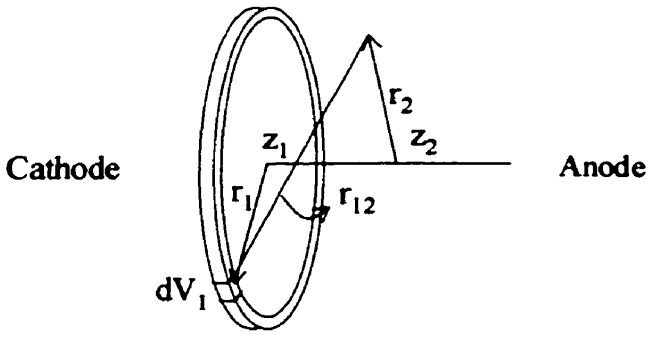

Figure 1 Geometry for calculation of photoionization rate.

The rate of photoionization within the ring (r_2, z_2) is given by [54]:

$$d\Psi_{ph2} = \frac{q(r_1, z_1) \cdot f(r_{12}) \cdot dV_1}{4\pi \cdot r_{12}^2} \tag{1}$$

where r_{12} is the distance between the volume dV_1 and target point (r_2, z_2):

$$r_{12} = [r_1^2 + r_2^2 + (z_2 - z_1)^2 - 2 \cdot r_1 \cdot r_2 \cdot \cos\phi]^{\frac{1}{2}} \tag{2}$$

where $\phi=\phi_2-\phi_1$.

The factor $f(r_{12})$ in Eq. 1 expresses the absorption of radiation by the O_2 molecules [54]:

$$f(r_{12}) = \frac{\exp(-\chi_{min} \cdot P_{o_2} \cdot r_{12}) - \exp(-\chi_{max} \cdot P_{o_2} \cdot r_{12})}{r_{12} \cdot \log(\chi_{max} / \chi_{min})} \tag{3}$$

where χ_{min}=2 $cm^{-1} \cdot Torr^{-1}$ and $\chi_{max}=3.5 \cdot 10^{-2}$ $cm^{-1} \cdot Torr^{-1}$ are the absorption coefficients for O_2, and P_{o2} is the partial pressure of oxygen. The emission intensity $q(r_1, z_1)$ of the source ring is given by:

$$q(r_1, z_1) = A \cdot \alpha_1 \cdot |\upsilon_{el}| \cdot n_{e1} \tag{4}$$

where $\upsilon_{el}=\mu_e \cdot E$ is the electron drift velocity, n_e is the electron density in source ring, α_1 is the Townsend ionization coefficient, and the term A is equal to:

$$A \approx 0.1 \cdot \frac{P_q}{P + P_q} \tag{5}$$

where P is the gas pressure and P_q=30 Torr is the quenching pressure of the radiating state $C^3\Pi_u$ of N_2.

The rate of photoionization is obtained by integrating Eq. 1 with respect to r_1 ($0 \le r_1 \le R$) and ϕ(($0 \le \phi \le \pi$), that is:

$$\Psi_{ph2}(r_1, z_1) = \frac{1}{2\pi} \int_0^R q(r_1, z_1) \cdot r_1 \cdot dr_1 \cdot dz_1 \int_0^{\pi} d\phi \cdot \frac{f(r_{12})}{r_{12}^2} \qquad (6)$$

Eq. 6 may be evaluated numerically to determine the different times of discharge propagation within the gap. Figure 2 shows the calculated rate of photoionization profile with discharge propagation time as a parameter.

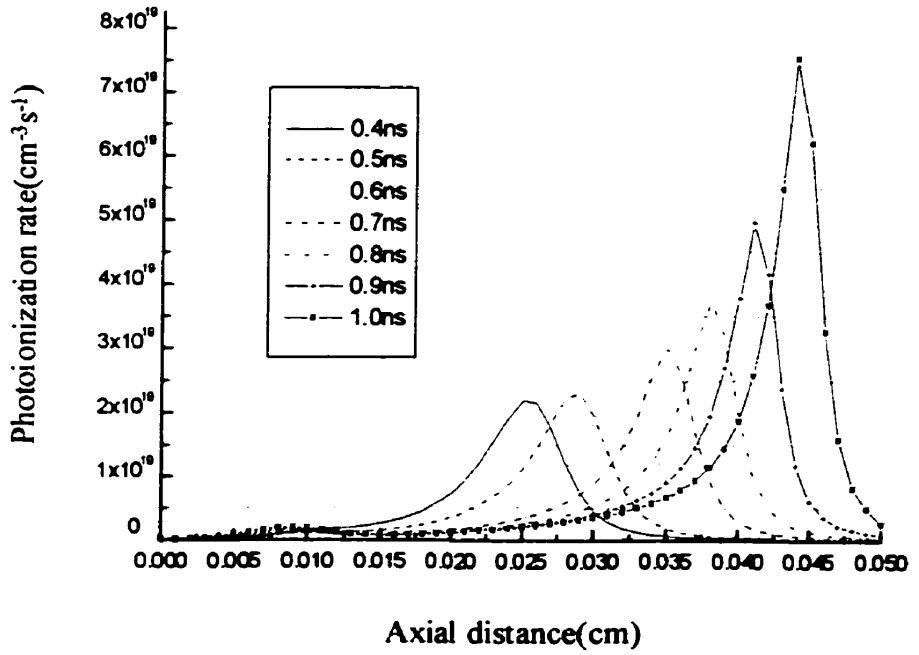

Figure 2 Profile of the rate of photoionization.

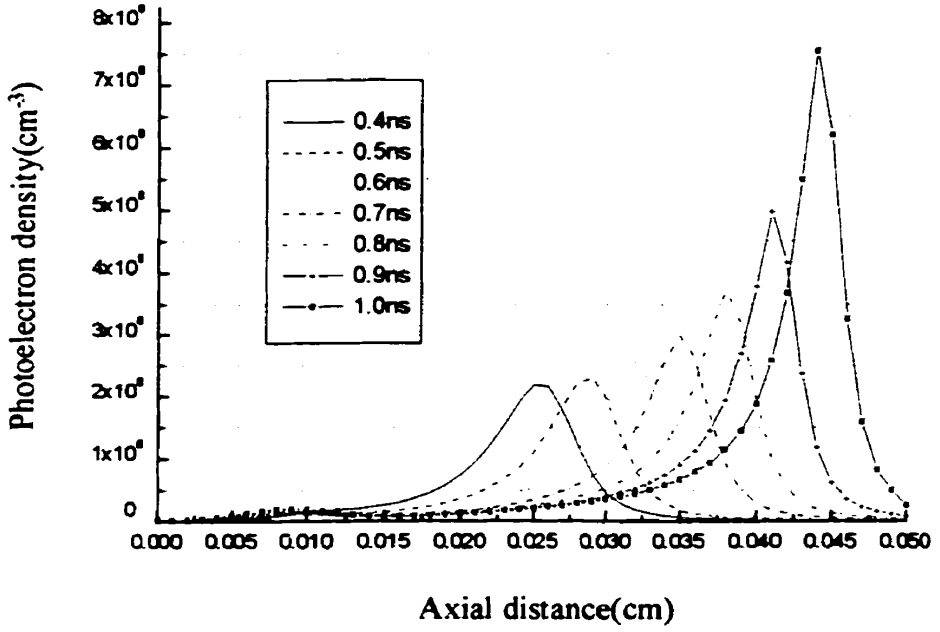

Figure 3 Electronic density profile due to photoionization as a result of the discharge in the gap.

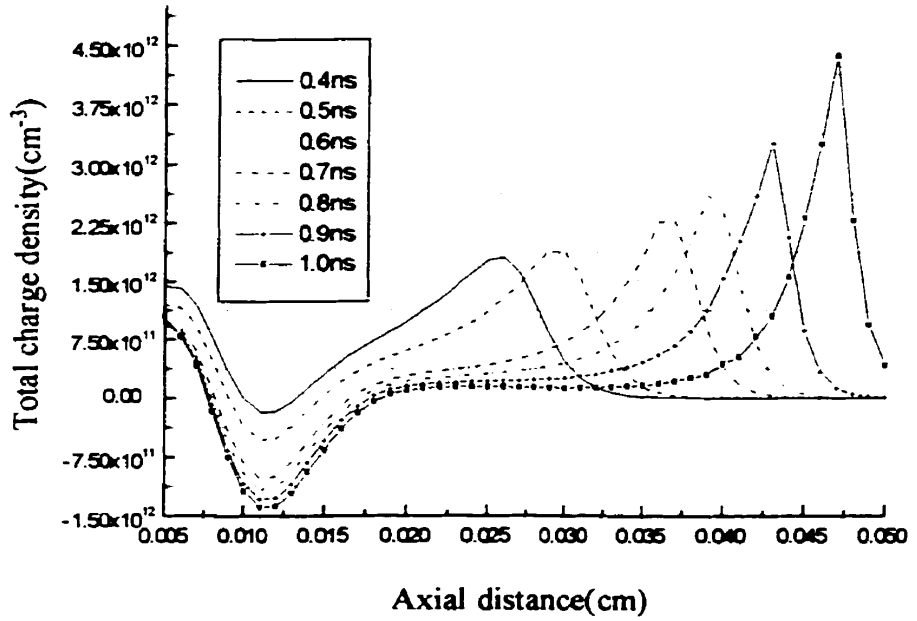

Figure 4 Total charge density profile.

Fig. 3 shows that excessive photoelectron densities are formed around the streamer head. The photoelectron density close to the anode reaches the value $7.5 \cdot 10^8$ cm^{-3} that is higher than background pre-ionisation density 10^7 cm^{-3}, used in Section 3.1. The total electron density in the gap reaches a value of $4.5 \cdot 10^{12}$ cm^{-3} (Fig. 4), which is higher than the density of photoelectrons (Fig. 3) by four orders of magnitude. Applying the two different cases mentioned above, shows that the calculated photoelectron density and background pre-ionisation in the model gave us very similar results in field distribution and charge densities, when discharge propagation occurs. Consequently, these calculations show that it is possible to apply the background pre-ionisation of 10^7-10^8 cm^{-3} for the short air gap discharge at atmospheric pressure, instead of calculating the photoelectron density that involves a more time-consuming procedure.

APPENDIX II: FORMATION OF CHEMICAL PRODUCTS IN ATMOSPHERIC PRESSURE AIR DISCHARGE

As a result of the discharge in gap, the electrons gain energy in high electric field and lose it by inelastic collisions with molecules to produce new chemical species in the gas. The rate of formation of chemical products of each inelastic process is defined by electron energy distribution function, which depends only on the local value of field E and number density of molecules N under atmospheric pressure conditions [55]. In present calculations we suppose that air consists of N_2(79%), O_2(20%), and H_2O(1%). The concentrations of chemical products M_F were calculated from:

$$\frac{dM_F}{dt} = k \cdot s \cdot n_e \cdot M_P \qquad (7)$$

where s is the stoichiometric coefficient, which is equal to the number of reaction products, k is the reaction rate constant:

$$k = \alpha \cdot \exp[-\frac{\beta}{\xi}], \qquad (8)$$

M_P is the density of parent molecules, and $\xi=10^{17}\cdot E/N$. The coefficients α, β, and the stoichiometric coefficients for a chosen number of reactions, which have higher reaction rate coefficients taken from [55], are given below in Table 1. The rating in the number of species produced in the formation of chemical products was found by using Fig. 5, where the results of the simulation are presented.

Table 1 Types of chemical reactions, coefficients α and β, the stoichiometric coefficients *s*, and the rating in the number of species produced (see Fig. 5).

Type of reaction	α, cm^3/s	β, $(\cdot 10^{-17})$ $V \cdot cm^2$	*s*	rating
$N_2+e=>N_2(B)+e$	$6.31 \cdot 10^{-9}$	340.8	1	1
$N_2+e=>N_2(C)+e$	$6.31 \cdot 10^{-9}$	485.9	1	2
$N_2+e=>N_2(W^3, B')+e$	$5.01 \cdot 10^{-9}$	354.6	1	3
$N_2+e=>N_2(A)+e$	$3.98 \cdot 10^{-9}$	322	1	4
$N_2+e=>N_2(a, w^1)+e$	$3.16 \cdot 10^{-9}$	400.7	1	5
$O_2+e=>O(^3P)+O(^3P)+e$	$1.26 \cdot 10^{-8}$	308.5	2	6
$N_2+e=>N_2^+ +e+e$	$5 \cdot 10^{-9}$	840.4	1	7
$N_2+e=>N_2(a')+e$	$1.59 \cdot 10^{-9}$	384.5	1	8
$O_2+e=>O(^3P)+O(^1D)+e$	10^{-8}	389.1	1	9
$O_2+e=>O(^3P)+O(^1S)+e$	$1.59 \cdot 10^{-9}$	274	1	10
$O_2+e=>O_2^+ +e+e$	$1.59 \cdot 10^{-9}$	647	1	11
$N_2+e=>N_2(E, a'')+e$	$7.94 \cdot 10^{-11}$	585	1	12
$O_2+e=>O^- +O$	$5 \cdot 10^{-10}$, $\xi \le 80$ $6.31 \cdot 10^{-11}$, $\xi > 80$	283, $\xi \le 80$ 131.2, $\xi > 80$	1	13
$O_2+e=>O_2(a)+e$	10^{-9}, $\xi \le 40$ $6.31 \cdot 10^{-11}$, $\xi > 40$	119.7, $\xi \le 40$ 8.1, $\xi > 40$	1	14
$O_2+e=>O_2(b)+e$	$3.16 \cdot 10^{-10}$, $\xi \le 30$ $6.31 \cdot 10^{-12}$, $\xi > 30$	138.2, $\xi \le 30$ 16.6, $\xi > 30$	1	15
$H_2O+e=>OH+H+e$	$2 \cdot 10^{-11}$	322	1	16

Fig. 5 shows that the most abundant species generated by discharge are excited nitrogen molecules and short-lived oxygen atoms, which under atmospheric pressure conditions tend to formation of ozone molecules O_3.

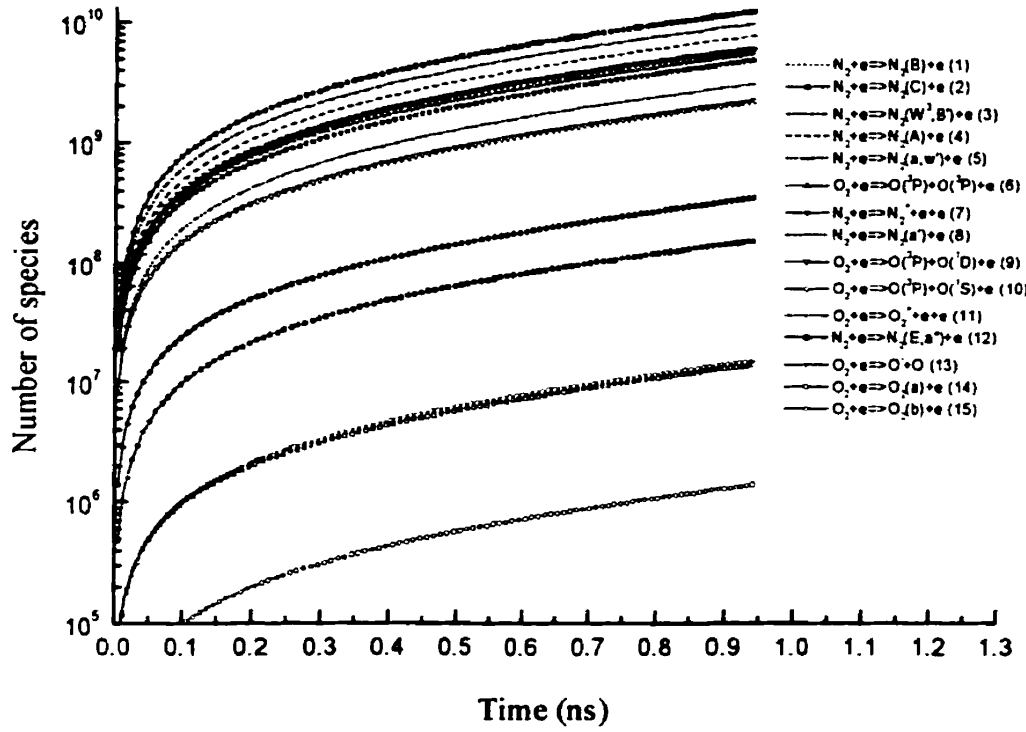

Figure 5 Chemical products in air.

The concentration of generated products occurs where E/N reaches its maximum values, i.e. close to the anode as shown as an example for the excited states of oxygen molecules $O_2(a)$ in Fig. 6.

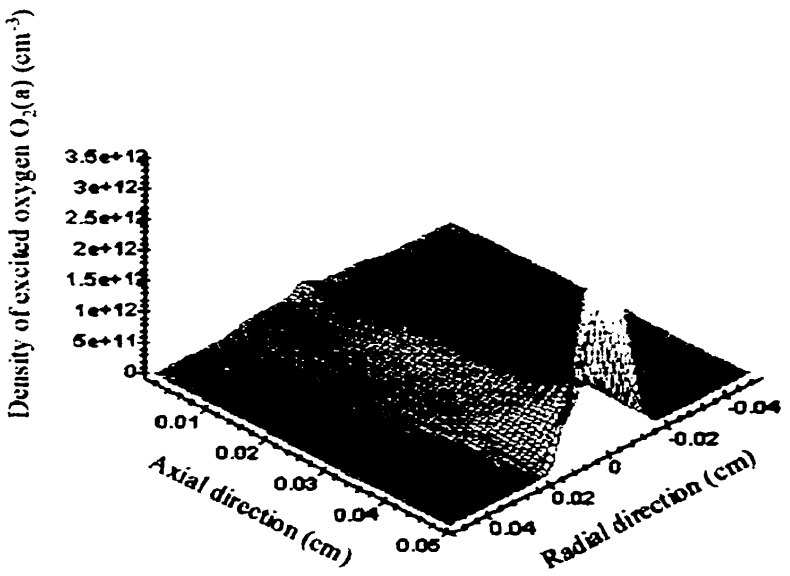

Figure 6 Density of excited states of oxygen $O_2(a)$ at time of discharge propagation, t=1.5 ns.

APPENDIX III: PHOTON FLUX AT THE CATHODE

To compute the photon flux Ψ at the cathode, we use, as was already done in [56], the form of Poisson's Equation 1.2 (Section 1.2), where we replace the charge density $\rho(r, z)$ by the density of excited species $n_{ex}(r, z)$, and the electric field by the photon flux Ψ. The photon flux through a unit area at point Q_1 on the cathode surface due to a point source, volume $dV=r'dr'dz'd\phi'$, of excited atoms at $Q_2(r', z', \phi')$ shown in Fig. 7, is given by:

$$d\Psi_{cathode}(r,z') = \frac{1}{4\pi} \frac{n_{ex} \cdot r' dr' \cdot z' dz' d\phi'}{(z'^2 + r^2 + r'^2 - 2rr'\cos\phi')^{\frac{3}{2}}} \tag{9}$$

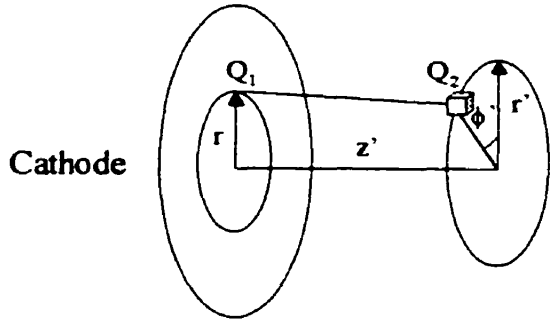

Figure 7 Geometry for calculation of the photon flux at the cathode.

The total photon flux through unit area at the cathode is obtained by integrating the Eq. 9 over all points (r', z', ϕ'):

$$\Psi_{cathode}(r) = \frac{1}{4\pi} \int_0^{d_g} \int_0^R n_{ex}(z', r') r' dr' dz' \int_0^{2\pi} \frac{z' \cdot d\phi'}{(z'^2 + r^2 + r'^2 - 2rr'\cos\phi')^{\frac{3}{2}}}, \tag{10}$$

where d_g is the gap distance.

Evaluation of only the angle related integral in Eq. 10 yields:

$$\Psi_{cathode}(r) = \frac{1}{\pi}\int_0^{d_g}\int_0^{R} n_{ex}(z',r')\{K(y) + y\frac{dK(y)}{dy}\}\frac{r'z'dr'dz'}{[z'^2+(r+r')^2]^{\frac{3}{2}}} \tag{11}$$

where K(y) is the elliptic integral; its value is given by:

$$K(y) = \int_0^{\frac{\pi}{2}} \frac{d\theta}{\sqrt{1-y^2\sin^2\theta}} \tag{12}$$

$$\text{where } y = \frac{2\sqrt{r'r}}{[(r+r')^2+z'^2]^{\frac{1}{2}}} \tag{13}$$

The photon flux is determined in terms of Eq. 11, by noting that:

$$\{K(y) + y\frac{dK(y)}{dy}\} = \frac{\pi}{2}\cdot\frac{1}{1-y^2}[1-\frac{1}{4}y^2-\frac{3}{64}y^4-\frac{5}{256}y^6\ldots] \tag{14}$$

As an example, we make use of the excited oxygen species, $O_2(a)$, to illustrate the calculation procedure for estimating the photon flux at the cathode. For this reason, we employ the distribution of the density of the excited state of $O_2(a)$, which is shown in Fig. 8. Figure 9 depicts the calculated photon flux at the cathode surface. Now the photon flux calculated from the distribution of chemical products, n_{ex}, can be in turn used in further calculations to determine the production of photoelectrons at the cathode.

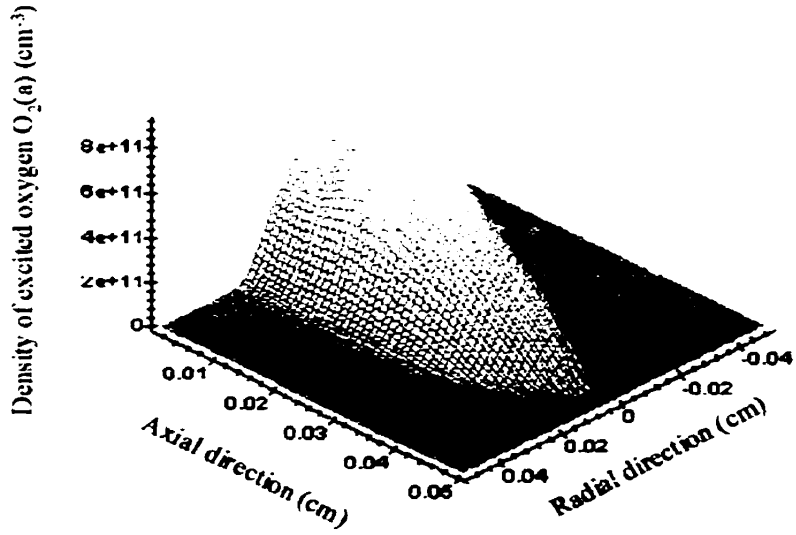

Figure 8 Density of excited states of oxygen $O_2(a)$ at time of discharge propagation t=1 ns.

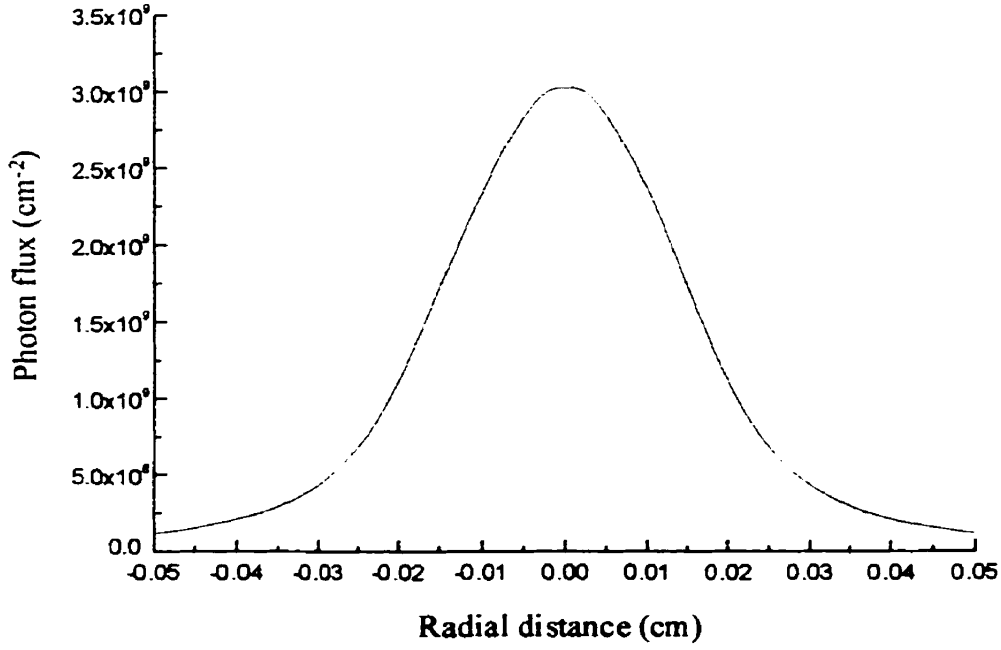

Figure 9 Photon flux at cathode surface due to excited species of oxygen $O_2(a)$.

APPENDIX IV: IMPROVEMENTS TO EXPERIMENTAL SETUP AT IREQ AND PREPARATIONS TO AN EXPERIMENT

1 Description of the experimental electric circuit

We have studied an experimental setup to accomplish electrical and optical measurements of PD in the future. The electrical circuit used for preliminary tests, before the experimental work will be started, is shown in Figure 10.

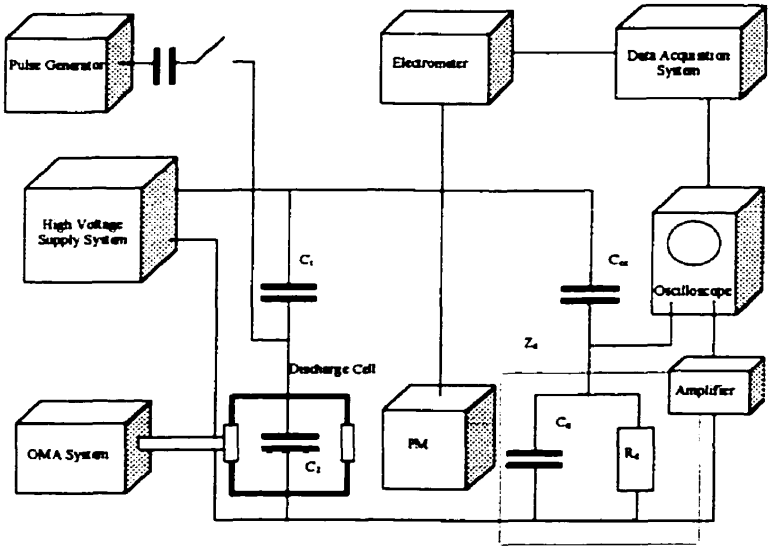

Figure 10 Electric configuration of detection system, where: C_1 is a 40 pF discharge free vacuum capacitor, used as a voltage divider, C_3 is a 50 pF test capacitor, Z_d is a 50 Ω detection impedance, and C_{cc} is a 1000 pF charge capacitor.

2 Data acquisition programs and calibration of optical system

We have started preparations for the experiment by writing (in Borland C^{++}) the data acquisition and treatment programs for the programmable electrometer (Keithley, Model 617) and digitizing oscilloscope (Hewlett-Packard, model 54200A). The next step of the experimental setup was calibration of the Multichannel Optical Analyzer ("OMA", Princeton Instruments, Model ST-120), which was performed for two gratings (Groove densities of 600 g/mm and 1200 g/mm) by using a mercury-argon lamp (6035 Hg(Ar) Lamp, 6047 Power Supply, Oriel Corporation). The standard values for the mercury lines were taken from the Handbook of Chemistry and Physics [59] and from the Handbook of Spectroscopy [60].

3 Modification of the PD cell

We added three windows to the glass cell to make the optical measurements, two of them were connected with multichannel analyzer (OMA) and photomultiplier. By using a micrometer screw, we established the distance between the two electrodes (one is of metal, with diameter 2.5 cm, and another electrode was covered with epoxy, 5 cm in diameter) in the cell at 0.5 mm. We verified the vacuum pumping system and performed the vacuum test of the cell.

4 Epoxy coating procedure

To perform an epoxy coating procedure we used epoxy resin Araldite CW 229 and hardener HW 229-1 (bought from Ciba Polymers Electrical & Structural Casting Systems Company). Since special care must be taken to avoid the presence of bubbles or the appearance of unwanted stresses inside the epoxy, we used the specific equipment at CITEX to make the coating of electrodes properly. A preparation step involves a cleaning procedure for electrodes and matrices. The stainless steel electrodes and brass matrices were prepared at École Polytechnique. Preparations of epoxy and hardener were made in special containers at a temperature of 65 ^{0}C and pressure 5 mbar during 24 hours to obtain the necessary consistence. Epoxy and hardener had to have a mass of 140-145 gr, and the total mass of epoxy and hardener mixture was 280 gr. We dried the molding system with electrodes for 2-3 hours at 140 ^{0}C inside an oven. After all preparations, we placed the molding system inside the metallic cell to start coating. The pressure in the cell was fixed at 15 mbar, to evacuate air bubbles from the epoxy-hardener mixture. We then gradually increased the pressure in the cell up to atmosphere, after which the molding system was placed inside of the programmed oven, where the temperature was changed gradually from 80 ^{0}C to 140 ^{0}C during 4 hours. The temperature was maintained at 140 ^{0}C for the next 20 hours. Finally, the specimens were removed from the molding system.

5 Experimental tests

After the experimental setup was completed, we made the detection tests of small signals (0.3-0.5 pC), simulating discharges of different amplitude, which were generated by a pulse generator. To amplify the signal, we use the 100 MHz Current Feedback Amplifier HA-5004, and two Medium Power Amplifiers (Model ZHL-A, Mini-Circuits, Brooklyn, NY, +21 dBm, range from 7 kHz to 4.2 GHz). The characteristics of the experimental apparatus are given below.

6 Principal characteristics of the detection system

Here we present the principal characteristics of the detection system for the experiment.

Programmable Electrometer (Model 617, Keithley Instruments, Inc. Cleveland, Ohio, USA):

Volts: range from 200 mV to 200 V, resolution from 10 μV to 10 mV,

Amps: range from 2 pA to 20 mA, resolution from 100 aA to 1 μA,

Coulombs: range from 200 pC to 20 nC, resolution from 10 fC to 1 pC,

Ohms: range from 2 kΩ to 200 GΩ, resolution from 100 mΩ to 10 MΩ.

Measurement range for digitizing Oscilloscope (Model 54200A, Hewlett-Packard, 200 MHz, Channel 1 and 2):

Voltage: from 40 mV to 40 V,

Time: from 50 ns to 10 s.

Photomultiplier (Model C31034A-02, Burle Industrie Inc.):

Spectral response: from 185 nm to 950 nm,

Amplification current: $0.6 * 10^6$,

Using temperature: from $-80^{o}C$ to $+30^{o}C$,

Voltage between anode and cathode: 2200 V (max),

Photocathode sensitivity: 720 A/lm,

Background noise: 12 pulses per second ($30^{o}C$).

Multichannel Optical Analyzer ("OMA", Princeton Instruments, Model ST-120) & Spectrometer (Model 1681C, SPEX Industries, Inc., Edison NJ):

ST-100 scan crystal: 8.064 MHz.

Diode array: 1024 elements,

Scan time (integration time) during normal operation: 16.3174 ms.

Holographic Gratings (Model 6006-300 and 12006-500):

Groove density for 6006-300 (12006-500): 600 (1200) gr/mm,

Blaze angle for 6006-300: 300 nm and for 12006-500: 500 nm,

Theoretical Resolving Power: $R_T = \frac{\lambda}{\Delta\lambda} = \frac{\nu}{\Delta\nu} = mN$, where m is order of diffraction (m=1), λ is wavelength, ν is wavenumber and N is a total number of grating ruling. We have for m=1: R_T =1200 $\frac{A^0}{mm}$ for 12006-500 Model, and R_T =600 $\frac{A^0}{mm}$ for 6006-300 Model

ruling. We have for m=1: R_T =1200 $\frac{A^0}{mm}$ for 12006-500 Model, and R_T =600 $\frac{A^0}{mm}$ for 6006-300 Model

Data Acquisition System (IBM PC 386)

High Voltage Supply System (Biddle Model 66JS90, transformer 60 Hz)

Pulse generator (Model 3310A, Hewlett Packard)